Direct to metal anti-corrosion coatings

Gwynfor Callaghan

Submitted to Swansea University In fulfilment of the requirements for the degree of Master of Science

2020

Supervisors: Dr Natalie Wint, and Professor Geraint Williams

Materials Research Centre

School of Engineering

Swansea University

Summary

The primary objective of this work was to evaluate the corrosion driven coating failure mechanisms affecting a commercial polyurethane coating (RAPTOR), traditionally applied as a topcoat, when instead directly applied to iron. This was done by evaluating its susceptibility to corrosion driven cathodic disbondment and Filiform corrosion.

The effect of cure time on the completion of the polymerization reaction was characterised using ATR-FTIR. It showed a direct correlation between cure time and resistance to cathodic disbondment.

The kinetics for cathodic disbondment was investigated using adapted Stratmann delamination cells as well as the scanning Kelvin probe. Free corrosion potential profiles were generated and allowed for the rate of delamination of RAPTOR from iron to be deduced. The rate limiting mechanism for the cathodic disbondment of RAPTOR was shown to be migrationof electroactive species under the coating .

Filiform corrosion was initiated via addition of an aqueous iron chloride solution to penetrativeRAPTOR coating scribes. Samples were maintained at a relative humidity of 94 % . Image analysis software was used to evaluate the geometry of filaments formed and the results were compared to those obtained in the case of polyvinyl butyral coatings (PVB)

Aluminium polyphosphate and glass flake pigments were evaluated as potential corrosion inhibitors. The inhibitive properties of Aluminium polyphosphate have been shown to reducethe rate of coating delamination via cathodic disbondment. This is proposed to be linked to the production of partially/insoluble precipitates that limit the migration of electroactive species. Aluminium polyphosphate has also shown to increase the initiation time required to form filaments during the filiform corrosion process. Glass flake had little influence on the rate of cathodic disbondment but was shown to limit both the initiation and propagation of filaments during filiform corrosion.

Declarations

1. This work has not previously been accepted in substance for any degree and is not being concurrently submitted in candidature for any other degree.

2. This thesis is the result of my own investigation, except where otherwise stated. Other sources are acknowledged by footnotes giving explicit references.

3. I hereby give consent for my thesis, if accepted, to be available online in the University's open access repository and for inter-library loan and for the title and summary to be made available to outside organisations unless a bar has been put in place.

4. I certify that I have followed the university's procedures around ethical practice for the research.

Signature: 

Date: 21/06/2021

Table of Contents

Acknowledgements

I would like to thank and acknowledge WEFO and U-POL the company partner for their full financial support from the beginning to the end of my research project.

I would like to especially thank Dr Natalie Wint who has offered me extensive support throughout the project before and after she was made my primary supervisor. Without her support, the completion of the thesis would not have been possible.

Professor Neil McMurray was another invaluable source of guidance and support who has spent many hours offering his support throughout the project. His extensive knowledge andin-depth discussions have been vital to my understanding of corrosion science.

I would also like to thank Dr Calvin Richards who has given up many hours of his own research time to support me. Without him it would have been impossible to operate and process the data gathered from the SKP. In addition, he has constantly offered his time to discuss and support my research.

I would like the thank Rhiannon Naylor, and Simon Aldersley along with the other membersof staff at U-POL who have given me this opportunity. They motivated me to develop an intensive understanding of corrosion and the vast coating industry.

I would like to thank the corrosion group within the school of engineering at Swansea University; staff and students have constantly been a source of support and inspiration. Lastly, I would like to thank my family and friends who have been there for me throughout my masters who have supported me throughout the challenges experienced during a research project.

Chapter 1 Literature review

1.1 Introduction

Steel is still regarded as the most important industrial material today and is used in all aspects of our daily lives. This is demonstrated by the global crude steel production of 1,670 million tonnes being produced alone in 2017 [1].

However, steel is subject to corrosion, a natural and costly process of destruction which is comparable to earthquakes, tornados, floods and volcanic eruptions in terms of the damage it can cause [2]. Corrosion has affected many civilizations across time and still affects us today, and even has known to limit the technical progress of civilizations [2]. This statement holds true even today when the costs of corrosion are evaluated. In a study evaluating the cost of corrosion by C. C. Technologies Inc USA, [3], the Federal Highway Agencies (FHWA), USA [4] and the National Association of Corrosion Engineers [5] it was estimated that in the USA alone, the cost of corrosion equalled 276 billion US dollars (3.1% percent of their GDP). In the UK it was estimated as 4-5% of GDP[6].

This then leads us to protective coatings consisting of organic and inorganic coatings. With organic coatings regarded as the most common means of protecting metals from corrosion in industry today due to their low cost and ease of application [7,8]. Coatings have been used for thousands of years for decorative and identification purposes, with the industrial importance only fully recognised after World War II [2]. In 2000 the USA alone manufactured 3.5 billion gallons of paint with one third being used to protect and or decorate metal surfaces [2]. The cost of using organic coatings in industry is directly related to [2]:

1. The importance of the structure to be coated
2. The lifespan of the coating system
3. The environment the coating would be exposed to
4. The application and maintenance times for the coating

Most organic coating systems used in industry to protect metal substrates involve multiple layer systems. These systems have high manufacturing, and maintenance costs due to the multiple coating products required and their associated cure times.

A potential replacement for multilayer systems is direct to metal coatings. They incorporate the key properties of a multilayer system within a single product [9]. While they only account for a small percentage of the market; they are one of the fastest growing subsegments [10]. Moreover, with the recent developments of polyurethane topcoats the potential to develop a standalone coating arises.

Therefore, the need to evaluate the performance and failure mechanisms of polyurethanes coated directly to ferrous substrates is required to produce a high-quality coating system. The following research will involve evaluating the failure mechanisms of a novel automotive based Polyurethane (RAPTOR) when directly applied to iron substrates.

The project involves firstly evaluating the recent literature around both organic coatings as well as current techniques used to evaluate corrosion driven coating failure mechanisms. Following that the use of well-established electrochemical techniques such as the scanning Kelvin probe, as well as chemically induced corrosion methods will be used to quantify and evaluate the performance of RAPTOR for two key corrosion driven coating failure mechanisms: cathodic disbondment and filiform corrosion.

1.2 Electrochemical cell

An electrochemical cell is made of four components: a cathode; an anode ,a metallic conductor and an electrolyte; [8,11]. At the anode and cathode, a series of electrochemical reactions take place. At the anode, oxidation takes place, whereas reduction reactions take place at the cathode. Oxidation is classified as the removal of electrons from a material whereas reduction is the addition of electrons. General forms of oxidation and reduction reaction can be seen in equations 1.1 and 1.2 respectively. [12]

$$M^{n+} + ne^- \xrightarrow[reduction]{} M \qquad \text{(Eqn 1.1)}$$

$$M \xrightarrow[Oxidation]{} M^{n+} + ne^- \qquad \text{(Eqn 1.2)}$$

Where n refers to the number of electrons involved and n+ is the ionisation state of the metal, and M is the species involved in the reaction. As the electrolyte is the medium which completes the cell the positively charged ions known as cations travel toward the cathode and the negatively charged ions named anions, travel towards the anode via this medium [11] .

The electrons and charged particles generated at the anode flow to the cathode, generating a current between the two electrodes. The flow of current within the cell is always from the anode to the cathode. The electrode potential is another common parameter measured it is defined as the potential of an electrode in an electrolyte as measured against a reference electrode such as the standard hydrogen or calomel electrode.[2].

Electrochemical cells generate electrical energy due to the reactions described at the anode and cathode. The energy available is calculated using the equation 1.3.

$$Electrical\ energy = Volts \times Current = -nEF \quad \text{(Eqn 1.3)}$$

Where E is the electromotive force (emf) of the cell in volts ,n is the number of electrons involved in the reaction and F is Faradays constant approximately 96485 C mol^{-1}.

1.3 Introduction to corrosion

Corrosion can be defined as a physicochemical interaction between a metal and its environment which results in changes in the properties of a metal [12] or simply as the conversion of a metal to a metallic compound [8]. Corrosion primarily affects metals due to their thermodynamic instability. This instability is due to most metals existing in nature as ores comprised of oxides sulphides and halides [13]. The metals are extracted typically with the use of a furnace and the addition of reducing agents [14,15].Once they have been extracted, the metals are said to be in a metastable state with a higher energy than their prior ore form [14,15]. With the use of Gibbs free energy and the second law of thermodynamics it can be seen that the extracted and refined metals have propensity to revert to their thermodynamically stable compounds in the form of corrosion products due to the driving force of the negative change in Gibbs free energy which is seen in figure 1.1 [2].

Where Gibbs Free energy is defined as the proportion of the total enthalpy of a system that can be converted to work [2] and the change in free energy of the system is a driving force for a chemical reaction to take place. In figure 1.1 ΔG^* stands for the free energy of activation and must be overcome for the reaction to take place. ΔG^* also determines the rate of corrosion and is influenced by factors such as temperature, humidity and the concentration of the electroactive species [14,15].

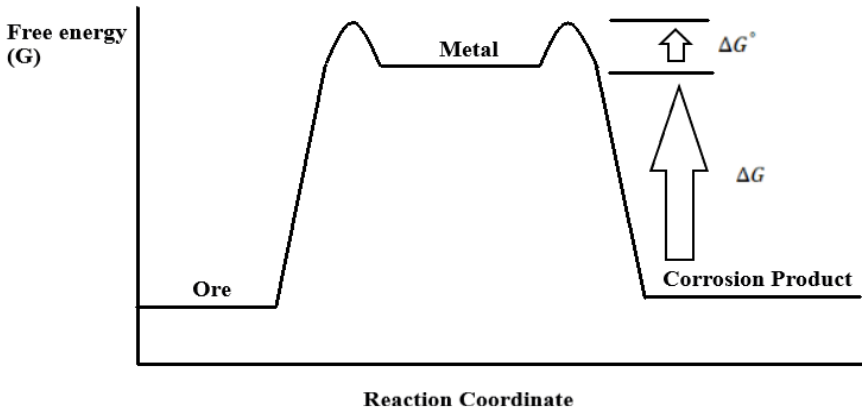

Figure 1.1 The free energy transition from a metal ore to corrosion product.

we can relate the change of free energy to the standard electrode potential of a cell by the equation below [2]:

$$\Delta G = -nFE \qquad \text{(Eqn 1.4)}$$

Where ΔG is the free energy change given in joules, n denotes the number of moles of electrons involved in the cell reaction per mole of product formed, and F is the Faraday constant.

The electrode potential of a metal in a corrosion cell is typically referred to as E_{corr} or the corrosion potential and is defined as the potential generated by the metal surface when immersed in electrolyte. The current in a corrosion cell is referred to as i_{corr} or the corrosion current and is defined as the current generated during the corrosion process as electrons are transferred from the anode to the cathode. The magnitude of the corrosion current in the system is a way of measuring the rate of corrosion and is directly proportional to the difference in potential between the anode and cathode.

1.4 General corrosion reactions

In a corrosion cell multiple anodic and cathodic sites can form on the same metal surface due to variation in the composition in the metal or from concentration differences of the surrounding electroactive species. Moreover, if the anode and cathodic sites are small and numerous this is referred to as ‘general corrosion’ whereas if the anode and cathode sites are large and discrete this is regarded as ‘localised’ [2]

As iron shall be the focus of the study, the anodic and cathodic reactions of iron will be discussed below. The wet corrosion reactions for iron at the anode are shown in equations 1.5 and 1.6 and the cathode reaction is seen in equation 1.7 [16]. The overall reaction is depicted in equation 1.8

$$Fe \rightarrow Fe^{2+} + 2e^{-} \quad \text{(Eqn 1.5)}$$

$$4Fe^{2+}(aq) \rightarrow 4Fe^{3+}(aq) + 4e^{-} \quad \text{(Eqn 1.6)}$$

$$O_2(g) + 2H_2O(l) + 4e^{-} \rightarrow 4OH^{-}(aq) \quad \text{(Eqn 1.7)}$$

$$4Fe^{2+}(aq) + O_2(g) + 2H_2O(l) \rightarrow 4Fe^{3+}(aq) + 4OH^{-}(aq) \quad \text{(Eqn 1.8)}$$

From the anodic reactions we can see that the dissolution of the metal occurs at these sites via an oxidation reaction as well as the iron(II) cations oxidising to a higher valence . At the cathode, a reduction reaction occurs, that produces hydroxyl ions. Following these reactions, the iron(II) cations react with the hydroxyl ions to from iron hydroxide which reacts with oxygen to give red-brown iron (II) oxide which is seen in equation 1.9.

$$4Fe(OH)_2 + O_2 \rightarrow 2Fe_2O_3.H_2O + 2H_2 \quad \text{(Eqn 1.9)}$$

However, if the electrolyte solution has a low pH (<7) where H^+ ions prevail, the cathode reaction changes, :

$$2H^{+}(aq) + 2e^{-} \rightarrow H_2(g) \quad \text{(Eqn 1.10)}$$

This then results in :

$$Fe + 2H_2O \rightarrow Fe^{2+} + 2OH^{-} + H_2 \quad \text{(Eqn 1.11)}$$

$$Fe^{2+} + 2OH^{-} \rightarrow Fe(OH)_2 \quad \text{(Eqn 1.12)}$$

The resulting iron (II) hydroxide is less soluble and is then deposited on the metal surface and inhibits the further oxidation of iron to some extent [16].

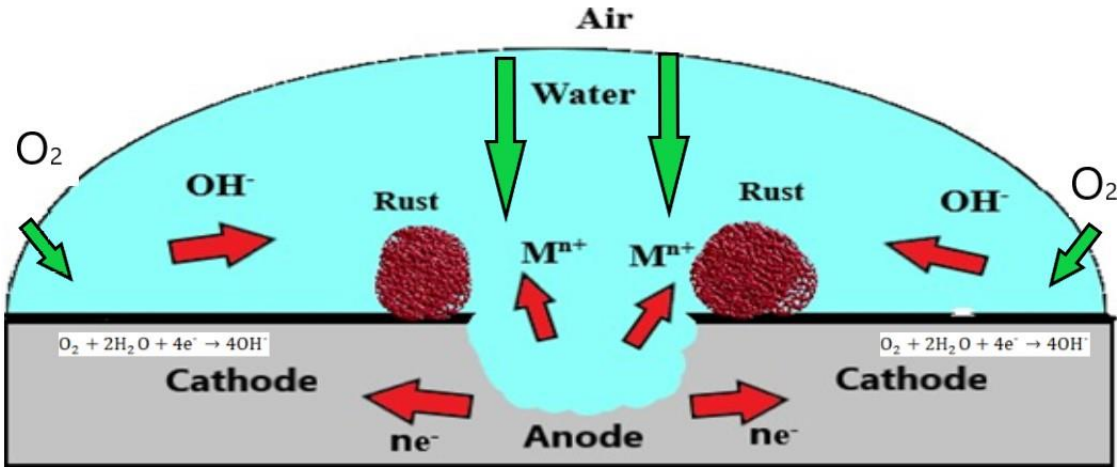

Figure 1.2 schematic of an aerated corrosion cell on a metal surface

Figure 1.2 shows how an aeration corrosion cell can form on iron from a water droplet. In the schematic the cathodic and anodic sites arise due to the difference in oxygen concentration established between the centre and periphery of the droplet. This difference can be seen by the shorter oxygen diffusion pathway at the edge of the droplet in figure 1.2 opposed to the centre .Hydroxyl ions are produced at the cathode site as previously described and they migrate towards the anode. While this occurs iron, cations are produced at the anode which combine with the hydroxyl ions to form ferric hydroxide. Iron oxide or 'rust' is deposited on the surface when the ferric hydroxide eventually dries [17]

1.5 Electrochemical series

As previously defined the electrode potential of a metal can be determined via forming an electrochemical cell with the desired metal and a bridge connected to the standard hydrogen electrode as the reference electrode. The potentials obtained are listed as reduction potentials to measure a metals ability as either a reducing or oxidising agent this list is known as the electrochemical series. The standard conditions used are a constant temperature of 298K, a pressure of 1 Atm, and a concentration of 1mol/Litre. A collection of the most common metals can be seen in table 1.1 below. The higher(positive) electrode potential is regarded as a noble metal whereas the lower (negative) potentials are regarded as a base metal [12] .

Table 1.1 Reduction potentials obtained using a Standard hydrogen electrode at standard conditions {2]

Electrode Reaction	**E° (V vs SHE)**
$Au^{3+}(aq) + 3e^{-} = Au(s)$	+1.5
$Ag^{+}(aq) + e^{-} = Ag(s)$	+0.8
$Cu^{2+}(aq) + 2e^{-} = Cu(s)$	+0.34
$2H^{+}(aq) + 2e^{-} = H_2(g)$	0
$Pb^{2+}(aq) + 2e^{-} = Pb(s)$	-0.13
$Fe^{2+}(aq) + 2e^{-} = Fe(s)$	-0.44
$Zn^{2+}(aq) + 2e^{-} = Zn(s)$	-0.76
$Al^{3+}(aq) + 3e^{-} = Al(s)$	-1.66
$Mg^{2+}(aq) + 2e^{-} = Mg(s)$	-2.37
$Na^{+}(aq) + e^{-} = Na(s)$	-2.71
$Ca^{2+}(aq) + 2e^{-} = Ca(s)$	-2.87
$K^{+}(aq) + e^{-} = K(s)$	-2.92
$Li^{+}(aq) + e^{-} = Li(s)$	-3.03

Additionally, the standard electrode potentials obtained can be related to Gibbs free energy via equation 1.4 where if the value of ΔG° is negative then the forward reaction would be thermodynamically favourable.

1.6 Standard hydrogen electrode (SHE)

The standard hydrogen electrode (SHE) is a common reference electrode used for potential measurements for example for the electrochemical series. The reversible hydrogen electrode in a solution of hydrogen ions exhibits a potential which can be taken as zero at all temperatures. The electrode itself is made of a platinum wire immersed in a solution containing hydrogen ions and saturated with hydrogen gas [2].

1.7 Nernst equation

A metal will generally not be subjected to standard conditions and in these instances the electrode potential of the metal can alter due to temperature and the activities of the chemical species. The Nernst equation seen below in equation 1.13 allows the actual potential to be calculated by including temperature and changes in concentration of reduction and oxidation products [18].

$$E = E^{\circ} + \frac{RT}{nF} \ln \left(\frac{Products}{Reactants}\right) \quad \text{(Eqn 1.13)}$$

Where R is the universal gas constant (8.31J mol^{-1} K^{-1}), T is absolute temperature (K), Products refers to the concentration of products from oxidation reactions and reactants are the concentration of reactants from reduction reactions at the electrode

1.8 Pourbaix diagrams

Pourbaix diagrams can be used to represent the stability of a metal as a function of potential and pH [2, 19]. The diagrams are constructed based on a series of calculation based on the Nernst equation discussed before as well as solubility data for the metal and its products [2]. Pourbaix diagrams are split into 3 different regions active, immune, and passive which are specific to the metal and environment[20].

1.8.1 Immunity region

This is the region on the Pourbaix diagram where the metal is said to be 'immune' and not expected to corrode. This would occur when the concentration of the metals ions in solution was below 10^{-6} $mol.dm^{-3}$ [20]

1.8.2 Active/Corroding region

The active region is where the metal is expected to freely corrode =. The metal will freely corrode if its metal ion concentration in solution is above the threshold value of 10^{-6} $mol.dm^{-3}$ [20]

1.8.3 Passive region

The passive region is where the metal forms a passive oxide film. If this film is insoluble an adherent to the metal surface it can inhibit or reduces the further dissolution of the metal [2,20].

While these diagrams provide useful information of the stability of metals in varied environments and potential there are some limitations. Firstly, these diagrams are based purely on thermodynamic data and do not provide any information on the rate of the reactions. Next it is assumed that the system is in equilibrium for that specified environment and thus factors such as temperature and velocity are not considered. Lastly Pourbaix diagrams only deal with pure metals which limit their use in industry. A simplified Pourbaix diagram for iron can be seen below in figure 1.3

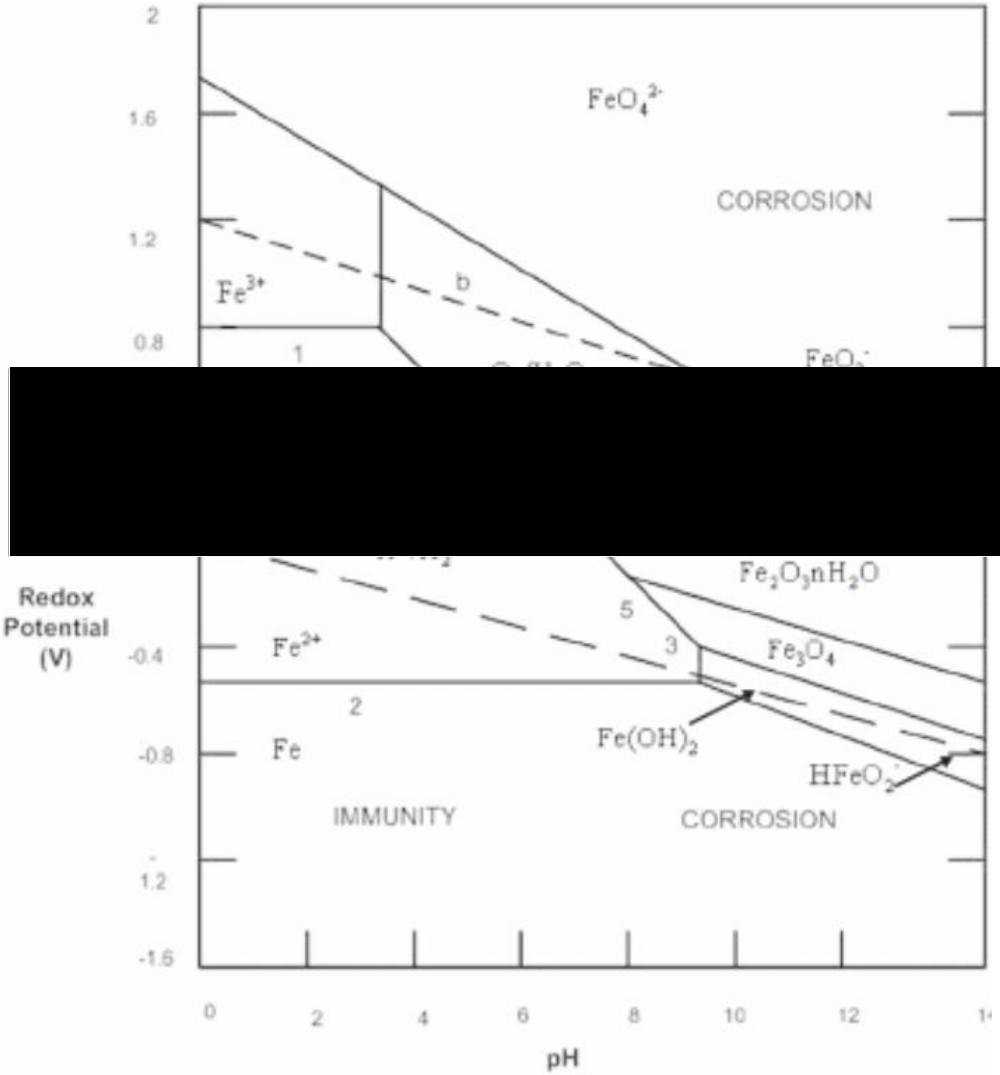

Figure 1.3 Pourbaix diagram for iron showing regions of immunity, passivity, and activity. With the dotted lines showing the stability regions of water [2]

1.9 Corrosion Kinetics

As previously discussed, when a wet corrosion cell is established, cathodic and anodic reactions can take place on the metal surface. The current density (current per unit area) is in indication of the rate at which corrosion occurs. Once the reaction reaches equilibrium, and assuming no external potential is applied, the net current will equal zero and the contribution to the current from the anode and cathode will be equal [18,21].

$$i_a = -i_c = i_0 \quad \text{(Eqn 1.14)}$$

For equation 1.14 i_a is anodic current while i_c is the reduction current and i_0 is referred to as the exchange current.

However, to describe the corrosion rate outside of equilibrium conditions we must evaluate the difference between the actual non-equilibrium and equilibrium potential values [22]. The overpotential (η) is a measure of how far the electrode potential shifts from the equilibrium potential. Depending on which direction the shift is, it can be an anodic or cathodic overpotential. The over potentials can be calculated using equations 1.15 and 1.16.

$$\eta_a = E - E_{eq} \quad \text{(Eqn 1.15)}$$

$$\eta_c = E_{eq} - E \quad \text{(Eqn 1.16)}$$

Where E is the measured potential and E_{eq} is the equilibrium potential.

The Butler-Volmer equation seen in equation 1.17 can be used to produce a plot of potential as a function of current density:

$$i = i_0 \, exp\left(\frac{(1-\beta)\eta F}{RT}\right) - exp\left(\frac{-\beta\eta F}{RT}\right) \quad \text{(Eqn 1.17)}$$

Where the first exponential term $(exp\left(\frac{(1-\beta)\eta F}{RT}\right))$ describes the anodic reaction, whilst the second term $(exp\left(\frac{-\beta\eta F}{RT}\right))$ is for the cathodic reaction. The $1-\beta$ and $-\beta$ are the energy fractions of the reaction. If the external potential is large enough the Butler-Volmer equation can be simplified for either anodic or cathodic polarization. The equation can be expressed in the general form as seen below in equation 1.18 :

$$\eta = a + b \log i \quad \text{(Eqn 1.18)}$$

Where b is the Tafel slope for anodic or cathodic reactions and is determined by equations 1.19 and 1.20.

$$b_a = \frac{2.3RT}{(1-\beta)F} \quad \text{(Eqn 1.19)}$$

$$b_c = \frac{2.3RT}{-\beta F} \quad \text{(Eqn 1.20)}$$

Where b_a corresponds to the anodic reaction and b_c for the cathodic reaction.[21]

1.10 Evans Diagram

The Butler-Volmer equation can be used to produce a plot of potential as a function of current density. Figure 1.4 below shows an example plot for the iron/ferrous solution half-cell. Where the plot (dotted lines) contain two branches, the iron anodic reaction at the top and the iron cathodic reaction at the bottom. The solid lines are extrapolations of the linear portions of the anodic and cathodic branches for the potential-logarithmic current density plot. The intercept is the point where the current is equal to the exchange current and the corresponding potential is known as the reversible or equilibrium potential.

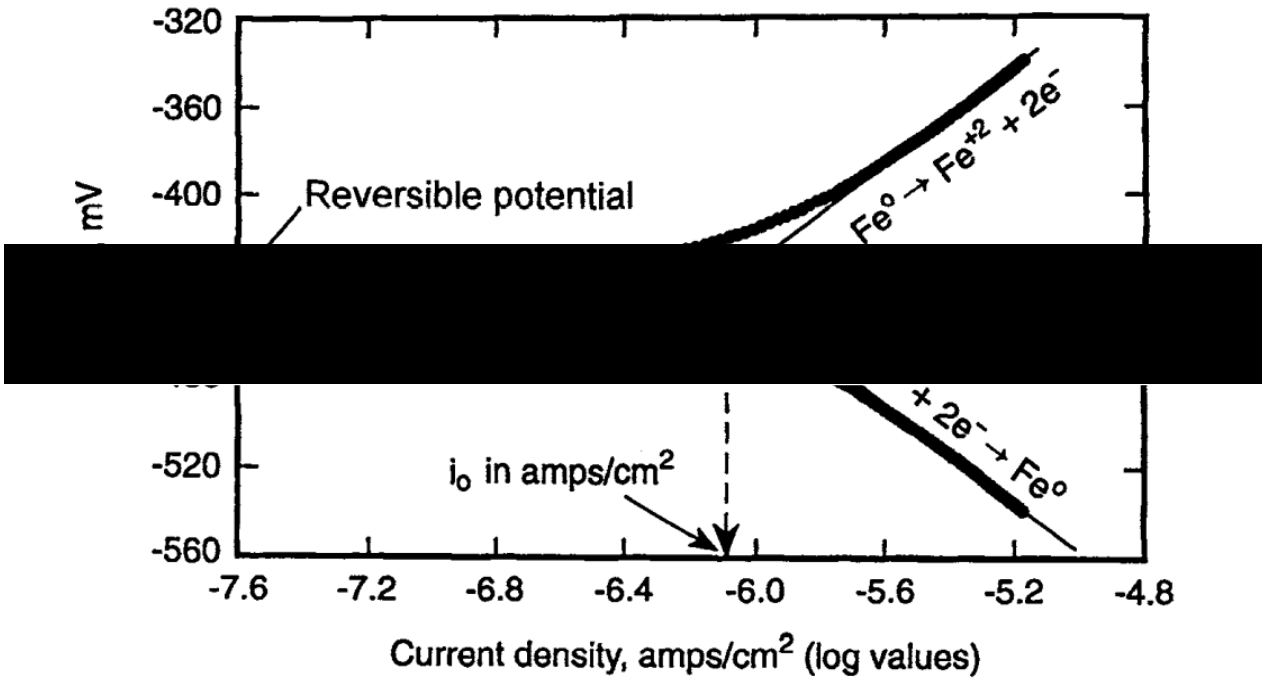

Figure 1.4 potential vs current density for iron/ferrous solution half-cell reaction [21]

A common simplification to the plot is to only show the solid lines on the potential-logarithmic current density plot in figure1.4 and this simplified plot is known as an Evans diagram named after U.R Evans who first proposed the simplification [23]. An Evans diagram is a simplified plot of the anodic and cathodic reaction curves for an electrochemical system; that can be used to describe a metal corrosion system. The electrode potential (volts) is shown on the y-axis with the reaction rate (amperes) shown on the x-axis.

Figure 1.5 shows an Evans diagram for a metal immersed in an aerated electrolyte. As the metal corrodes at the anodic site, electrons begin to flow to the cathodic site. As the corrosion reaction proceeds the potential at the anodic region becomes less negative and results in an upward shift of potential away from the equilibrium potential (η_a). The opposite effect is seen at the cathodic site represented by η_c. At the intersection of the two Tafel slopes is the point where both the anodic and cathodic current densities are and defines the free corrosion current density. Additionally, as the free corrosion potential (E_{corr}) is dependant to the corrosion current any given corroding metal will adopt a unique potential.

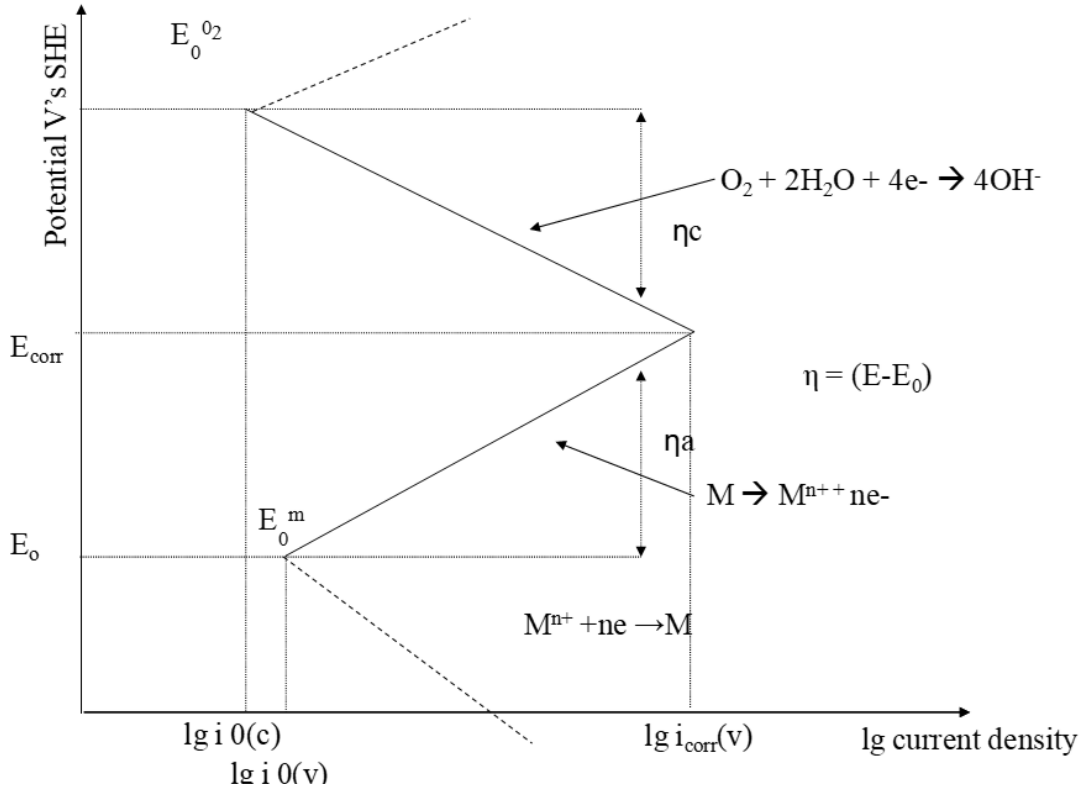

Figure 1.5 Evans diagram for a metal immersed in an aerated neutral electrolyte.

1.11 Polarization diagrams

Polarization curves describe the potential-current density behaviour of a system which is obtained by applying an external potential or current [2].

On a polarization diagram the thermodynamic driving force (potential) for the electrochemical reaction is plotted on the y-axis while the kinetics of the reaction (current) is plotted on the x-axis. Polarization diagrams can be used to combine the effects of thermodynamics with the kinetics of the corrosion reaction such as to determine the rates for metal dissolution at the anodic regions of a corrosion cell.

1.12 Introduction to electrochemistry

Electrochemistry is a branch of science that is heavily seen in industry as well as in nature such as the electroplating of commercial products to the degradation of metals. Wolfgang Schmickler defined electrochemistry as the study of structures and processes at the interface between an electronic conductor (the electrode) and an ionic conductor (electrolyte) or at the interface between two electrolytes [24]. Ultimately the focus of electrochemistry is the study of the properties of ionic conductors and of electric circuitscontaining ionic conductors [25].

1.13 Scanning Kelvin Probe (SKP)

The scanning Kelvin probe (SKP) is a non-contact, non-destructive vibrating capacitor that is used to measure the work function difference between a conducting material and the probe. The SKP does not require electrolyte contact between the reference and working electrodes which allows it to investigate corrosion under organic coatings and thin films.

The modern SKP setup and procedure used to measure the under-film corrosion seen in this study was developed and explained by Stratman [26]. From this paper it was suggested that the Volta potential of a polymer coated metal surface can be determined by the corrosion potential of the substrate. Therefore, it has the ability to map changes in localised potential distributions across a surface caused by various surface or interfacial electrochemical phenomena under intact organic coatings.

The SKP apparatus and experimental setup are described in detail in section 2

1.14 SKP Theory

The vibration probe is positioned above the sample where the probe and the sample mirror the two plates of a parallel plate capacitor. The air gap and insulating polymer covering the sample form the non-conducting medium present between the 'capacitor plates. Capacitance (C) of a parallel plate capacitor is calculated following Equation:

$$C = \frac{\varepsilon\varepsilon_0 A}{d} \quad \text{(Eqn 1.21)}$$

Where A is the plate area, d the distance between the plates, ε_0 is the permittivity of a vacuum and ε is the dielectric constant of the capacitor dielectric. The probe electrode is vibrated relative to the samples surface in a sinusoidal form at a frequency (ω) in a way that the distance (d) between the plates varies with time. This is expressed as:

$$d = d_0 + d_1 \sin(\omega t) \quad \text{(Eqn 1.22)}$$

Where d_0 is the mean plate separation, and d_1 is the amplitude of vibration. The vibration of the probe produces a periodic fluctuation of C. Where any Volta potential difference (ΔV) that exists between the probe tip and sample surface, causes the periodic fluctuation in capacitance to generate an alternating current in the external circuit [27]. As the working electrode and reference electrode are connected by an external circuit the fermi levels of both materials are identical and the sum of the energies necessary to transfer an electron from the working electrode through the several interfaces into the reference surface are zero [27].The open circuit value of ΔV is not directly obtained from the Kelvin probe signal current. The use of a nulling technique is used to adjust the value of the external Direct current bias voltage E, such that the signal current equals zero. Then if the assumption is made that E_{KP} = $-E_{i=0}$ then the E_{KP} is equivalent to the Kelvin probe determined ΔV.

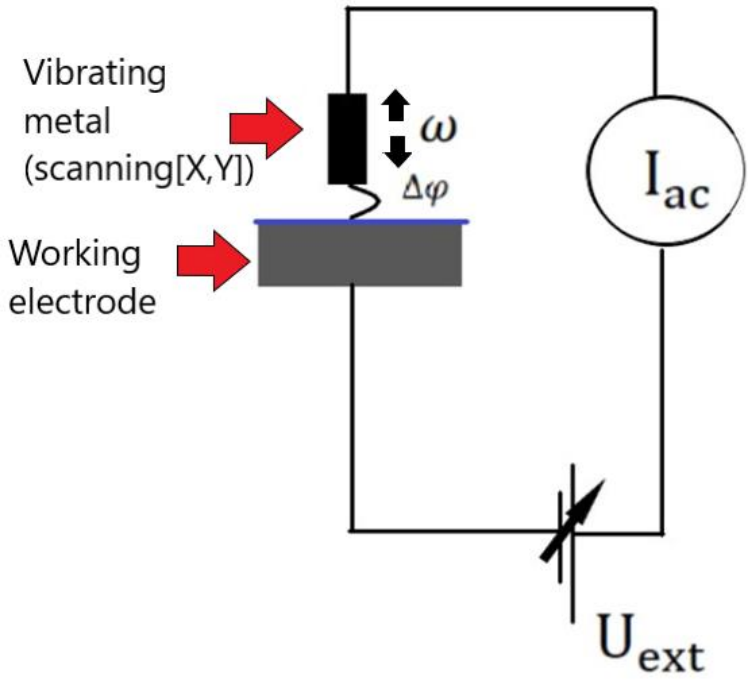

Figure 1.6 schematic diagram for the SKP. Where the blue line above the working electrode is the electrolyte. $\Delta\Psi$ is the measured volta potential difference between the probe and sample and ω is the frequency of vibration.

1.15 Coatings and paints

A coating is a thin layer of material applied on a substrate to change its appearance, protect it from damage, or to stop the substrate interacting with its environment and other substances [28]. Paints, which are primarily organically based, protect metals by interposition of a continuous inert and adherent film between the surface of the metal and its environment. This film has been shown to possess a high electrolytic resistance that impedes the movement of ions between the anodes and cathodes at the metal surface. This is further supported by the fact that most organic coatings have been shown to be permeable to oxygen and water in the vapour phase at levels greater than required for the bare substrate to corrode [29]. Therefore, for undegraded organic coatings the rate determining step is not oxygen or water diffusion through the coating [29]. This is different for metallic based coatings on metal substrates which rely on the electrochemical relationship between the environment, coating and base metal [7]. Polymeric or organic coatings consist of thermoset and thermoplastics. Where a thermoplastic can be re-melted after its polymerisation reaction and the thermoset cannot [12].

1.16 Multi layered paint systems

Traditional thermoset coatings do not have the adhesion, barrier properties and surface appearances required for industrial applications in corrosive environments [28]. Thus, multi layered paint systems are used for protection. A multi-layered coating paint system consists of multiple layers built up on a metal surface to protect it from degradation from the environment figure 1.7 shows a general cross section of a multi-layered coating system.

1.16.1 Interfacial oxide

Most metals except gold and silver and a few select metals will have an interfacial oxide layer at metal/organic coating interfaces [30].This interfacial oxide adds another layer in the multilayer system and can affect the adhesion properties of the coating to the substrate which in turn will affect its overall corrosion resistance. Adhesion is defined as the mechanical strength between two different objects or materials [31]. One of the primary requirements for a strong adhesive strength is that the paint comes into direct contact with the base metal or underlying layer [12]. The properties at the interface between the coating and substrate are dependent on the interaction of functional groups present on the substrate and the coating. Moreover, the atoms on a surface can be acidic or basic in nature, where the acid is regarded as an electron acceptor and a base is an electron donor [32]. If contaminants are present, they could form organo-metallic bonds with the substrate which could reduce the adhesive strength [33,34].

1.16.2 Pre-treatment

Pre-treatments are a common form of corrosion protection which can be applied across a wide array of substrates including iron, steel, zinc and aluminium substrates to name but a few [7].The chemical treatment can be used to change the chemistry of the substrate surface to increases its reactivity in regards to promoting adhesion between the surface and the subsequent coatings; or can deposit a thin (2-7 μm dry film thickness) precipitate layer of inhibitor close to the metal surface to halt or limit the corrosion reaction[12,28,35]. However, most pre-treatments do not provide sufficient protection to a metal substrate on their own.

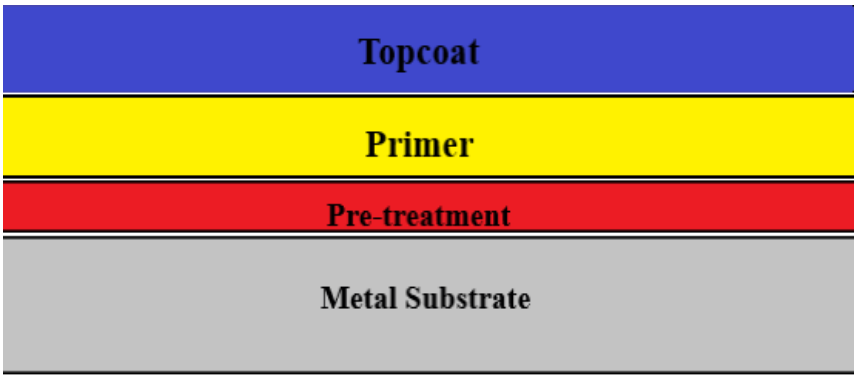

Figure 1.7 Cross section for a multi-layer coating system on a metal substrate

1.16.3 Primer

The primer is applied directly on top of the metal substrates natural occurring oxide film or the subsequent pre-treatment layer. Many industrial primers consist of epoxy-based paints that are used prior to midcoat/topcoat applications to [36-39] :

1. Inhibit corrosion of the metal from discontinuities in the paint system
2. To resist mechanical damage to the paint system
3. To provide adhesion to the substrate and to subsequent coating layers
4. To provide an inactive coating layer next to the metal surface
5. To provide corrosion inhibitors close to the metal surface
6. To add to the overall aesthetic appearance of the metal by reducing surface roughness

The thickness of a primer layer can vary depending on the number of layers and the type of primer used. Most layers reach a dry film thickness of 40-80µm and are applied in 2 coats leading to a total thickness of 80-160 µm [12].

1.16.4 Mid/Topcoat

The mid or topcoat are the coatings that are applied after the primer phase and can consist of different coatings or multiple layers of the same coating. This layer is applied on top to provide durability and barrier properties to the overall coating system [28,35]. The layer directly on top must provide both the aesthetic properties as well as have a high level of UV resistance to protect the subsequent layers from damage [28,35]. The typical dry film thickness for the coating layers above the primer range from 40-240 µm [12].

Additionally, the advantages of a multilayer coating system consisting of an epoxy primer and polyurethane finish coating applied to a steel substrate has been shown in previous literature [40]. The study showed the multilayer coating system provided strong protection to the steel from atmospheric corrosion, as well as resistance to coating delamination from defects in the coating .The primer provided good adhesive properties to the system which in turn limited the effects of coating delamination [40]. The Polyurethane topcoat provided a good aesthetic finish, hardness and durability, and UV radiation protection to the primer below [40].

To conclude while multilayer coating systems can provide corrosion protection to metal structures care must be taken when selecting the different coatings. Consideration of the different formulations must be evaluated as their different polymer structures and chemical formulations could affect the overall performance of the system. For example, different solvents in varying coatings could compromise the integrity of the adjacent coating layer resulting in loss of adhesion [12].Lastly, one must consider the thickness of each layer in the system as thick paint films while offering a thicker barrier between the metal substrate and environment can result in cracks due to internal stresses [41].

1.17 Direct to metal coatings (DTM)

A direct to metal coating or DTM is a type of paint or coating which can be directly applied to a metal substrate either as a single application or in multiple phases without the use of primers or other coating systems [30,42]. DTM coatings are typically classified into two categories solvent-based coatings or water-based coatings [40]. DTM coatings are currently used where surface preparation is not possible or in low quality applications due to their limited resistance to corrosion driven coating failure and corrosion failure when compared to traditional multilayer systems [42]. However, due to the advancements in industry topcoats there is potential to develop new DTM coatings that will lead to the reduction in costs by reducing labour times associated with curing different coating layers as well the formulation and procurement of additional coatings and surface pre-treatments [40]. Therefore, any DTM coating must possess the key properties of a multilayer coating system which include its resistance to coating delamination, resistance to atmospheric corrosion, resistance to UV radiation, hardness, and the aesthetic appearance achieved by industry topcoats in order to be considered as an option for wide spread industrial applications [40].

1.18 Polyurethane coatings

As the focus of the study is to evaluate the failure mechanisms of RAPTOR when directly applied to a ferrous substrate a good understanding of the coating's chemistry is required. The first major development of polyurethane coatings was observed in 1849 by Charles-Adolphe Wurtz a chemist who reacted aliphatic isocyanates with hydroxyl compounds to form urethane compounds [43]. Following from this, Bayer et al pioneered the polyaddition polymerization reaction by reacting polyisocyanates with hydroxyl or amine compounds which has led to the development of the modern polyurethane coating seen in industry today [43,44]. The word 'Urethane' is a common phrase for the compound ethyl carbamate and concerns the urethane linkages with the polymer chain of these coatings formed via the reaction of isocyanates and active hydrogen compounds [51].Therefore, a polyurethane coating is defined by the presence of a urethane group present, irrespective of the composition of the rest of the molecule [46].

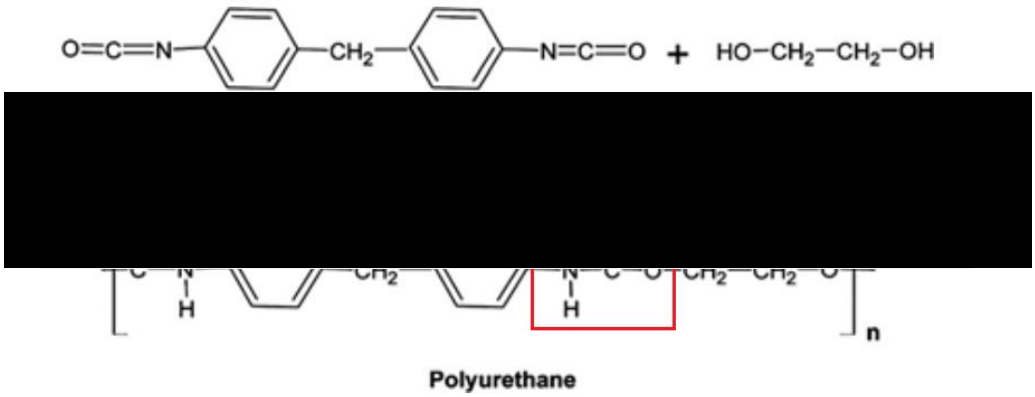

Figure 1.8 The common reaction to form a polyurethane. With the urethane linkage shown by *the red square [47]*

1.19 Adhesion and covalent bond formation of Polyurethane coatings

Polyurethanes have been attributed to have strong adhesion to metal oxides. This strong adhesion is typically attributed to the formation of chemical bonds between the molecules of the adherent and the substrate [40,48]. An understanding of the high level of adhesion is important as it will determine the performance of the coating when directly applied to a metal substrate as well as how to maximise its corrosion resistance. It is the reactivity of isocyanates with active hydrogens that forms the basis of urethane synthesis. The polymerization reaction that results forms a polymer rich in polar functional groups that allow for strong interactions with metal oxides.

In addition, to forming urethane linkages the isocyanate groups can also form condensation reactions with metal hydroxyls to form esters; which would add to the overall adhesion of the coating/metal interface [49,50,51,52].As the polyurethane is rich with polar functional groups the formation of a covalent bond between nitrogen and the metal surface as well as the formation of a covalent metal-oxide urethane linkage occurs [48,49,53].

1.20 Corrosion inhibitors

A corrosion inhibitor is a substance that when added to an environment, reduces the corrosion rate of a metal by changing the rates of the electrochemical reactions [54]. The inhibitors are primarily added in small quantities to pre-treatments or coatings that are close to the substrate [35,54]. There are two general classes of corrosion inhibitors: anodic or cathodic.

1.20.1 Anodic inhibitors

An anodic inhibitor works by increasing the polarisation of a metal surface via the formation of a passive film or a salt layer of limited solubility which influences the reaction at the anode of the corrosion cell formed [35,54]. Anodic inhibitors themselves can be split into two types, precipitation inhibitors and oxidising agents [55]. Precipitation inhibitors are anions that react with metal cations generated via the corrosion dissolution process and lead to the formation of a passive salt film [55]. Oxidising agents or cathodic depolarisers increase the efficiency of the oxygen reduction reaction which shifts the free corrosion potential of the metal substrate thus causing passivation [35]. Both processes reduce the corrosion current whilst increasing the free corrosion potential of the metal [54].However, a major downside to anodic inhibitors is that localised accelerated corrosion can occur if the concentration is too low and thus anodic inhibitors are often labelled as ‘’dangerous inhibitors’’ [12]. This can be seen in figure 1.9 where the addition of the inhibitor has caused the corrosion potential to increase which in turn increases the current increasing the rate of corrosion.

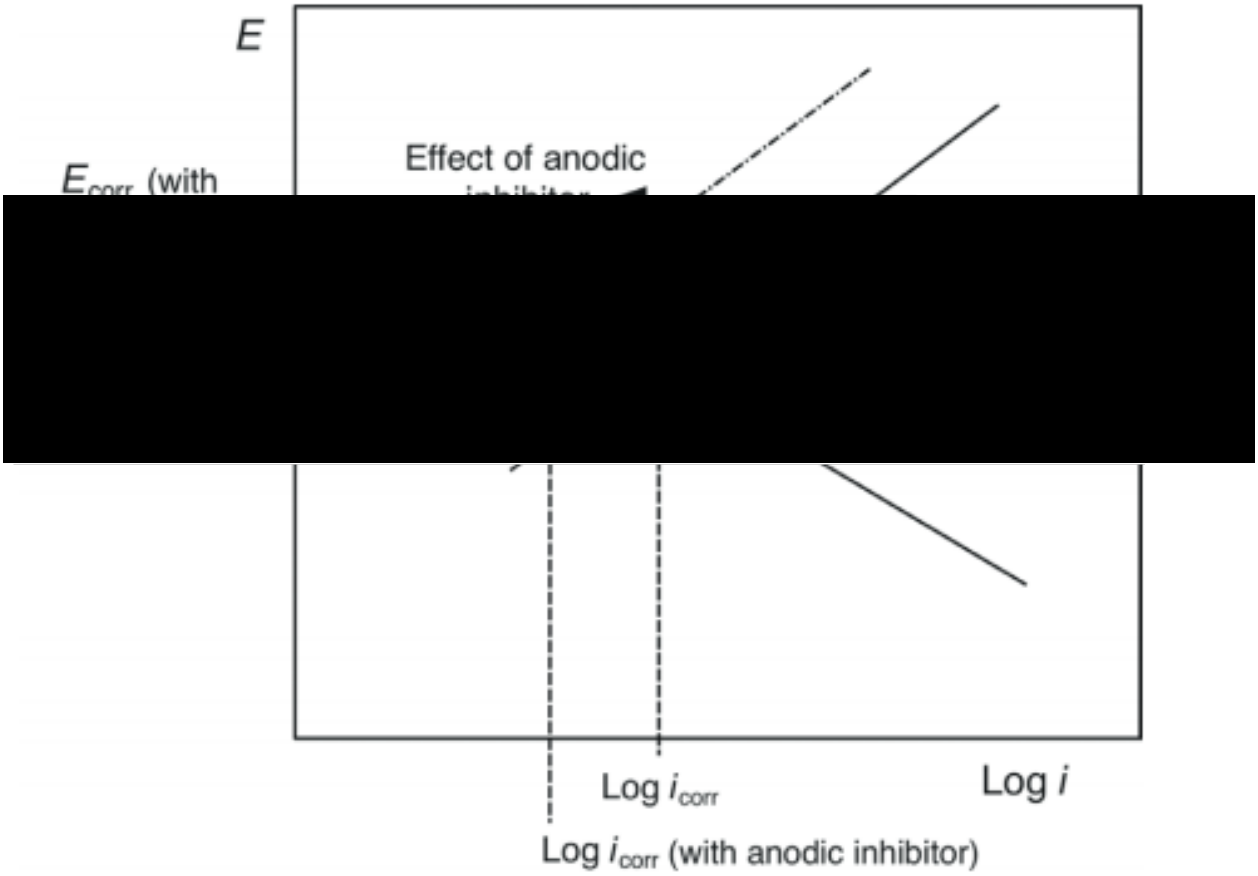

Figure 1.9 Corrosion potential vs corrosion current plot showing the shift caused by an anodic inhibitor [12]

1.20.2 Cathodic inhibitors

The main principal of cathodic inhibitors, regardless of their type, is that they increase the cathodic polarisation of the metal surface thus resulting in a decrease in both the free potential and corrosion current [35].This can be seen in figure 1.10.Cathodic inhibitors can be split into two different groups: precipitation inhibitors which form a passive film at the cathodic site, or inhibitors that affect the cathodic reaction rate [35]. Cathodic precipitation inhibitors reduce corrosion by reducing the thermodynamic driving force for corrosion as well as the cathodic area [35]. One major difference between cathodic inhibitors and anodic inhibitors is that even if a small amount of a cathodic inhibitor is added, it will still reduce the rate of corrosion to a degree without raising the energy of the system, which occurs for anodic inhibitors[12,35].Common cathodic inhibitors used in industry are Zinc salts, polyphosphates and phosphonates. The zinc salts form zinc hydroxide which is precipitated at the cathode and increases the pH which reduces the rate of the cathodic reaction while the other two form protective layers [12].

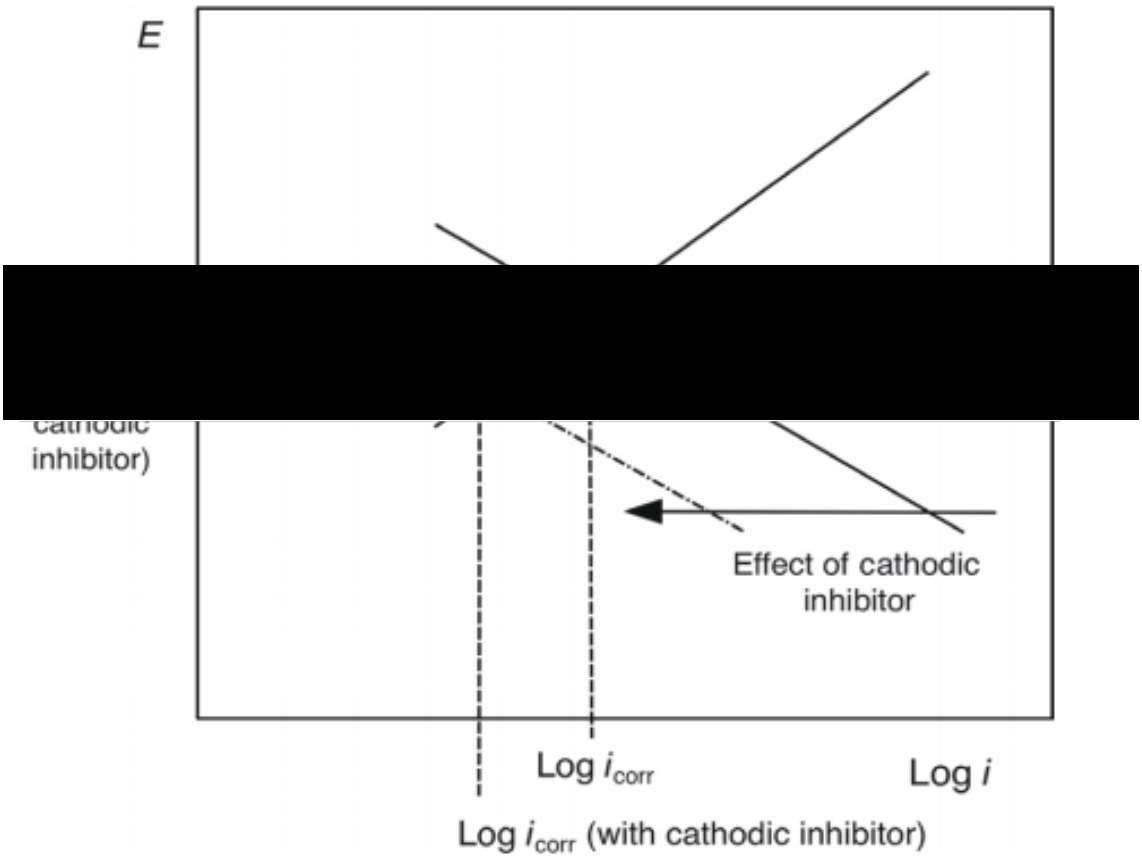

Figure 1.10 Corrosion potential vs corrosion current plot showing the shift caused by a cathodic inhibitor [12]

1.20.3 Mixed inhibitor systems

Mixed inhibitors systems involve mixtures of both anodic and cathodic inhibitors or an inhibitor supresses both the anodic and cathodic reactions [12,35]. The extent and direction in which the polarisation curves shift, will be dependent on the concentration and ratio of inhibitors present in the coating or system [35]. A very effective mixed inhibitor that was traditionally used is hexavalent chromium which forms an insoluble passive film. However, due to its carcinogenic properties its use in industry is being phased out apart from specialist applications such as aerospace [35]

1.21 Pre treatments

As previously discussed, pre-treatments can be applied to metal substrates prior to subsequent coating layers. These pre-treatments offer a layer of corrosion protection close to the substrate and helps to promote strong adhesion of further coating layers [7]. Commonly used pre-treatment systems are referred to as conversion coats.

Conversion coats convert the natural oxide on a metal surface into a different metal oxide or salt [56]. These coatings can be very thin and offer a film that is integral part of the metal/metal oxide surface and can form an electronically nonconducting layer which improves the corrosion resistance of the metal [6]. Phosphating is a conversion coating that is primarily used on iron, steel and zinc substrates. Although it is not enough on its own to protect the metal substrate, it does offer a good base for impregnation with paint enamel and oils. The coating is heavily absorbent and can retain oils for extended periods which can exclude moisture and provide lubrication if desired [7]. Moreover, surfaces that are to be painted can be subjected to a fast, thin treatment which additionally anchors the paint film to supress corrosion [7].

1.22 Silanes

Coating systems can be improved by the addition of functionalized silanes which have been widely used as reactive coupling agents for improving the adhesion of organic coatings applied to steel substrates [57]. Alkoxysilanes are an example of a good coupling agent which assists in the adhesive bonding between dissimilar surfaces which in turn allow for better bulk and interface properties for the multilayer system [58]. Moreover, vinyl silanes improve wet adhesion of a range of organic coatings such as alkyd, amino coatings while epoxy silanes can be used for polyurethane coatings [59].

1.23 Glass flake

Glass flake is an inorganic material which has shown excellent chemical resistance and aging resistance in a range of anti-corrosion coatings [60]. When the materials overlap in a parallel arrangement in the polymer matrix it can form an impermeable layer [60]. Moreover, researchers found that adding glass flake to coatings could increase the coatings resistance to chloride ion permeability [60].

The bridging connection observed in the coatings played a major role in the improvement of the mechanical properties of the coatings. Another study found that the addition of amino silane functional groups could improve the dispersion and arrangement of a glass flaked loaded coatings [61].

1.24 Phosphate and Polyphosphate based pigments

Phosphate and polyphosphate-based pigments are a common group of anticorrosive pigments that have shown to have a good compatibly with organic binders [62-65].They consist of the phosphate or polyphosphate anion combined with one or more cations of zinc, calcium, aluminium, lithium, magnesium, and strontium. They have been covered extensively in other literature [55, 66-80]. The phosphate-based pigments are sparingly soluble in water and therefore able to release free ions to protect the metal substrate in locations where the coating is damaged and exposed to electrolyte [55,65,75,78,81,82]. The free ions can protect the metal substrate by either passivating the surface or via forming a protective precipitated salt film which can inhibit the diffusion of aggressive species as well as electrolyte under the coating [64,65,82]. Moreover, this phosphate precipitate layer can polarise the cathodic reaction which in turn reduces the advancement of delamination in cathodic disbondment [82]. Care should be taken when adding phosphate-based pigments to organic coatings for while they do provide corrosion protection the compatibility of the particular pigment must be suitable to the formulation to maximise its performance as well as to not cause any damaging effects to the adhesion of the coating [64,83,84].

The most common used phosphate-based pigment in industry is zinc phosphate which prior to 2004 was regarded as the most important phosphate pigment in industry [73,85-87]. However, in 2004 it was classified as a hazardous substance to the environment and therefore the development of a zero or low zinc content phosphate pigment is desired in industry [80,87].

A substitution for the phosphate anion which has shown improved corrosion inhibition are polyphosphates which due to their sufficient water solubility are able to provide corrosion protection via precipitating a layer on the surface via an electrodeposition process which has been covered extensively [72,73,88-93].

Polyphosphates offer better inhibitive performance than their phosphate counterparts due to the higher phosphate content ,increased solubility of the phosphate ions as well as the barrier properties of the salt film formed on the metal substrate. Which are all dependent on the various polyvalent metal cations that could be added [19,72,92,94,95].

Zinc aluminium polyphosphate (ZAPP) is an example of a pigment that showed better corrosion resistance in epoxy/polyamide coatings when compared to conventional zinc phosphate which was primarily due to ZAPPs increased solubility [55].

Another polyphosphate pigment that has shown inhibitive prosperities is strontium aluminium polyphosphate (SAPP). Its increased inhibitive properties are due to its increased water solubility as well as its reaction with the metal substrate [65,77,79]. SAPPS have shown to provide corrosion protection to both steel substrates [73,77,79] as well as zinc alloys when added to an organic primer [65]. However, while it offered corrosion protection to zinc by the dissolution of the SAPP it caused disruption of the integrity of the coating which formed large cavities and porous networks which could lead to easy pathways for aggressive species to reach the metal underneath [65]. However, the dissolved SAPP did provide active protection of the zinc as well as formed insoluble corrosion product or a precipitated salt film which was formed by the reaction of the corroding zinc and SAPP which in turn filled any cavities formed by the dissolution of the inhibitive pigment in the coating [65].

Lastly aluminium triphosphate is another polyphosphate pigment that could be used to replace zinc phosphate as it has shown to provide corrosion inhibitive properties. In addition to corrosion protection it could hydrolyse to produce hydrogen ions which in turn could reduce the hydroxyl production on a metal substrate. This would reduce the generation of a high pH environment under the coating which in turn would increase the service life of the coating as it would limit the alkaline attack of the interfacial oxide layer and the coating [96].

However, the natural acidity of aluminium triphosphate must be neutralised. The neutralizing substance must be carefully selected as not to form a high alkaline formulation that could result in loss of adhesion, which in turn could result in under film corrosion [97].

1.25 Coating system failures

Over time, organically coated systems suffer a range of defects which can lead to coating failures. Organic coating films, especially crosslinked coating systems, have been shown to be heterogenous in structure where the film consists of small areas termed ‘D’ or direct conduction regions while most of the film is made of ‘I’ or inverse conduction regions [29]. The D regions have a significantly lower ionic resistance than their I counterparts which is directly related to the solution that the film is immersed in. While the resistance of I regions increases as the electrolyte concentration increases. The breakdown of the painted film has been shown to occur at these sites of lower resistance. Where ultimately corrosion of the substrate primarily will occur. Differences of the resistance seen between the D and I regions has been attributed to the variation in the cross-linking density of the polymer film [29]. Moreover, the presence of D regions increase over time as the polymer film degrades or defects are introduced.

These defects can arise during the application process such as irregularity of vehicle molecules in the paint formulation, solvent residue, difference in expansion coefficients in multilayer coatings, residual stress, and poor adhesion of the coating to the pigments [98].Additionally, during manufacturing cracks, scratches, or cut edges can develop on the organic coating which leaves part of the underlying substrate exposed or will form weakened zones within the coating [99]. Damage to the coating can also be achieved via chemical attack, permeation, or UV radiation [12].Permeation, which is defined as the interaction of the polymer in its environment [12], can cause the organic coating to swell or grow in dimension which in turn can lead to softening of the polymer via plasticization [12].Plasticization can be defined as the process of changing the structure of a polymer making it less rigid. This can lead to hydrolysis occurring under the coating, which further weakens the substrate to coating adhesion [12].

Organic coatings are also susceptible to attack from moisture and chemicals, which penetrate through the coating. This is due to most industrial coatings consisting of large polymer macromolecules which in turn possess kinetic energy. This kinetic energy causes movement and thus forms space or free volume within the polymer which allows for liquids to absorb in the coating via diffusion into the molecular interstices or free volume [12].

This diffusion of moisture and even oxygen will penetrate even the most resilient coatings over time regardless of pre-existing defects [100]. Another coating failure, coating delamination, occurs when a coating peels off the underlying substrate. This process can occur due to poor adhesion of the coating as well as via several corrosion driven processes and forms the focus of this study [100].

1.26 Introduction to cathodic disbondment and filiform corrosion

Organic coatings are widely used to protect metals from corrosion in a range of industrial and domestic applications. Whilst they offer initial barrier protection, once a penetrative defect arises, electrolyte and aggressive ions can penetrate through to the metal substrate underneath . Once this begins a range of coating failure mechanisms could occur. Within this study two of the most common failure mechanisms will be investigated, these being cathodic disbondment, or filiform corrosion. Both propagate from pre-existing breaks or penetrative defects in an organic coating, which allow species from an external electrolyte to penetrate under the coating [99].

1.27.1 General Filiform corrosion (FFC)

The term filiform corrosion (FFC) was first used to describe the filaments of dry corrosion products formed on organic coated iron in humid environments in 1944[101]. FFC is a corrosion driven coating failure mechanism that has been recorded on a range of organically coated metal substrates. These include aluminium [102,103] as well as iron and steel substrates (104,105). The process is initiated via electrolyte entering through a penetrative defect in the coating such as cut edges, scribes and scratches [106] which in turn result in the formation of threadlike filaments [104]. The filaments formed are best divided in two parts the filament head, and the filament tail which can be seen in figure 1.11. Figure 1.11 shows a cross-section of a filament formed from a defect in coating. The filament head is split into two zones the deaerated region and aerated section followed by the porous corrosion product filled tail. FFC in early literature has not been reported to directly affect the mechanical integrity of a structure, and just causes visual aesthetic damage, as well as progressive degradation of the coating [107]. However, recent literature has shown that FFC can cause the delamination and degradation of organic coatings via osmotic forces [105], anodic undermining [108] and cathodic delamination [109-111].

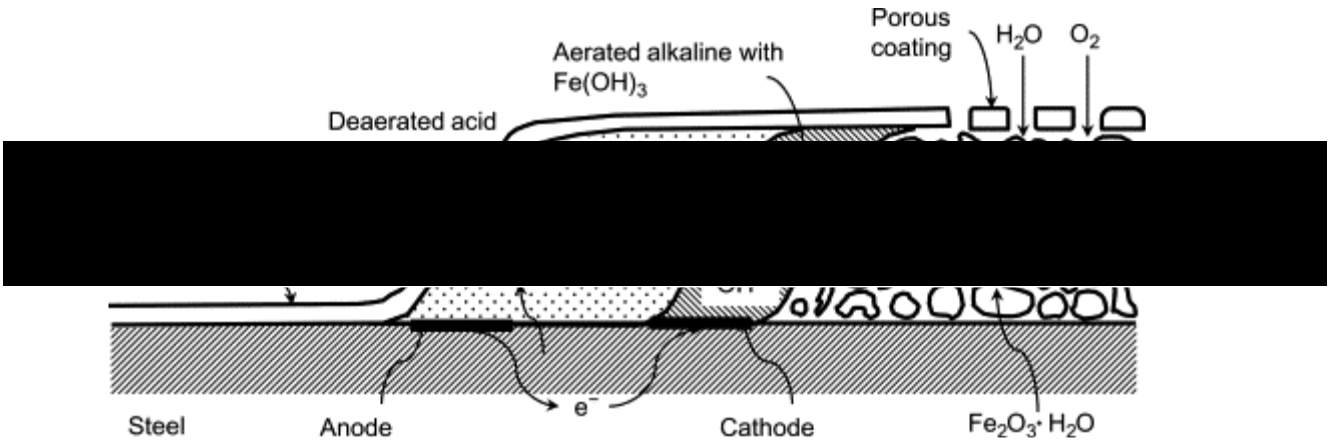

Figure 1.11 schematic of a filiform filament under a coating with the deaerated and aerated regions of the head on the left with the corrosion product filled tail shown on the right [112]

1.27.2 Mechanism for Filiform corrosion of PVB coated iron

FFC of iron occurs only at humidity ranges from 60-95% [113]. When the relative humidity approaches and exceed this maximum value of 95% blistering is typically observed. Regarding FFC on iron substrates initiated by aqueous group (I) chloride salts, previous literature show that the process occurred via a two-stage mechanism which will be discussed below [114].

Phase one

McMurray et al showed that a phase of cathodic coating disbondment precedes FFC where initiation is achieved by the addition of group (I) chloride salt electrolyte to the penetrative defect [114]. Once the electrolyte is added the group (I) cations deplete over time as they migrate to the cathodic delamination site. Cl^- anions remain near the defect. The cell is completed via the anodic dissolution of Fe^{2+} cations at the defect. Once the group (I) cations have been exhausted and the cathodic delamination reaction is halted. The second phase was then initiated by the remaining Fe^{2+} and Fe^{3+} chlorides at the defect site . Moreover, in the same study it was found that initiation using $FeCl_2$ resulted in no initial cathodic disbondment. This was attributed to the polyvalent Fe^{3+} aquocation rendered incapable of carrying current through the alkaline under film electrolyte layer [114]. Where aquocations are the state that free metal cations take form when dissolved in solution and are subsequently surrounded by coordinating water molecules.

Phase two

The initiation of FFC on iron occurs via osmosis based around the fact that it only occurs at relative humidities above 60%[113,115]. The defect allows for the entry of an electrolyte containing a soluble salt. A small liquid aggregate will then form due to the high affinity of the ions for water[109]. Iron dissolution then occurs at the anodic region releasing Fe^{2+} ions into the solution. The oxygen deficient zone forms the basis of the anode and the surrounding area forms the cathode.

Once the oxygen concentration cell is formed the front of the head anodically undermines the coated substrate allowing the propagation of the filaments. Williams et al showed that a potential gradient exists between the front and back of the filament head where anions migrate to the front and cations migrate to the back [114].

Fe^{2+} formed via oxidation of iron as seen in equation 1.23 at the front of the head migrates to the back of the head. Further oxidation of the cation then occurs as it is exposed to a higher oxygen concentration as seen in equation 1.24.

$$Fe \leftrightarrow Fe^{2+} + 2e^{-} \quad \text{(Eqn 1.23)}$$

$$4Fe^{2+} + O_2 + 2H_2O \leftrightarrow 4Fe^{3+} + 4OH^{-} \quad \text{(Eqn 1.24)}$$

The filament head formed containing the small droplet of electrolyte is maintained by the hygroscopicity of the salts therein [106]. Additionally, during cation hydrolysis from the anodic metal dissolution at the leading edge of the head, a very low pH has been shown to exist as low as a pH of 1 (seen on aluminium initiated with HCl [114] .

The tail region is as previously said is the porous region where oxygen diffuses through , The diffusion occurs through the corrosion product formed, or via the porous coating to the active filament head region [105].This results in the promotion of cathodic oxygen reduction at the back of the head whereas anodic metal dissolution occurs at the oxygen deficient region at the tip under the coating . This differential aeration drives the filaments forward [114].

1.28.1 Cathodic disbondment

Corrosion driven cathodic coating disbondment affects organic coatings applied to a range of metals including ferrous metals and Zn [116]. When the metallic substrate is exposed via a scratch or cut edge created during manufacturing ,or through in-service damage to the organic coating, the electrolyte can contact the metal and form an electrochemical corrosion cell [99] . The species for this cell includes water, oxygen, free electrons, and a counter ion to balance and maintain electroneutrality[100].Additionally, Koehler showed that for cathodic delamination to occur that these counter ions are generally group 1 cations because they only possess the hydrolytic stability and solubility at high pH necessary to support a strongly alkaline electrolyte [117].

The general mechanism for cathodic delamination on iron substrates involves anodic metal dissolution occurring at the coating defect which acts to couple with the cathodic oxygen reduction. The oxygen reduction occurs at the delamination front by the ingress of the electrolyte underneath the coating, which results in deadhesion of the coating from the metal substrate. At the delamination front the oxygen reduction reaction forms hydroxyl ions as seen by equation 1.8 which in turn form a highly alkaline environment [99]. Additionally, other reactive intermediate products are formed during the oxygen reduction and, through the chemical attack on the electrolyte forms a 'hydrogel' consisting of a network of hydrophilic polymer chains that is said to be the medium for initial underfilm ingress. Diffusion through the hydrogel is still possible but it is seen to be lower than an aqueous solution [118]. Fürbeth et al showed that the formation of a galvanic element occurs during the process due to the migration of cations from the defect to the delamination front [119]. While the external electrolyte anions remain localised to the defect zone [118].

As the SKP is one of the key techniques used to demonstrate and evaluate the cathodic disbondment of polymers from metal substrates a schematic of a cathodic delamination cell and a typical SKP potential plot will be used to explain the different regions.

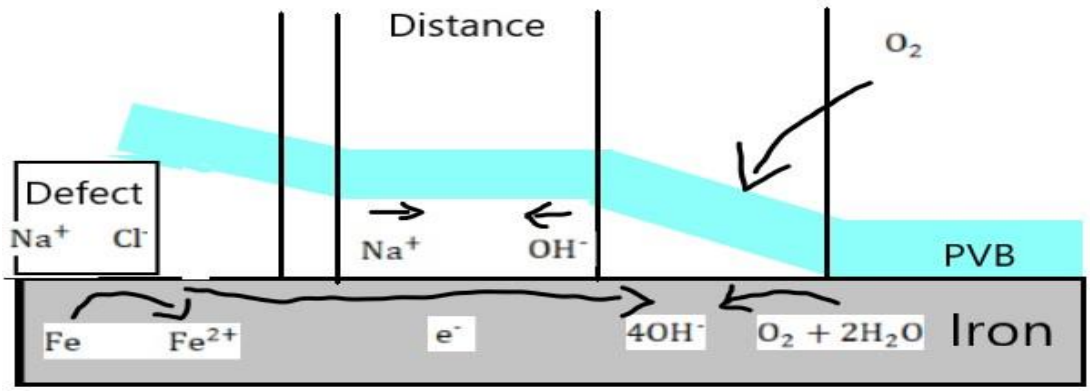

Figure 1.12 schematic representation of the E_{Corr} measured in relation to a delamination cell

The four main regions are as follows:

1. The defect region: where anodic metal dissolution takes place.
2. Region of gradual potential increase: this results from ohmic resistance to the galvanic current linking the delamination front to the defect.
3. Cathodic delamination region: observed as a sudden step in potential, where the reactions responsible for the loss of coating adhesion occur.
4. The intact interface defined by an anodic plateau. This plateau is the result of electronic conductivity from the oxide-covered substrate on which electron transfer reactions (ETRs) take place [120].

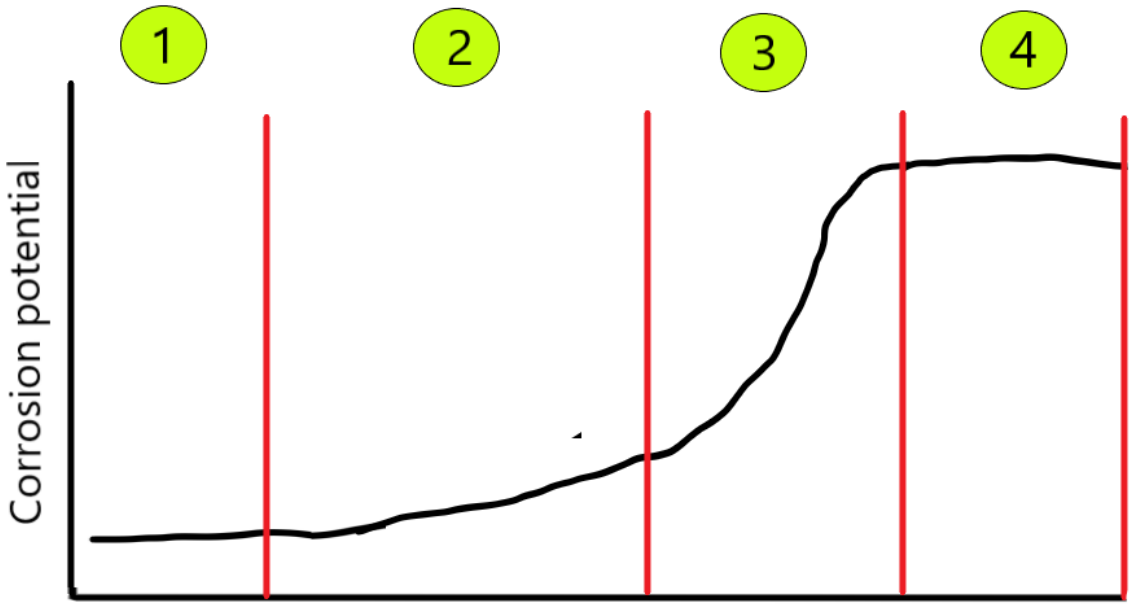

Figure 1.13 A typical SKP plot of Corrosion potential vs distance from a defect for a coating undergoing cathodic disbondment with the four regions numbered according to the listing previously.

1.28.2 Mechanisms for the cathodic delamination of polymers from iron

There are several proposed mechanisms for cathodic disbondment which vary depending on the substrate and system. However, while there may be several mechanisms of disbondment occurring simultaneously for any one given system it is the mechanism with the fastest rate that is considered the governing mechanism [99]. One of the most important suggested mechanisms derives from the work conducted in 1976 by Leidheiser and Kendig who described the formation of an alkaline environment at the delaminated region, a parabolic delamination rate kinetics, and the sharp drop in E_{corr} where the coating delamination front has occurred [121]. This will be the focus of this section. Firstly, the anodic plateaux observed in region four of the E_{corr} profile (seen in figure 1.13) results from high electronic conductivity of the iron oxides formed on the surface of the metal. At this surface the electron transfer reactions take place. Oxygen can diffuse to the metal surface and will be reduced according to the surface oxidation of the surface oxide. However, with no electrolyte present, no ion transfer reactions occur and thus no corrosion occurs. Above a certain anodic potential, the oxygen reduction rate is reduced so much that no further anodic potential shifts are seen.

When oxygen is removed from the cell a rapid decrease of the electrode potential on the intact interface is observed which is considerably slower for an iron oxide surface. This has been attributed to a large proportion of Fe^{3+} ions at the iron/polymer interface having to be transformed into Fe^{2+} which in turn limits the chance of a cathodic potential shift.

As stated in section 1.28.1 the oxygen reduction reaction that occurs at the metal-polymer interface raises the pH of the under-film electrolyte due to the formation of hydroxyl ions. The interfacial iron oxide layer is said to be stable in alkaline environments based on Pourbaix diagrams for iron and thus no anodic behaviour is observed outside the exposed defect zone. Which eliminates metal dissolution as a possible delamination mechanism for iron. However, oxidative destruction at the iron-polymer interface, with a focus on base-catalysed polymer degradation, base-catalyse hydrolysis of interfacial bonds and polymer attack can be linked to the intermediate radicals that form during the cathodic reactions which in turn lead to deadhesion of the coating [120,122].

Furthermore, previous literature have shown that many short-lived intermediates formed during the oxygen reduction reaction may be more reactive and damaging to the iron-oxygen-polymer bonds than OH^- ions [116].However the generation of a high pH is still important as many organic coatings, including both epoxy esters, polymers containing ester functionality and polymers bearing urethane and urea linkages such as polyurethane coatings, have been shown to be susceptible to hydrolysis [99]. Moreover, the work of both Castle and Watts, and Hammond show that the delamination of coatings which are more resistant to alkaline hydrolysis are more likely to delaminate as a result of interfacial separation as opposed to cohesive failure caused by the degradation of the polymer [123,124]. Thus, the rate of the oxygen reduction reaction is directly linked to the instability of this interface. Another potential mechanism for the cathodic disbondment is that the alkaline electrolyte formed physically displaces the coating at the substrate-coating interface. Alkaline solutions have shown to creep over a metal surface [117,125] and electrodes have increased wettability, with decreasing electrolyte-electrode interfacial energy. This eventually reaches a maximum at the potential of zero charge [126]. Therefore, when the pH of the electrolyte is increased above the isoelectric point the displacement of the coating via water is possible. Additionally, with the assumption that the isoelectric point is near or below neutral pH, displacement of the coating via water is promoted at pHs above 7 [99]. Lastly if the coating system relied on oxide-polymer acid-base interactions such as polar polymers such as polyurethanes for adhesion this physical displacement can lead to further displacement. [117]. To conclude based on the current literature the governing mechanism for adhesion loss on iron is due to cathodic delamination where during the process reactive intermediates are generated via oxygen reduction at the cathodic sites. These intermediates attack the polymer and lead to the breaking of interfacial bonds along with the degradation of the polymer itself. Which can lead to residual stresses concentrating at the metal-polymer interface and thus can cause peeling of the coating [127].

1.29.1 Characterisation of underfilm delamination kinetics of uninhibited coatings

To evaluate the performance of inhibitors within a coating the cathodic disbondment kinetics for the uninhibited coating must first be characterised. This section will be focused on the reported delamination kinetics for uninhibited polyvinyl butanol (PVB) coatings when applied to iron substrates with the delamination being initiated with 5% aqueous NaCl electrolyte and the experiments carried out a 93% relative humidity.

The measurable distance from the defect to the delamination front can be established using a potential plot generated by the SKP. The delamination front at any scan can be located at the inflection point where a steep potential change is observed and seen in figure 1.13. in the third zone. The time of the scan in relation to the position of the delamination front can then be used to analyse the underfilm delamination kinetics. The relationship between the delamination distance (x_{del}) and the time of the scan (t_{del}) after the addition of electrolyte is defined by equation 1.25

k_{del} is the delamination rate constant [128] and t_i is defined as the time taken for either parabolic or linear kinetics to become established. By plotting x_{del} vs $(t_{del} - t_i)^{1/2}$ allows for the delamination kinetics to be characterised. The onset of definable delamination kinetics at time t_i is the time at which interfacial ionic concentration reaches a level suitable for cathodic oxygen reduction.

$$x_{del} = k_{del}(t_{del} - t_i)^{1/2} \quad \text{(Eqn 1.25)}$$

For unpigmented PVB coatings on iron and HDG substrates the plots of x_{del} vs $(t_{del} - t_i)^{1/2}$ given by various studies have shown that linear kinetics are seen [129-131]. The rate determining step for the delamination kinetics seen have been regarded as the transport of electrolyte cations that travel from the defect parallel to the interface to the delamination front. Equation 1.25 does not consider the transport of ions penetrating the coating in a perpendicular direction. Leng et al showed that by differentiating a series of potential profiles that were taken from a typical delamination experiment on the SKP, the delamination front could be obtained exactly by the maximum value of the peak. The parameters such as height, width, and position of the peak reveal characteristics of each delamination cell formed in respect to time[118].

Moreover, as the time increased the peak height gradually decreased which was suggested to occur due to the highly alkaline corrosion conditions beginning to distribute from the delamination front to the already delaminated region making the delamination front indistinguishable over long periods of time. While the width of the peak is reported to remain relatively constant over long periods of time. To summarise, multiple quantifiable characteristics exist with regards to a delamination cells potential profile. From these profiles any effect an inhibitor addition to a coating's formulation can be determined.

1.29.2 Factors that determine the delamination rate of uninhibited coatings

The rate- determining step for the delamination of unpigmented coatings is regarded as the transport of electrolyte cations travelling from the defect to the delamination front. As with any complex process the rate-determining step is always the slowest step. Therefore, before evaluating the contributions an inhibitor may have on the delamination kinetics, the effects of the parameters that remain constant in the experiment should be understood.

1.30 Summary of literature Review findings

- Understanding of the key properties a direct to metal coating must have to match a multilayer coating system
- Understanding of two common coating failure mechanisms that can affect organic coatings on iron: cathodic disbondment, and FFC.
- Understanding of the SKP and how it has been applied in previous literature to assess the rate kinetics for cathodic disbondment for polymer coated metal substrates .
- Understanding of the effect inhibitor/ pigment additions can have on barrier and corrosion inhibition properties of coatings.
- Understanding of the polarization effects inhibitors can have on the free corrosion potential and current of an electrochemical reaction.

1.31 Aims and objectives

- To measure the change in functional groups over time to establish a percentage cure relationship for RAPTOR with the use of the FTIR
- To establish a relationship between percentage cure and resistance to cathodic disbondment with the use of adapted Stratmann cells
- To evaluate the rate determining step for cathodic disbondment of unpigmented RAPTOR with the use of adapted Stratmann cells and the SKP.
- To investigate the initiation and propagation kinetics of FFC filaments for RAPTOR
- To investigate the inhibition and rate reducing properties of aluminium polyphosphate and glass flake formulated RAPTOR with regard to FFC and cathodic disbondment

Chapter 2 Methodology and experimental setup

2.1 Experimental supplies

2.1.1 Metal substrates

Iron foil 50x50x1mm coupons of 99.95% purity provided by Goodfellow metals

2.1.2 Chemicals

All chemicals used are of analytical reagent or pigment grade.

RAPTOR Base (Polyurethane liners) provided by the UPOL

RAPTOR hardener (Isocyanate Hardener) provided by UPOL

RAPTOR Base with a percentage addition of glass 300µm glass flake Formulated and provided by UPOL

RAPTOR Base with a 5% by weight addition of aluminium tripolyphosphate

2.2 Coating Notation

For the remainder of the thesis the base unpigmented polyurethane coating will be referred to RAPTOR-A; where the A is a numerical value which represents the number of days the coating is cured for. AL P will stand for the polyurethane coating pigmented with a 5 % by weight addition of aluminium polyphosphate. Lastly GF stands for the coating pigmented with glass flake. Where both the AL P and GF coatings are cured for 7 days only at room temperature.

2.3 Metal substrate Preparation and cleaning

The iron foil coupons were abrasively cleaned with an aqueous slurry of 5µm aluminate to remove any impurities and form a uniform surface . The samples were then rinsed with distilled water and lastly degreased with acetone before drying following a method used to measure filiform on iron substrates [114]. Lastly a metal gauge thickness of $\geq$ 1mm was chosen to ensure no bending occurs during preparation and handling of the sample therefore providing a uniform straight surface for the following experiments.

2.4 Coating preparation, mixing ,drying and curing

All the polyurethane based coatings consist of 2-part systems (base and hardener) and were mixed in a 3:1 ratio by volume respectively at room temperature . Once the coating was mixed it was bar cast over the metal surface and left to flash in a fume cupboard for one hour before being left in a vacuum sealed desiccator filled with silicone desiccant for 7 days unless specified. The 15.5% w/w ethanolic solution of polyvinyl butyral (PVB) was bar cast directly onto the cleaned metal substrate and left to dry up to 24 hours to allow the solvent to flash off leaving a dry film.

2.5 Classic Stratmann cell layout

To measure a coating susceptibly to cathodic disbondment the coating is coated onto the metal substrate following the methodology outlined below. Firstly, to form the delamination cell the iron foil coupons were cleaned as previously described in section 2.3. Next a strip of clear, thin static free adhesive tape was laid down adjacent to one of the substrate edges so that it covered 1.5 cm of the metal while ensuring that a lip of tape was left hanging off the side. Then two parallel strips of 120µm thick PVC tape were laid down at right angles to the adhesive tape, leaving a 2cm wide strip of bare metal in the centre of the metal substrate. The polyurethane coating was then bar casted over the exposed metal substrate. The PVC tape acts as a height guide which formed a 70 ±5 µm dry film thickness coating layer. This was measured using Vernier callipers which were calibrated against a known distance. After the sample was cured following the procedure outlined in section 2.4 an artificial defect was formed following the method of Stratmann et al by cutting a section of the thin static free tape and lifting the residual lip [132].

Care was taken when creating the artificial defect to ensure no mechanical delamination of the coating occurred prior to the experiment. Finally, non-corrosive silicon sealant was added to the delamination cell to form a well around the newly exposed metal surface to allow electrolyte to be added. The cell before and after the defect is formed is seen below in figure 2.1

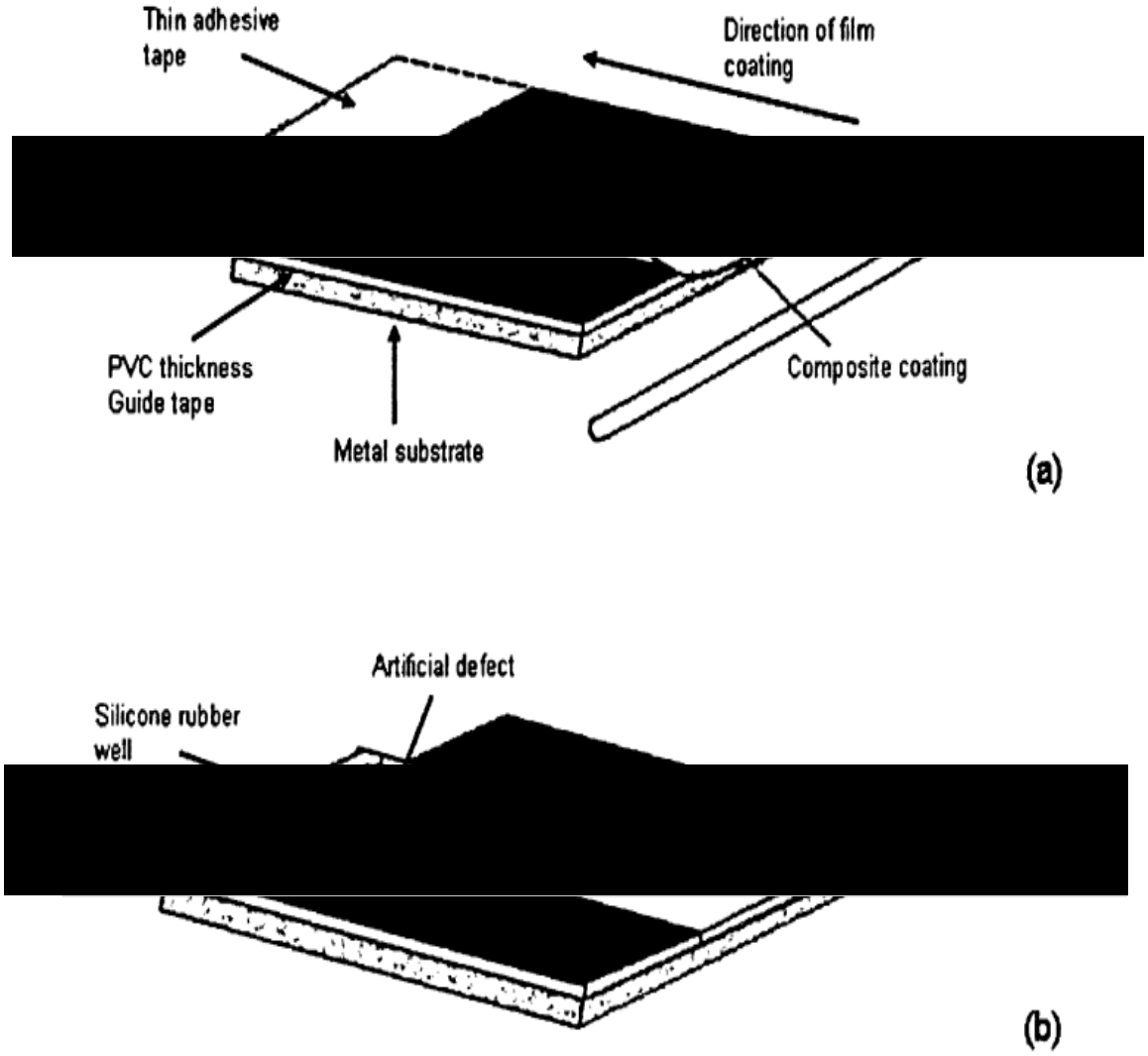

.

Figure 2.1 (a) shows the cell layout before the artificial defect is made. (b) shows the final delamination cell layout [116]

2.6 Delamination cell new methodology

The previously described classic Stratmann cell in section 2.5 was adapted to produce a novel new delamination methodology for this study. Following the application of the tape the novel polyurethane coating is bar cast over the bare strip of metal (following the direction of the arrow) in the centre of the cell. However, a 0.5 cm gap from the thin adhesive tape is left. This was achieved by applying a layer of thin adhesive tape over the 0.5 cm bare metal gap whilst coating. This was then removed after the coating was cast. Once the coating is cured the whole cell was overcoated with PVB.

This left a 0.5 cm section of iron coated with only PVB between the well and the iron polyurethane/PVB section. The PVB was then left to dry for 24 hours before creating the artificial defect as described in section 2.5 .

This new layout can be seen below in figure 2.2. This variation in the cell methodology was carried out for two purposes. Firstly, to allow the PVB calibration value that will be discussed in section 2.9 to be used for the SKP experiments. The use of PVB in delamination experiments has been covered previously and as such the calibration value has already been calculated [116] . The calibration value is dependent on the air to coating dipole therefore as PVB is overcoated over RAPTOR it is an acceptable value. The second reason is that by leaving a gap between the well and polyurethane coated section it ensured that when the artificial defect was formed that no mechanical delamination of the polyurethane coating occurred.

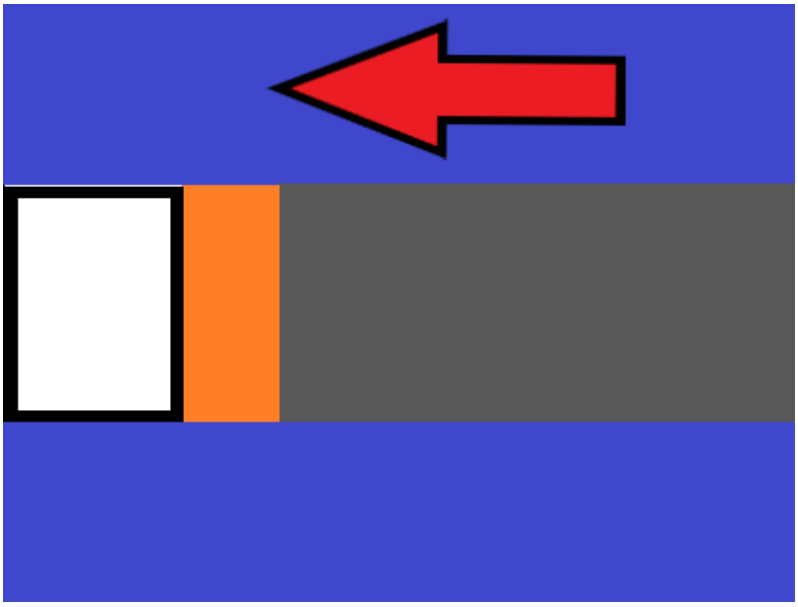

Figure 2.2 *New proposed delamination cell: Blue sections = electrical tape, Grey section = Polyurethane coating overcoated with PVB section, Orange section = PVB section, white section = Electrolyte well, Black line between white and orange = defect interface. Red arrow shows coating application direction*

2.7 FTIR

FTIR stands for Fourier Transform Infrared and is a type of infrared spectroscopy. An infrared spectrum is formed by the absorption of electromagnetic radiation at frequencies that correlate to the vibration of specific chemical bonds withing a molecule by passing a beam of infrared light though the sample[133]. As the infrared radiation is passed through the sample some radiation is absorbed by the sample (absorption) and some passes through it (Transmittance) [134].

Absorbance(A) is defined as the quantity of light that is absorbed while transmittance is the quantity of light that passes through a sample [135]. The resulting signal detected forms the infrared spectrum which represents what is called a molecular 'fingerprint' of the sample. The fingerprint formed is unique to the chemical structure analysed and thus forms the basis for FTIR analysis [134]. The spectrum formed is displayed with the wavenumber (cm^{-1}) on the x-axis and either the absorbance or % transmittance on the y-axis. As well as being able to detect the presence of specific functional groups the number of times the functional group occurs within a molecule can be detected by the FTIR this is known as the intensity and compares the relative presence of the functional group when compared to other detected groups [133]. The typical FTIR can detect signals in a range of 400 to 4000 cm^{-1} . Figures 2.3 and 2.4 show how the FTIR detects the signal formed when a sample absorbs some of the infrared radiation as well as how a sample is mounted against the crystal.

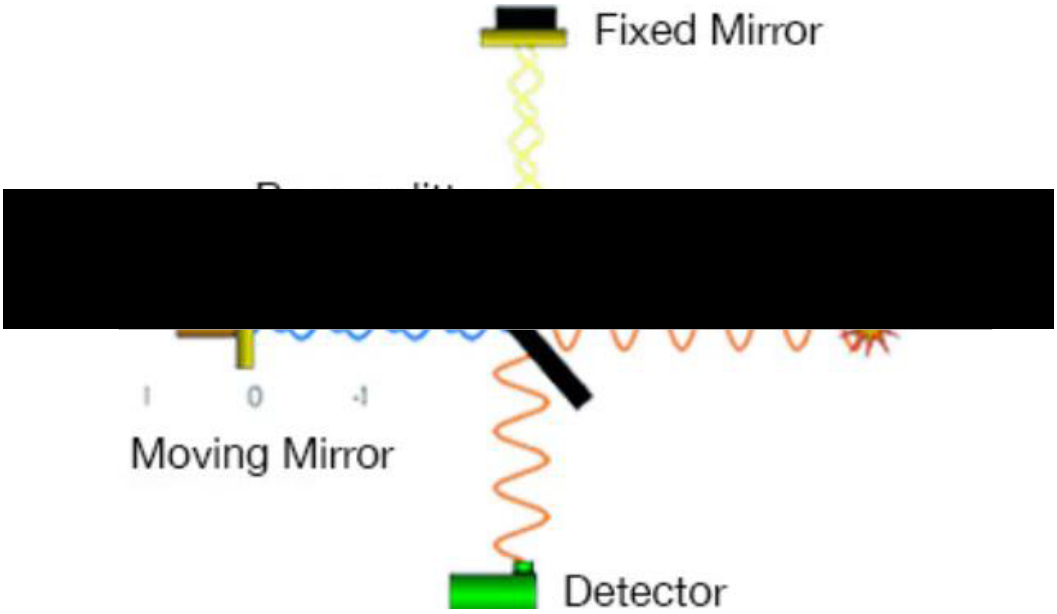

Figure 2.3 Schematic of how the signal is detected in an ATR-FTIR [134]

Figure 2.4 Schematic of how a sample is mounted over the crystal of an ATR-FTIR [134]

2.8 FTIR and cure varying delamination

Attenuated total reflectance Fourier transform infrared spectroscopy (ATR-FTIR) was carried out at a resolution of 4 cm^{-1}, 10 scans, for a wavelength range of 1000-4000 cm^{-1}. The FTIR was calibrated using Ethanol as the background reference scan. The scans were taken for a range of different cured samples of RAPTOR. RAPTOR was coated onto iron foil samples following the cleaning, mixing, application, and drying methods described in sections 2.3 and 2.4 to produce a uniform film thickness of 70µm. The absorbance scans produced were then compared to analyse the chemical structure changes for RAPTOR during the cure reaction.

2.9 Visual Sealed container delamination experiment

The delamination cell previously described was placed in a sealed container in a room maintained at 20°C reservoir of 0.86 $mol.dm^{-3}$ aqueous NaCl solution was used to maintain a humidity of 93% within the container to ensure the electrolyte well didn't dry. Then 0.86 $mol.dm^{-3}$ NaCl solution was then added to the electrolyte well using a pipette. Photographs were taken prior to placing the cell in the container and after 1 week.

Two slits were then made to the silicone sealant and tweezers were used to peel the tape back, allowing measure the delamination distance, as well as observe the substrate underneath the coating.

2.10 Scanning Kelvin Probe (SKP) Summary of key components

As discussed in sections 1.13 and 1.14 the SKP is an electrochemical technique that has been used previously to measure the kinetic rates for cathodic disbondment for a range of coatings on metal substrates by measuring the corrosion potential under organic coatings without the use of bulk electrolyte. The key components of the SKP tare shown in figures 2.5 and 2.6 .The main feature is the vibrating reference probe tip. It is made of a 125µm diameter gold wire that is housed within a tapered glass capillary tube with 5 mm of wire protruding out from the tapered end. The protruding wire acts as the reference tip while the reverse end of the capillary tube it attached to a 50 mm actuator (loudspeaker) that is connected to the vibrator drive that allows the tip to vibrate normal to the sample surface in a purely vertical direction .The vibration of the reference tip above the sample allows for measurements to be taken via generating a AC current in the external circuit which connects the sample and vibrating probe.

Additionally, the amplitude and frequency of this vibration is dependent on the characteristics of the waveform that drives the mechanical elements [136]. The actuator for the all the experiments carried out was driven at a frequency of 280 Hz. The tip and stage where the sample is connected are located inside a stainless-steel environment chamber while actuator is located outside the environment chamber to maintain effective electrostatic and magnetic shielding within the chamber. Additionally, both the tip and stage are held at earth potential. The lock-in-amplifier detects the ac voltage signal that is an amplified and converted form of the ac current that is generated by the vibrating tip.

The integrator receives the dc output from the lock-in amplifier and adjusts the dc bias applied to the sample via the transconductance amplifier which in turn automatically nulls the current. The magnitude of the reverse bias ($-E_{kp}$) applied via the integrator is measured and converted to a digital signal that is logged automatically by the computer. The signal equal to the local Volta potential difference between the reference probe and the sample surface. When the current is null the value of $-E_{kp}$ is equal to the local Volta potential difference that exists between the reference probe and sample surface (if the bias voltage is zero).The sample sizes are limited based on the space inside the environment chamber as well as the range of the stage. The typical size of samples used within this work are 50 x 50 mm .

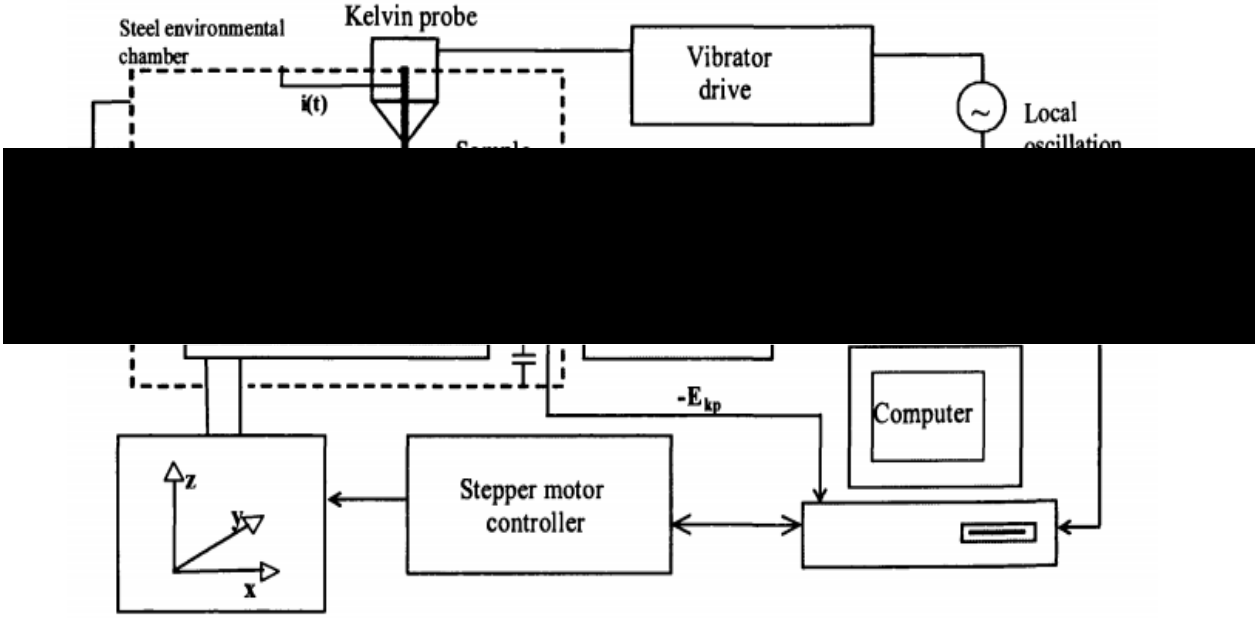

Figure 2.5 schematic of the SKP circuit setup [116]

The sample stage where is mobile and allows the position of the sample to change via three orthogonally arranged x,y,z stepper motor driven bearings. This allows for the sample to be moved during both calibration and positioning but more importantly provides the ability to scan across the sample surface. The vibration amplitude is in the range of +/-20 µm.

Figure 2.6 Experimental setup of the SKP apparatus

2.11 SKP calibration

The SKP potential can be calibrated in terms of electrode potential (vs. SHE) using Ag/Ag^{+}, $Cu/Cu2^{+}$, Fe/Fe^{2+} and Zn/Zn^{2+} redox couples according to an established calibration method [129]. The chosen metal is fabricated to form a disc with a well in the centre. The well is then filled with 0.5 $mol.dm^{-3}$ of the respective metal chloride(aq) or $CuSO_4$ in the case of copper was used .The Volta potential difference values or E_{kp} values are obtained for each system by positioning the SKP tip to a position of 100 µm above the solution in the well and logging the electrode potentials obtained.

Plotting the E_{corr} vs. SHE values obtained for each metal system in the order Zn/Zn^{2+}, Fe/Fe^{2+}, Cu/Cu^{2+} and Ag/Ag^{+} produces a linear plot that can be seen in figure 2.7 as the lower potential plot. When using the SKP to evaluate a system involving polymers the polymer layer must be considered. The Volta potential of polymer coated substrate is directly linked to the electrode potential of the substrate-polymer interface [27].

This is done by obtaining another calibration value by placing a free film of the polymer above but in contact with the aqueous salt. Then the salt solutions are left to equilibrate with the metal for three hours with the tip at a constant distance of 100µm from the polymer-air interface.

The equation for the half cell potential ($E_{1/2}$) of the metal solution interface for a bare metal surface covered with a layer of electrolyte solution is [27,137] :

$$E_{1/2} = \frac{\alpha_e^{ref}}{F} - \chi_{gas}^{sol} + \Delta\varphi_{sol}^{ref} \qquad \text{(Eqn 2.1)}$$

Where α_e^{ref} is the electronic work function of the reference probe material, F is faraday constant, χ_{gas}^{sol} is the dipole potential of the solution – gas interface, and $\Delta\varphi_{sol}^{ref}$ is the measured Volta potential difference between the reference probe and the solution surface.

For a polymer coated metal substrate, the equation is :

$$E_{1/2} = \frac{\alpha_e^{ref}}{F} - \chi_{gas}^{pol} + \Delta\varphi_{pol}^{ref} \qquad \text{(Eqn 2.2)}$$

χ_{gas}^{pol} is the dipole potential of the polymer- gas interface and $\Delta\varphi_{pol}^{ref}$ is the Volta potential difference measure between the reference probe and the polymer surface.

When delamination has occurred a layer of electrolyte exists between the substrate metal and polymer layer which transforms equation 2.2 to [137] :

$$E_{1/2} = \Delta\varphi_D + \frac{\alpha_e^{ref}}{F} - \chi_{gas}^{pol} + \Delta\varphi_{pol}^{ref} \qquad \text{(Eqn 2.3)}$$

Where $\Delta\varphi_D$ is the Donnan potential equivalent to the Galvani potential difference established between the polymer layer and the electrolyte solution ($\varphi^{sol} - \varphi^{pol}$).

If the gas -phase composition does not change: α_e^{ref} , χ_{gas}^{pol}, and χ_{gas}^{sol} in equations 2.1-2.3 are all expected to remain constant over time.

The free corrosion potential (E_{Corr}) of the metal substrate surface is usually expressed vs. a reference electrode by the following equation :

$$E_{Corr} = E_{1/2} + E_{1/2}^{ref} \quad \text{(Eqn 2.4)}$$

Where $E_{1/2}$ is the half-cell potentials defined in equations 2.2 and 2.3 and $E_{1/2}^{ref}$ is the half-cell potential of the reference electrode. Based on the values , α_e^{ref} , χ_{gas}^{pol}, and χ_{gas}^{sol} remaining constant equation 2.4 may be re-written as the following equations:

(Bare substrate -solution)

$$E_{Corr} = A + \Delta\varphi_{sol}^{ref} \quad \text{(Eqn 2.5)}$$

(Substrate-intact polymer interface) or (Substrate- delaminated polymer interface)

$$E_{Corr} = B + \Delta\varphi_{pol}^{ref} \quad \text{(Eqn 2.6)}$$

Where A and B are constants for the substrate- solution and substrate- polymer systems respectively. The value of A can be determined by simultaneous measurements of E_{Corr} (vs. a standard reference electrode) and $\Delta\varphi_{sol}^{ref}$ using the Kelvin Probe. The value of B is calculated using the SKP to measure E_{Corr} and $\Delta\varphi_{pol}^{ref}$, α_e^{ref} , χ_{gas}^{pol}, and χ_{gas}^{sol} simultaneously.

An example plot for the calibration of PVB can be seen in figure 2.5 represented by the higher potential line. The higher line on figure 2.7 is $\Delta\varphi_{pol}^{ref}$ vs. E_{corr} for the metal-solution-polymer-air system and the lower line is $\Delta\varphi_{sol}^{ref}$ vs. E_{corr} for the metal-solution-air system. By examining both lines, the gradients both equate to 1 and the intercepts of the higher line is 0.555 and 0.330V for the metal air data sets. The difference of 0.225V is attributed to the difference between the dipole potentials χ_{gas}^{pol}, and χ_{gas}^{sol} .

To use the data produced by the SKP in the following cathodic disbondment experiments the data must be calibrated. The calibration of the SKP was done using the Cu/Cu^{2+} redox couple. The E_{corr} value for copper is known to be 298mV and is assumed to be a constant. However, the value of the Cu/Cu2+ couple is liable to change over time and is used to calculate the calibration value that is subsequently added to each data point recorded by the SKP. So once the SKP records a value for $\Delta\varphi_{sol}^{ref}$ it is inserted into equation 2.7 to calculate a value for the constant.

$$\text{Ecorr} = \Delta\varphi_{sol}^{ref} + \text{Constant} \quad \text{(Eqn 2.7)}$$

A polymer layer exists between the tip and the sample and this must be considered in order to calculate an accurate value for the under-film potential (E_{KP}). This is done by subtracting the difference between the dipole potentials ($\chi_{gas}^{pol} - \chi_{gas}^{sol}$) seen by Eqn 2.8 For PVB this value is 0.225V.

$$\text{Calibration factor} = \text{Constant} - (\chi_{gas}^{pol} - \chi_{gas}^{sol}) \quad \text{(Eqn 2.8)}$$

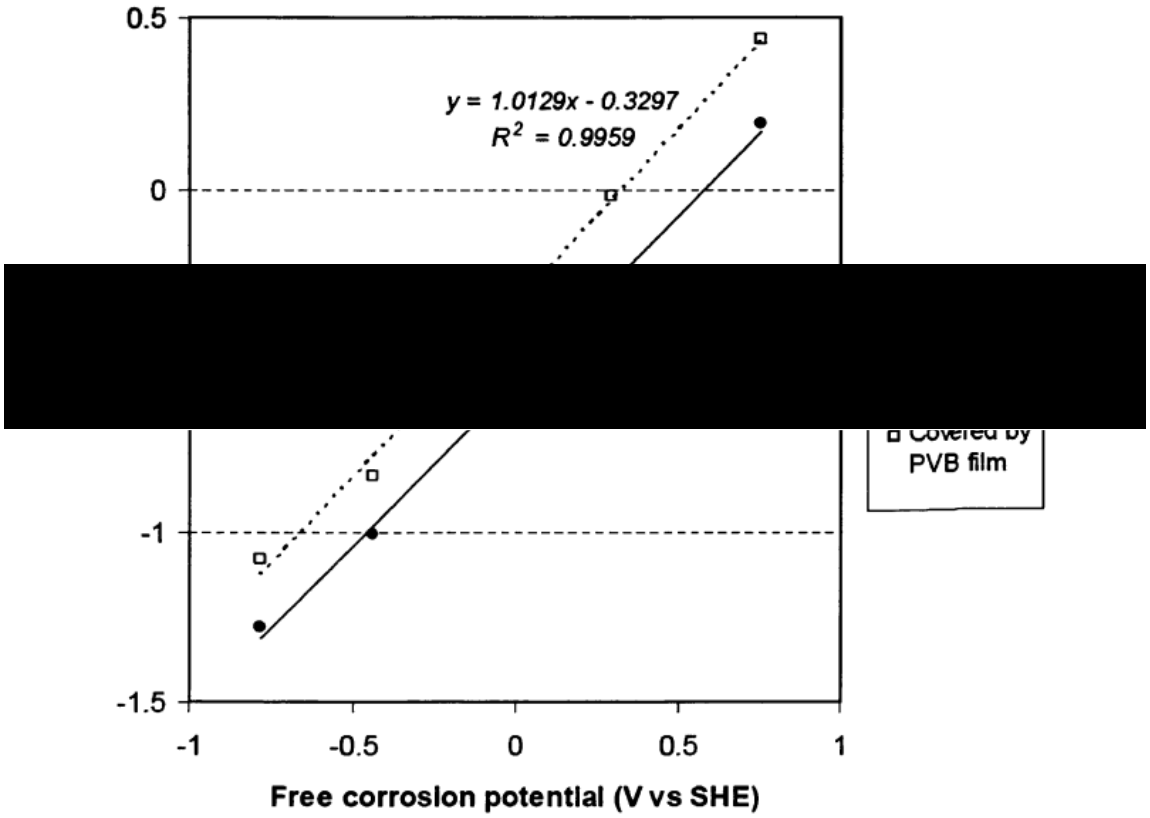

Figure 2.7 E_{KP} VS. Free corrosion potential for different metal redox couples [116]

The final calibration value is then added to every individual data point recorded for that specific experiment. Moreover, it is important to note that this difference in dipole potentials is different for different polymers and the calibration process must be repeated for standalone systems and every experiment. However, for the delamination cells used in this study for the SKP the polyurethane coatings are overcoated with PVB which in turn allows for the 0.225V value to be used in equations 2.7 and 2.8 as this value only considers the air to polymer dipole.

2.12 SKP experimental setup and scan settings

The SKP tip was firstly cleaned using a 2 mol.dm^{-3} (aq) of HCL before rinsing with deionised water was applied. Following calibration, the delamination cell is placed in the SKP chamber so that the tip is 100µm above the polymer surface and the sample is level to provide a constant distance between the tip and sample throughout the scan. The scans involved for the following experiments involved scanning four lines across the surface of the sample up to a maximum scan length of 20 mm from the artificial defect. Each scan line is formed of 400 individual data points (for the 20mm scan) to maintain a constant resolution which means if the scan length increased so will the number of points. Each line was 1mm apart. Each scan was taken in intervals of 60 minutes apart up to a total scan time of 8640 minutes for the following experiments. The relative humidity was maintained at approximately at 96 % RH using a reservoir of 0.86 mol.dm^{-3} (aq) NaCl solution. The same solution was also added to the delamination cell well to initiate cathodic disbondment. The measured potentials are then automatically logged to the computer so that the data can be processed to evaluate the under-film potential under the coating over time. Figure 2.8 shows a schematic of the scan area of a delamination cell.

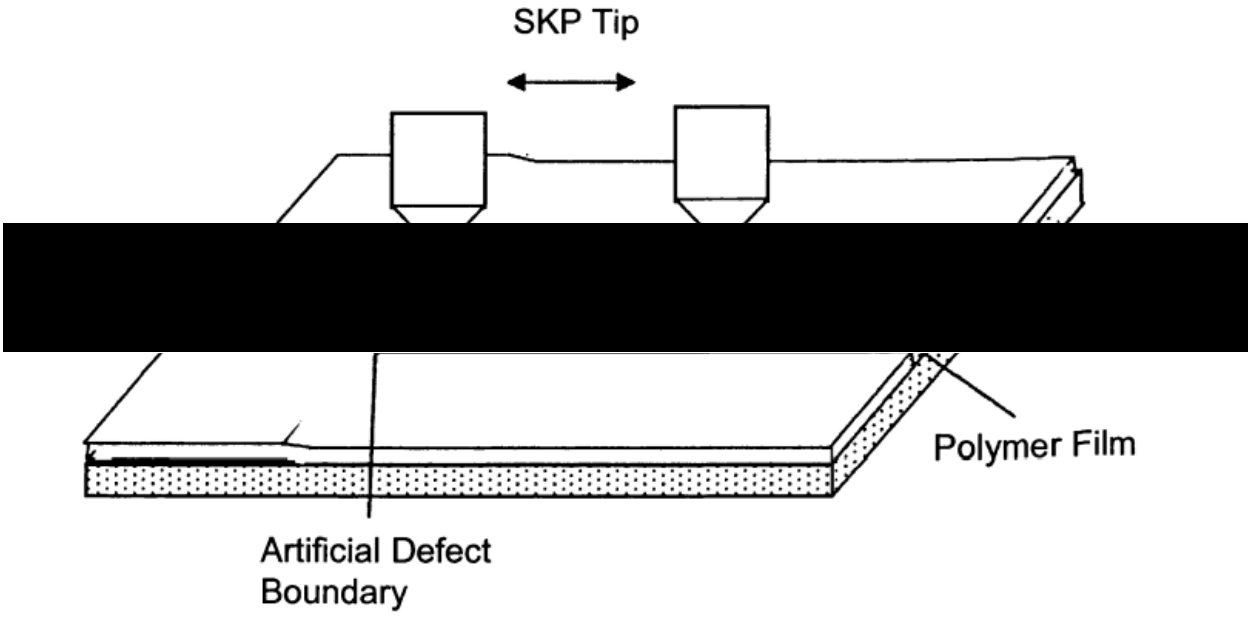

Figure 2.8 schematic of the scan area of a delamination cell. For the experiments conducted in this study the SKP tip will scan from the PVB interface not the defect.[116]

2.13 Measuring delamination of coatings

After the experiments described in sections 2.9 and 2.12 had been conducted the coating delamination distance is measured from the PVB/polyurethane interface. Four separate measurements are taken per sample . Figure 2.9 show where the measurements are taken from and to.

Figure 2.9 a delamination cell described in section 2.6 Where the red line is the PVB/RAPTOR interface, the white surrounding the defect is the silicon sealant *and the 'x' are the points where the measurements are taken from.*

2.14 Filiform corrosion (FFC) experiment

The iron foil samples in the following filiform corrosion experiments are identical in dimension , composition and cleaning method of the samples previously described. Following cleaning two strips of PVC tape were placed parallel to each other on either side of the coupon leaving a uniform exposed strip of iron in the centre (3x5cm).The samples were then coated with either RAPTOR-7 ALP, GF or a 15.5% w/w ethanolic solution of polyvinyl butyral (PVB), using the same method outlined in section 2.4. Once dry, two 1.5cm long defects were introduced to the coating using a scalpel to form two parallel penetrative scribes into the coating spaced at 2.5cm apart exposing the substrate underneath.

The PVB coated samples were briefly annealed by applying heat from a hairdryer to the coating for a period of 5 seconds to remove any residual stress from the coating prior to forming the slit. This is done to limit the chance of mechanical delamination occurring to the PVB film while introducing the defects.

Then using a micro syringe 2 µl of 0.005 mol.dm^{-3} $FeCl_2$ solution was added to each scribe defect to initiate filiform corrosion. The samples were placed in a sealed container which contained a well of saturated sodium sulphate deca-hydrate ($Na_2SO_4 . 10H_2O$) which maintains a relative humidity of 94 % at 20 ^{0}C [138]. The samples were photographed at one-week intervals starting at week 0 to allow for measurements to be taken of the filiform filaments formed. The PVB coated samples were initiated at the same time for each batch of filiform cells and placed in the same conditions to act as a reference as the occurrence of filiform corrosion on iron substrates coated with PVB has previously been shown [114].

2.15 Filiform corrosion filament data analysis

Once the filiform corrosion cells are prepared and initiated following the procedure outlined in section 2.14 the cells are photographed in 1-week intervals starting at week 0. The cells are photographed with a reference to a known distance next to the cell which was inputted Image j for image analysis of the filiform filaments formed. The individual lengths, widths, and corroded area of each filament formed during FFC were measured each week to track the kinetics of the filament growth. The surface area of the FFC attack was measured by calculating the area occupied by corrosive discoloration of the surface. Once the data was collated the rates were plotted against time. A total of 4 defects were used for each coating and the confidence limits (errors) between the data correspond to ± one standard deviation of the mean data . Figure 2.10 show the designation of each measured variable.

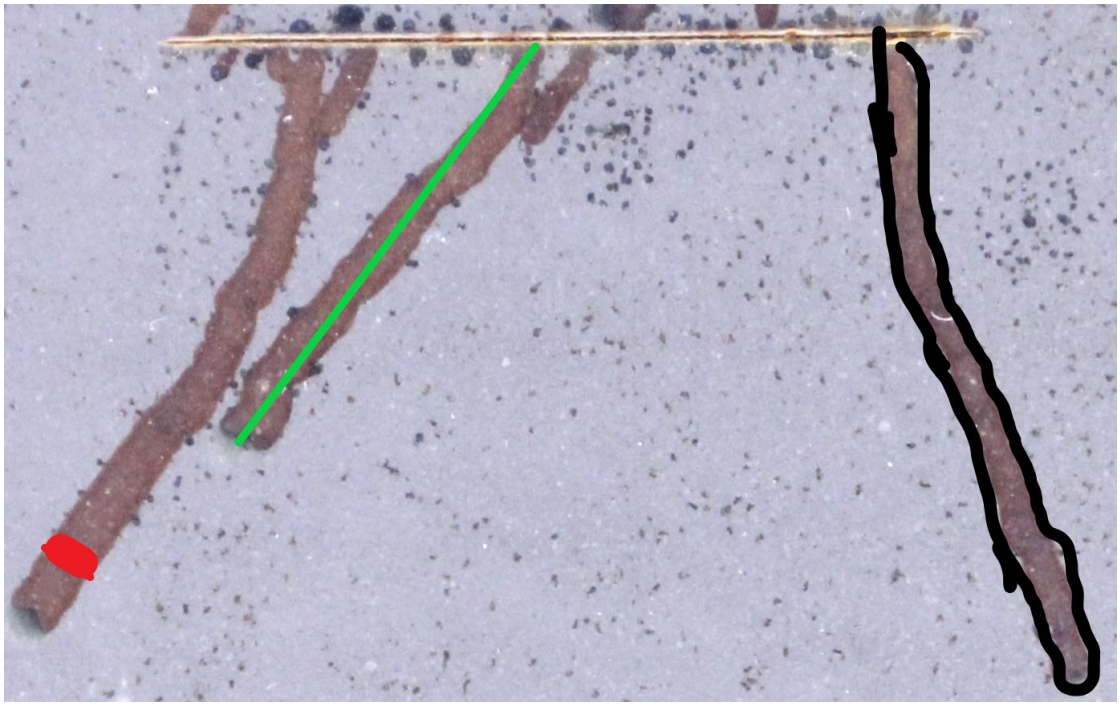

Figure 2.10 Filament measurement distinction for image analysis. The red line represents the filament width, the green line is the length and the area inside the black outline of the filament is the filament area

Chapter 3 Results and Discussion

3.1 FTIR Characterization of RAPTOR

RAPTOR was coated onto an iron foil sample and cured following the methodology in section 2.4. The sample was scanned at varying times during the curing process at 1 day, 3 days, and 5 days. Once cured, for the desired time the FTIR absorbance scans were carried out with a resolution of 4cm^{-1} for 10 scans over the sample with Ethanol was used as a reference for the background scan. The absorbance scans for the varying cures of RAPTOR can be seen below in figure 3.1 .The wavelength (cm^{-1}) is on the x-axis and the relative intensity is plotted on the y-axis as an arbitrary value. Table 3.1 summarises the various peaks detected in figures 3.1 with their associated wavelength, relative intensity, and associated functional group. The intensity compares the relative presence of a functional group when compared to other detected groups.

Table 3.1 showing peaks detected by the FTIR scans of RAPTOR over various cure times

cure time	frequency/cm^{-1}	relative strength	assignment
1 day	1703	very strong	γ(C=O) bonded
1 day	3300–3340	medium	γ(N–H) bonded
3 day	1703	very strong	γ(C=O) bonded
3 day	3300–3340	medium	γ(N–H) bonded
5 day	1703	very strong	γ(C=O) bonded
5 day	3300–3340	strong	γ(N–H) bonded

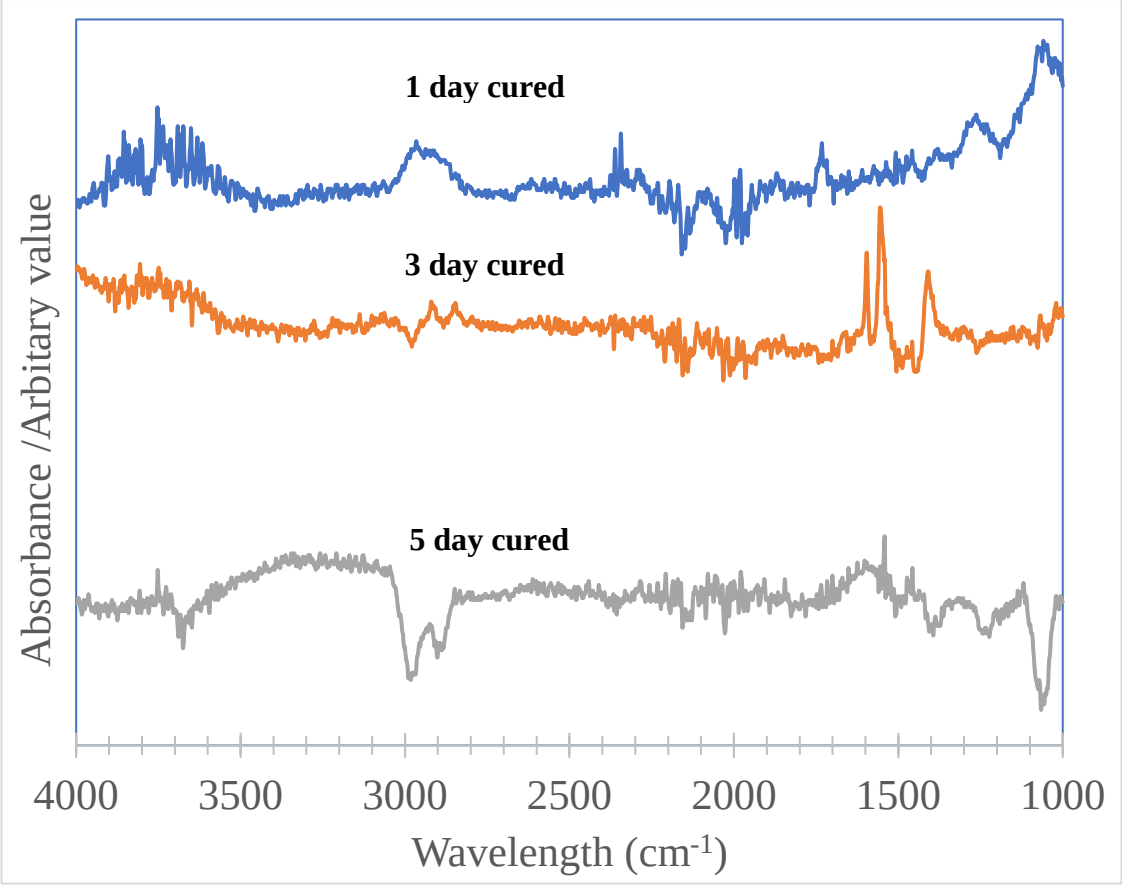

Figure 3.1 FTIR absorbance scans of RAPTOR after various cure times

Figure 3.1 shows that as the curing time increased the hydroxy peak at 3300 cm^{-1} decreases in relative intensity [139]. In contrast, the urethane carbonyl at 1703 cm^{-1} and NH stretching at 3300-3340 cm^{-1} increased in intensity. The greatest observed change can be seen for the NH stretching which increased from 'medium' detected intensity at the 1 day cured sample to 'strong' for the 5-day cured cell [139]. The changes in relative intensity of the detected functional groups corresponds to another study that evaluated the cure of a 2-part polyurethane coating where the increase in the urethane carbonyl and NH stretching and the decrease in the detected hydroxy groups is attributed to the formation carbamate (urethane) linkages in the polymer structure [139].

3.2 Cathodic delamination of unpigmented coatings

3.2.1 The effect of cure time on cathodic delamination – Visual Results

The cathodic delamination of a variety of RAPTOR coatings was monitored visually to allow for a quick and efficient method of screening for the optimum coating cure. Following the FTIR characterization of the cured RAPTOR coatings, delamination cells were formed following the methodology described in section 2.6 which is an adaptation of the classic Stratmann cell [132]. The cells formed were placed within a sealed plastic container kept at a humidity of 96 % RH using a well of 0.86 $mol.dm^{-3}$ (aq) NaCl. Corrosion driven cathodic delamination was initiated using 0.86 $mol.dm^{-3}$ (aq) NaCl added to the well. Most delamination cells were left for 4 days. The apparent superior protection afforded by RAPTOR-7 meant that these samples were left for 7 days. After the experiment the coating was peeled back to remove the delaminated sections of the coating.

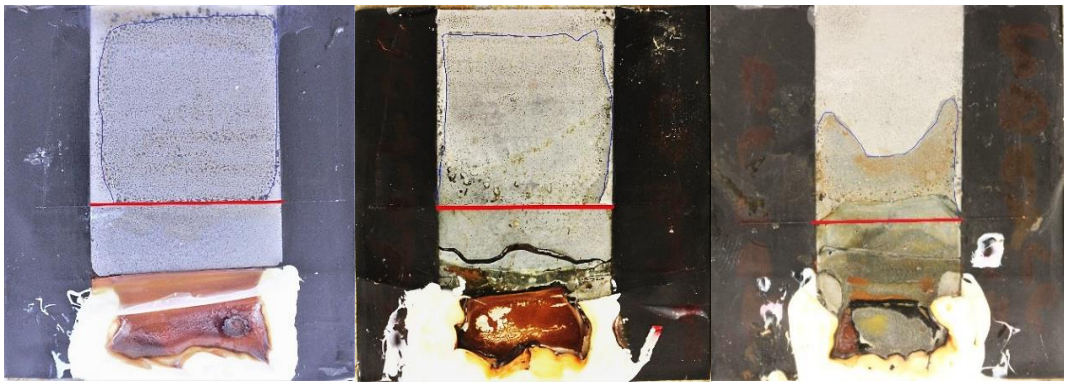

Figure 3.3 Images of stratmann cells coated in. 1 day (left), 3 day (middle), and 5 day (right) following delamination for 4 days

Figure 3.3 show images of the samples after the experiment where the red horizontal line indicates the position of the PVB/RAPTOR interface and the thin blue line highlights the boundary between the exposed substrate and the intact coating. Four measurements of the delamination distance (x_{del}) were taken along PVB/interface following the methodology in section 2.11 for each cell. Table 3.2 summarises the data where the mean signifies the average x_{del} value across the 2 delamination cells for each cure and SD is the standard deviation taken for that cure across the 8 measurements .

Table 3.2 Summary of delamination distance for varied cures of RAPTOR recorded 4 days after initiation of delamination using 0.86 mol.dm^{-3} NaCl

Cure (days)	X del (mm)								mean	SD
	1	2	3	4	5	6	7	8		
1	27.5	27.9	26.8	28	26.8	27	27.6	26.8	27.3	0.5
3	24.5	26.5	23.7	24.2	23.8	26.2	24.2	24.5	24.7	1.0
5	13	12	26	22	12.4	23	24	14	18.3	5.6
7	12.1	11.4	9.8	10.2	9.7	12	10.3	11.6	10.90	0.9

Table 3.2 shows that as the cure time increases the mean x_{del} distance decreases, with the mean x_{del} being 10.9 ± 0.9 mm for RAPTOR-7 and 27.3 ± 0.5 mm for RAPTOR-1 . The finding that coatings which had been cured for longer periods of times provided superior resistance to cathodic delamination is consistent with the FTIR characterization (section 3.1). It is believed that the change in functional groups over time (from hydroxy and isocyanate functional groups to the formation of carbamate groups) suggest that as the cure reaction proceeds the susceptibility of the coating/iron interface to alkaline hydrolysis decreases which was supported by the delamination data.

Following the experiment, all RAPTOR and pigmented variants would be cured for 7 days. The cure time was chosen to ensure that the coating delamination occurred at a rate that allowed for study into the kinetics of delamination without the need for constant inspection.

3.2.2 SKP Results

The Scanning Kelvin probe was used to monitor changes in underfilm E_{corr} during the delamination of RAPTOR-7 from iron. Scans were completed at intervals of 60 minutes for up to 7 days following initiation. Figure 3.5 shows the time dependant $E_{corr}(x)$ profiles for RAPTOR developed following initiation of coating delamination, where the x-axis shows the distance from the PVB/RAPTOR interface where zero is at the interface. The time dependent E_{corr} profiles formed develop due to ionic current flux passing along a thin layer of electrolyte that ingresses beneath the delaminated coating. This ingress of electrolyte produces an ohmic potential gradient that links the anodic site (at the artificial defect) where iron dissolution occurs (equation 1.6) to the cathodic oxygen reduction site (equation 1.8) which is present at the coating delamination front [140,142].

The potential at the defect is assumed to be at a potential of -0.44 V which is the free corrosion potential of iron [2]. This assumption is likely as other literature has shown it to be true for E_{corr} profiles generated by the SKP for PVB Coated iron delamination cells [118].

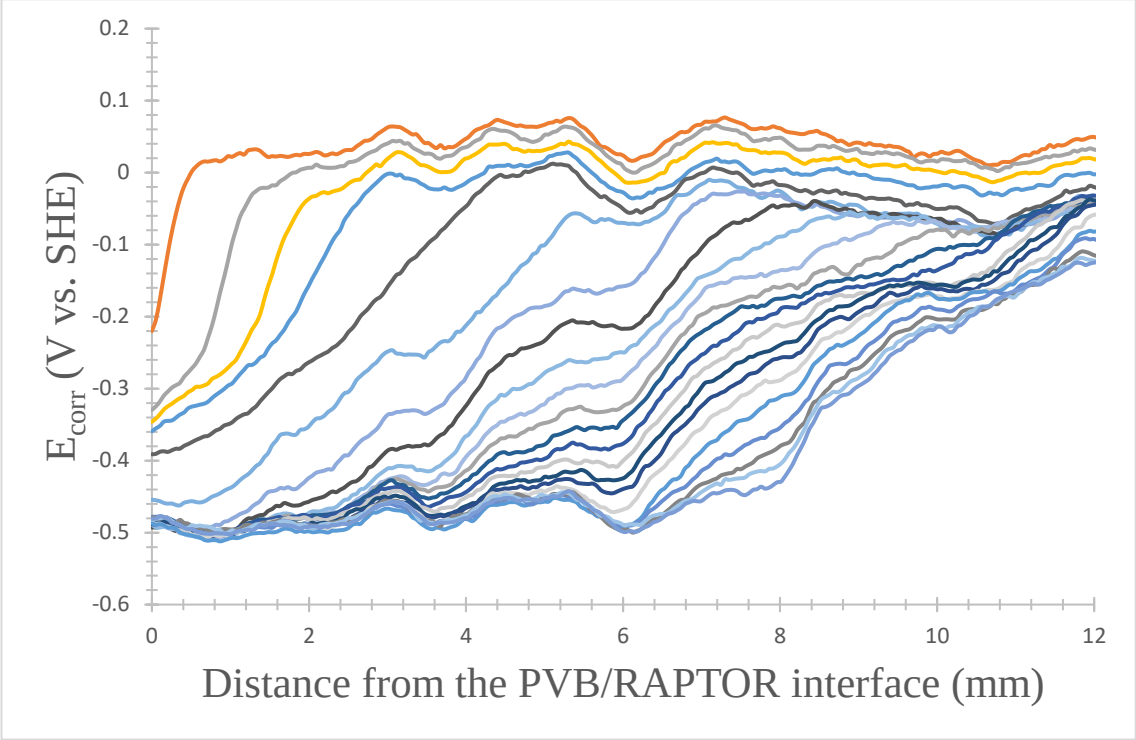

Figure 3.5 SKP derived Ecorr as a function of distance from the PVB/RAPTOR interface profiles for the delamination of RAPTOR-7 overcoated with PVB from iron initiated with 0.86 $mol.dm^{-3}$ NaCl electrolyte. Profiles from left to right at times of 360,420,480,540, and then in intervals of 8 hours. ti= 330 minutes

The high, constant potential (~0.05 V vs. SHE) seen on the right-hand side of the plots In figure 3.5 represent the E_{intact} potential for the intact non-delaminated section of the coating. The sharp inflection points observed to be travelling from left to right in Figure 3.5 correspond to the position of the delamination front as described in section 1.28.1 It is the sharp inflection point that have been identified as a semi empirical means of spatially and temporally identifying the position of the delamination front in an E_{corr} (x) profile [142,143].

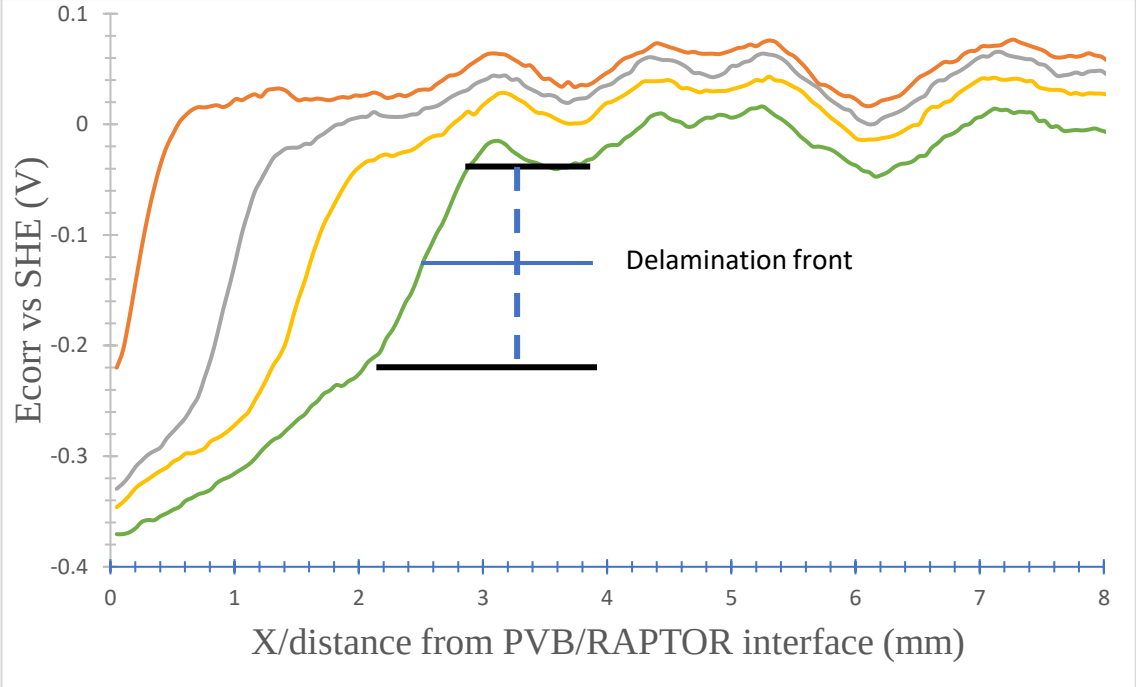

Figure 2- Simplified SKP derived Ecorr as a function of distance from the PVB/RAPTOR interface profiles to demonstatre where the delamination front distance measurements are taken from .

Figure 3.6 shows a simplified plot of 3.5 with only 4 profiles to help illustrate where the delamination front of an individual profile is taken as. For example, for fourth profile the delamination front distance is taken as the corresponding x value of the midpoint between the maximum and minimum points of the sharp inflection point in the graph seen by the black solid lines on figure 3.6. Therefore, for that profile the delamination front is taken as 2.5mm.

The rate kinetics of the delamination process are characterised by plotting the delamination front distance (x_{del}) against $(t_{del} - t_i)^{1/2}$. Which relates to equation 1.34 where k_d is the rate constant of delamination, t_{del} is the time associated with the specific delamination front distance and t_i is the time at which delamination is first detected.

$$x_{\text{del}} = k_d(t_{del} - t_i)^{1/2} \qquad \text{(Eqn 1.34)}$$

The rate of cathodic delamination is regarded as a multistep process and can be limited by several processes that include oxygen reduction, oxygen diffusion, cation migration or anodic dissolution. For uninhibited coating systems the rate of oxygen diffusion and oxygen reduction are fast. Therefore, rate kinetics of coating delamination for these systems are then typically parabolic (scale with $t^{1/2}$).

Parabolic kinetics have been shown to occur for uninhibited PVB coatings and have been attributed to the rate limited by the mobility of cations (here Na^+ cations) within the underfilm electrolyte between the defect and delamination front [142,143].

Figure 3.7 shows the plot of (x_{del}) against $(t_{del} - t_i)^{1/2}$ for the three repeat RAPTOR-7 delamination cells where the orange line is derived from the E_{corr} profiles in figure 3.5. The linear trends observed between x_{del} and $(t_{del} - t_i)^{1/2}$ in figure 3.7 are consistent with parabolic kinetics. The k_d constant from the three repeat experiments of RAPTOR-7 were averaged to yield a k_d value for RAPTOR of 96.59 ± 13.62 µm/min$^{-1/2}$ which corresponds within one standard deviation of the visual k_d values calculated for RAPTOR-7 from section 3.2.1.The loss of disbondment is believed to occur as a result of the reaction between the alkaline electrolyte and polymer or polymer/substrate interface. This is a likely mechanism for Polyurethane coatings, which have previously been shown to be susceptible to alkaline hydrolysis [98].However, as previously stated in section 1.6 free radical intermediated produced during the cathodic reaction or physical displacement of the coating via the formation of the alkaline electrolyte could play a part [116,117,120,122,125].

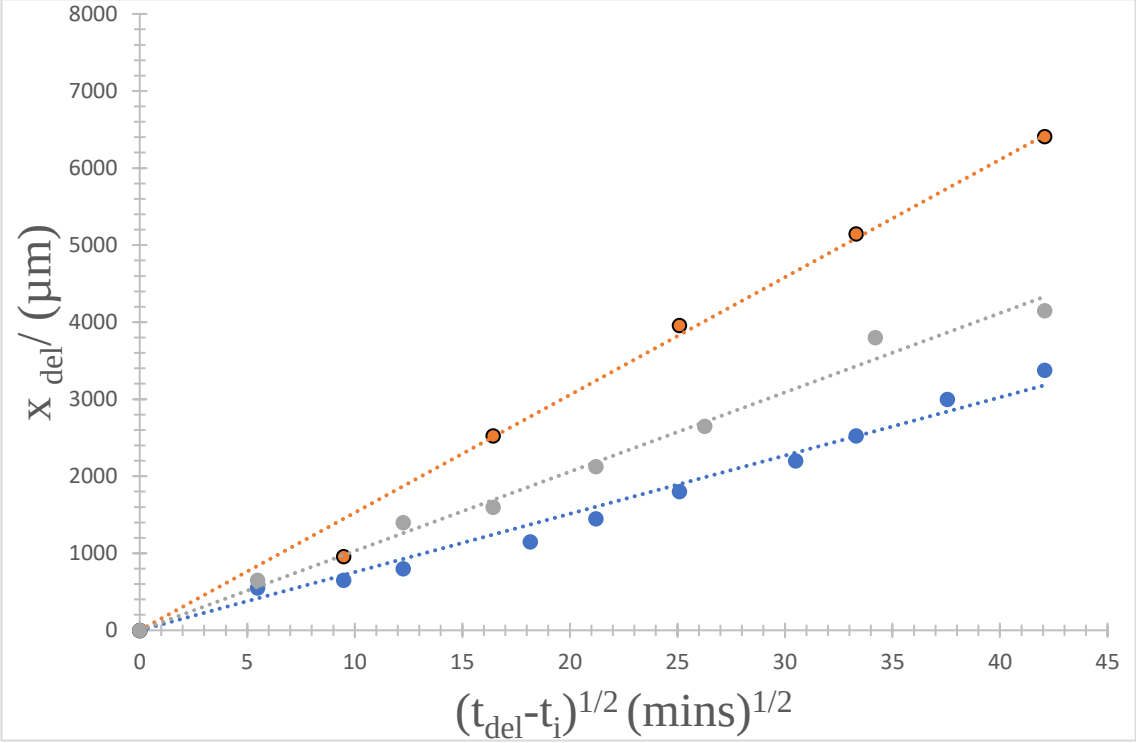

Figure 3.7 Plots of x_{del} vs. $(t_{del}-t_i)^{1/2}$ for RAPTOR-7 derived from the experimental data .

3.3 Cathodic delamination of pigmented coatings

3.3.1 Visual delamination of pigmented RAPTOR

RAPTOR formulated with 5 wt.% aluminium polyphosphate (AL P) or Glass flake (GF) pigments were applied to iron substrates, and cathodic delamination was initiated following the experimental procedure outlined in sections 2.6 . The visual delamination method was used to screen the pigments in a quick and efficient method. The coatings were all cured for 7 days and corrosion was initiated using 0.86 $mol.dm^{-3}$ (aq) NaCl solution and left for 7 days at a humidity of 96%. Table 3.3 shows a summary of the x_{del} measurements taken following the same method outlined in section 3.2.1. The presence of ALP resulted in a 33.18% reduction in x_{del} compared to RAPTOR-7 . While an increase in the total delamination length was observed in the case of GF.

Table 3.3 Summary of delamination lengths for RAPTOR and pigmented variants recorded 7 days after initiation of cathodic delamination using 0.86 $mol.dm^{-3}$ NaCl

Coating	Average X del (mm)				mean	SD
	1	2	3	4		
RAPTOR-7	12.1	11.4	10.6	10.2	11.1	0.7
AL P	8.0	8.6	7.0	6.0	7.4	1.0
GF	20.0	16.0	15.0	18.0	17.3	1.9

3.3.2 SKP Results

SKP was used to gather further insight into the delamination kinetics for coatings which contained ALP. Figure 3.8 shows the SKP derived E_{corr} time dependant profiles established once delamination was initiated at the PVB-ALP interface. E_{intact} remains constant at a value of 0.05 V vs. SHE up to 7mm from the PVB-ALP interface and then shifts up to 1.0V for the remainder of the scan. As the potential in the two regions remain constant it is assumed that the shift in potential is a result of a change in the coating profile. Following the same procedure in section 3.2.1 the kinetics for ALP are characterised using equation 1.34. The delamination front distances obtained from figure 3.8 are plotted against $(t_{del} - t_i)^{1/2}$ to observe the rate kinetics of delamination shown in figure 3.9. Figure 3.9 demonstrates the existence of a parabolic relationship between the x_{del} and $(t_{del}-t_i)^{1/2}$ for ALP. This is indicative of delamination being limited by the mass transport of Na^+ ions to the cathodic site which was seen in section 3.2.2. This is confirmed by the linear relationship seen in figure 3.9.

The delamination rate constant for AL P is taken as 61.18 $\pm$ 8.63 µm/min$^{-1/2}$ ·. The standard deviation is calculated by taking the fractional percentage error for RAPTOR-7 and applying it to ALP.The delamination corresponds to a 36% decrease in the delamination rate constant for RAPTOR-7. This corresponds within one standard deviation of the delamination rate constant calculated from the delamination data in section 3.3.1.

As seen in figure 3.9 as a linear relationship exists between x_{del} and (t_{del}-t_i)$^{1/2}$ .This is indicative that the rate determining step remains the mass transport of the Na^+ cations to the cathodic site at the delamination front. Therefore, due to the reduction in k_d it can be said that the addition of ALP must reduce the mass transport of Na^+ cations or the hydroxyl or intermediate free radical production at the cathodic site. But only to an extent where the oxygen diffusion is not the rate determining step which would have been seen by linear kinetics.

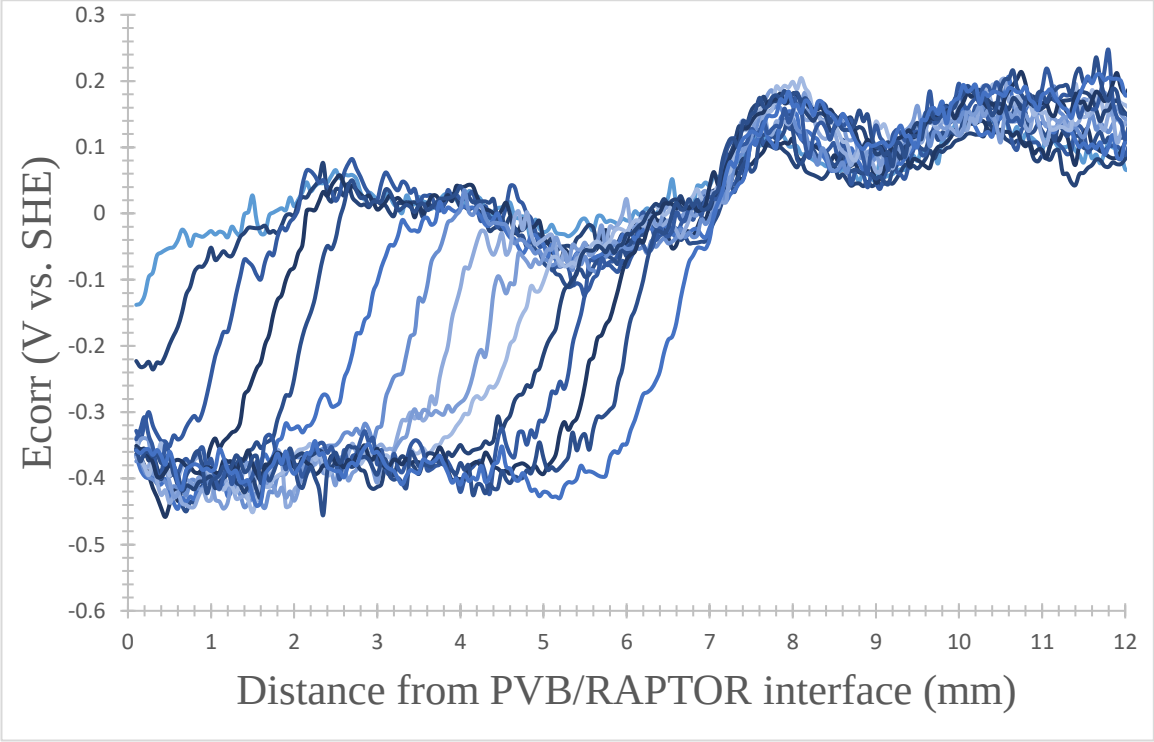

Figure 3.8 SKP derived Ecorr profiles as a function of distance from the PVB/AL P interface for the delamination of AL P overcoated with PVB from iron initiated with 0.86 mol.dm^{-3} NaCl electrolyte. Profiles from left to right at times of 240,360 and then in intervals of 12 hours up to 9720 minutes. ti= 210 minutes

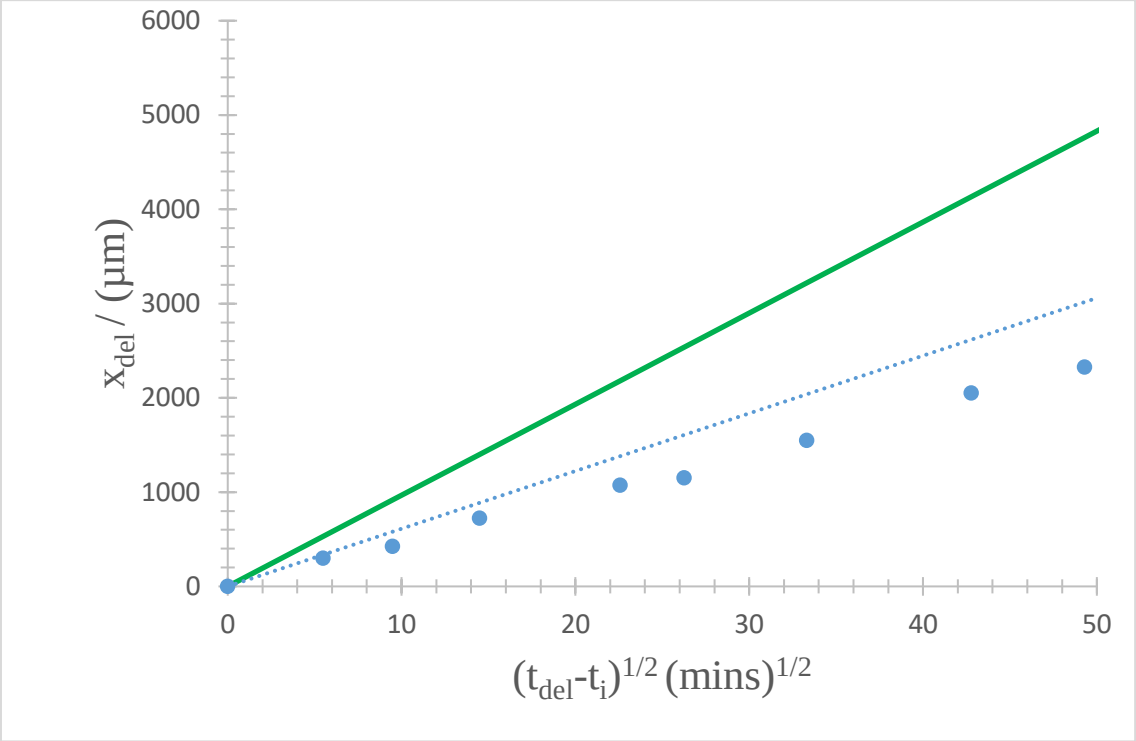

Figure 3.9 Plot of x_{del} vs. $(t_{del}-t_i)^{1/2}$ for ALP (Blue) derived from figure 3.8 against the averaged plot for RAPTOR-7 (green)

3.3.3 rate reduction mechanism of aluminium polyphosphate

As previously discussed, as cathodic disbondment progresses electrolyte ingresses under the coating. From solubility data obtained from the literature it is feasible to predict that aluminium polyphosphate pigments within the coating can dissociate into the electrolyte as the pigment solubility increases as the pH value increases above a value of 8 which corresponds to the second ionisation pKa of phosphoric acid (7.2) [65]. Therefore, as pH's under the organic coating at the delamination front can reach values near pH's of 12 the following reactions are feasible:

$$AlH_2P_3O_{10} \rightarrow Al^{3+} + 2H^+ + P_3O_{10}^{5-} \quad \text{(Eqn 3.1)}$$

$$Fe^{2+} + Fe^{3+} + P_3O_{10}^{5-} \rightarrow Fe_2P_3O_{10} \quad \text{(Eqn 3.2)}$$

$$P_3O_{10}^{5-} + 2H_2O \rightarrow 3PO_4^{3-} + 4H^+ \quad \text{(Eqn 3.3)}$$

$$x(Fe^{2+}, Fe^{3+}) + \gamma PO_4^{3-} \rightarrow Fe_x(PO_4)\gamma \quad \text{(Eqn 3.4)}$$

Equations 3.1 and 3.4 show that sparingly soluble secondary iron phosphates and insoluble tertiary phosphates can form under the degraded polyurethane coating. The precipitates that form could inhibit both the diffusion of aggressive electroactive species (Na^+ cations) and the electrolyte itself as well as reducing the area of the cathodic site [64,65,82,96]. Additionally, it has been shown that aluminium tripolyphosphate can hydrolyse to produce H^+ ions as seen in equation 3.3 which could minimise the hydroxyl production during the oxygen reduction reaction at the delamination front. This reduction in hydroxyl production would reduce the pH under the coating and thus limit the alkaline attack of the polymer itself. Moreover, the reduction in pH would reduce the electrolytes ability to creep and physically displace the coating [96,125]. However, the presence of aluminium polyphosphate would not reduce the production of free radical intermediates that form during the cathodic reaction which have been shown to be more destructive to organic coatings than alkaline hydrolysis [116].

3.4 FFC

3.4.1 Visual comparison of filaments

RAPTOR-7, AL P and GF were used to coat iron following the methodology outlined in section 2.12. The final coating thickness in each case was 70 µm , as measured using Vernier callipers. A 30 µm thick PVB coating was also applied to iron to act as a control coating. PVB was chosen as PVB coated iron has previously been shown to be susceptible to FFC [113,143]. All coatings were cured for 7 days prior to initiation, apart from PVB which was cured for 24 hours. Two samples were prepared for each of the four coatings. Two 1.5 cm long scribe coating defects were made on each sample and 2 µl of $5x10^{-3}$ $mol.dm^{-3}$ (aq) solution of $FeCl_2$ was used to initiate FFC per scribe [114]. Samples were kept in a sealed plastic container maintained at a relative humidity of 94 % using saturated Na_2SO_4 . $10H_2O$. Photographs of the samples were taken at intervals of 1 week and are shown in Figures 3.10-3.13 .The length, width, number of filaments per scribe and FFC area were measured using visual analytical software (Image J) following the methodology outlined in section 2.13. Variations in the filaments between scribes is attributed to minor variations in the initiation process such as : volume of initiate solution, spread of electrolyte across a scribe as well as the scribe formation. Additionally, variations in the coating thickness and polymer structure could impact the formation of filaments between scribes.

RAPTOR-7

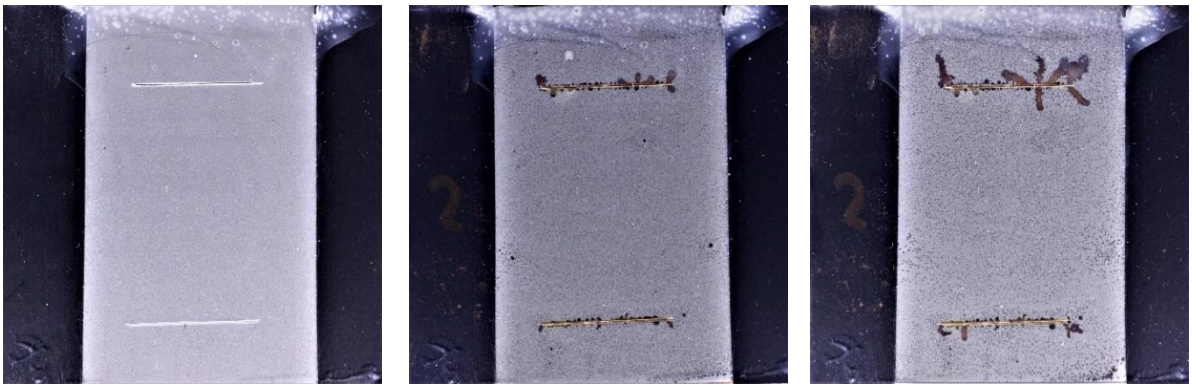

Week 0 Week 1 Week 2

Week 3 Week 4

Figure 3.10 Photographs of RAPTOR-7 in 1-week intervals up to four weeks after initiated with 2µL of 0.005[3] $mol.dm^{-3}$ $FeCl_2$ per scribe

PVB

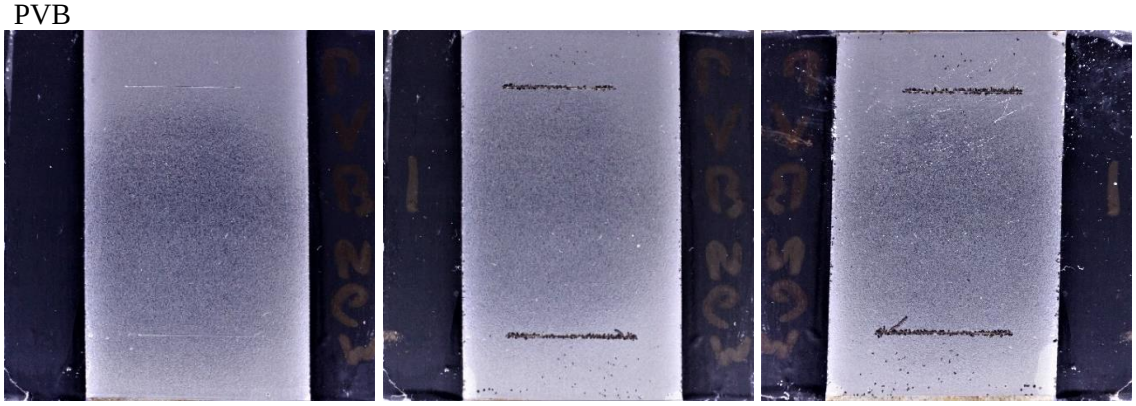

Week 0 Week 1 Week 2

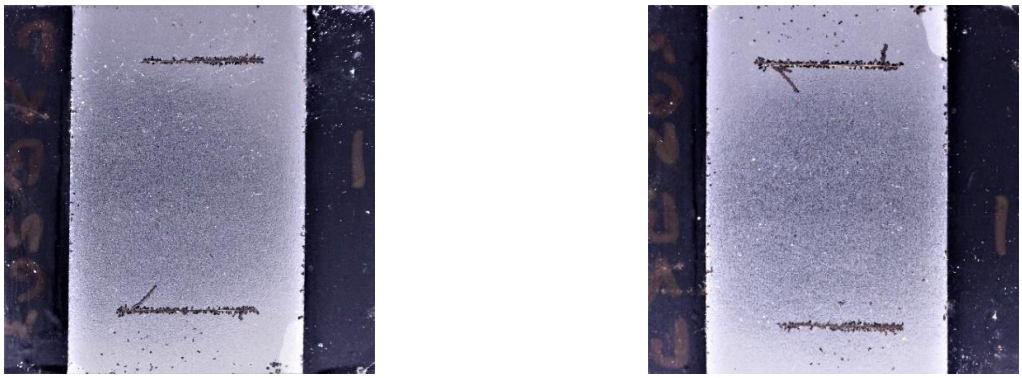

Week 3 Week 4

Figure 3.11 PVB photographs in 1-week intervals up to 4 weeks after initiation with 2µL of 0.005 $mol.dm^{-3}$ $FeCl_2$ per scribe

AL P

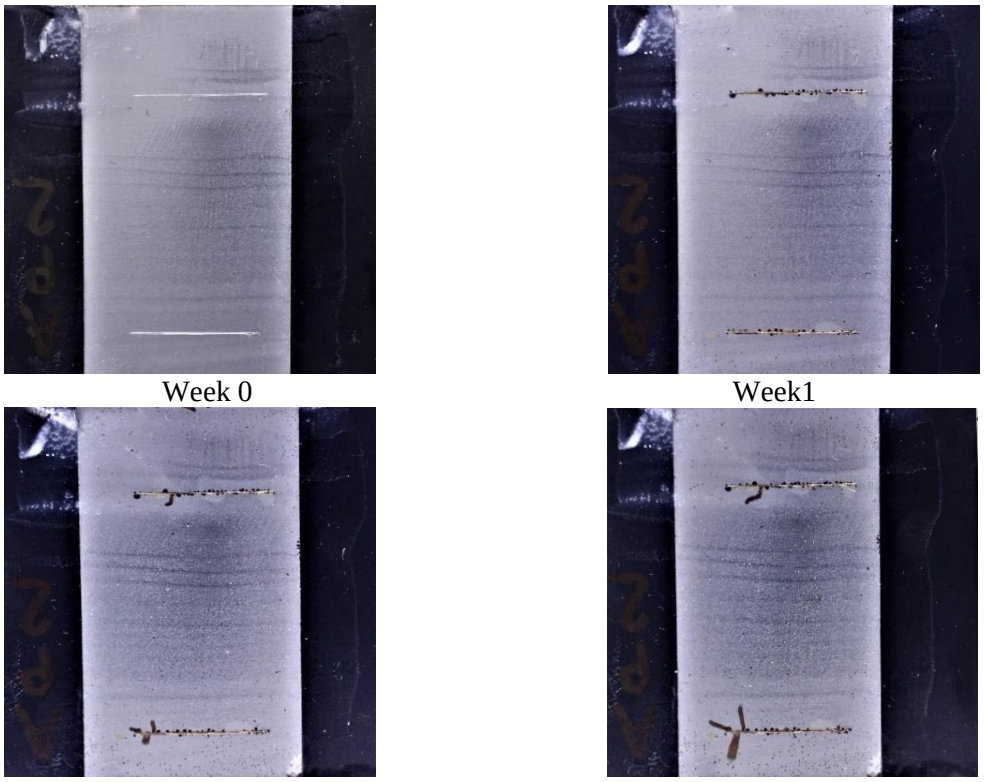

Week 0 Week1

Week 2 Week 3

Figure 3.12 AL P in 1-week intervals up to 3 weeks after initiation with 2µL of 0.005 $mol.dm^{-3}$ $FeCl_2$ per scribe

GF

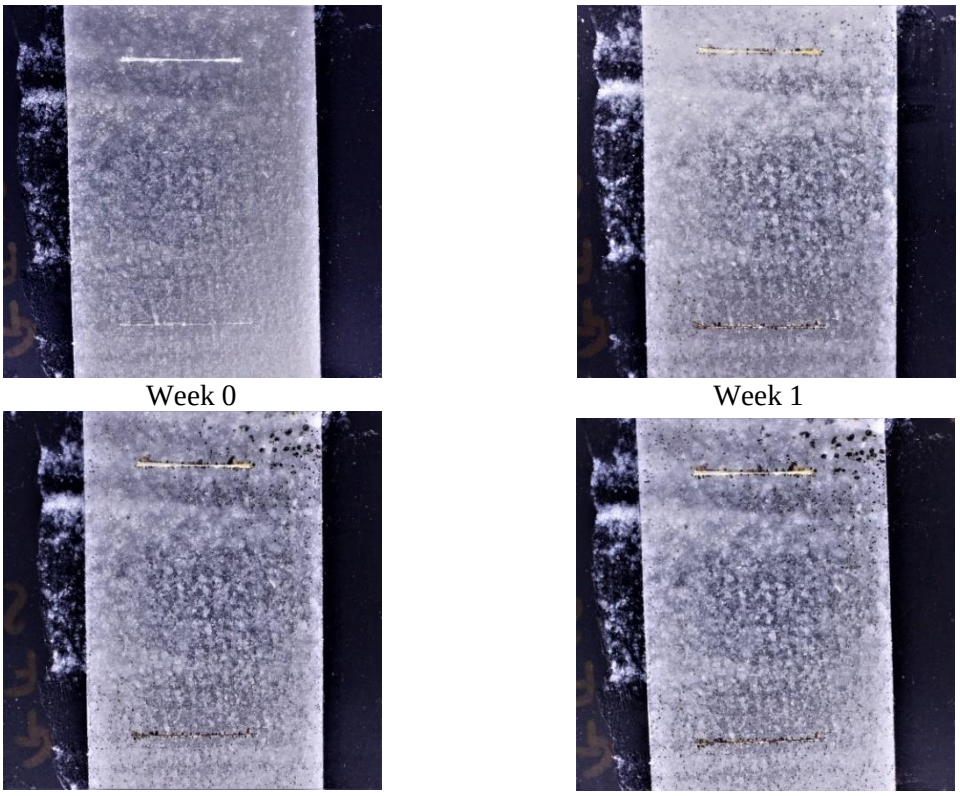

Week 0 Week 1

Week 2 Week 3

Figure 3.13 GF in 1-week intervals up to 3 weeks after initiation with 2µL of 0.005 $mol.dm^{-3}$ $FeCl_2$ per scribe

3.4.2 RAPTOR-7 vs PVB

Table 3.4 summarises the mean filament data recorded for each coating between the four scribes. Where the no. filaments is the average of the calculated number of filaments formed per scribe; the length (mm) and width (mm) are the mean values obtained for all the filaments for each coating; filament area (mm^2) is the average filament area; the total corroded area (mm^2) is the average total corroded area per scribe and dL/dt is the average linear growth rate for a filament. Where the highlighted rows showing the filament data for the corresponding coatings after 3 weeks. This was done to allow for a direct comparison between the filaments that formed for ALP,GF and RAPTOR as ALP and GF coatings were only ran for 3 weeks opposed to RAPTOR and PVB which were both ran for a total time of 4 weeks.

The mean filament length and mean total FFC corroded area for RAPTOR-7 and PVB are shown as a function of time in figures 3.14, and 3.15 respectively. Figure 3.14 shows that the linear velocity growth rate for filaments on PVB coated iron is slower than RAPTOR-7 coated iron. This correlates with the calculated growth velocity seen in table 3.4. Figure 3.15 shows that corroded area growth for a scribe is greater for RAPTOR than PVB by a significant amount despite the number of filaments being equal. The difference is due to the filaments under RAPTOR-7 being wider and longer than the filaments formed on PVB. The linear velocity for PVB recorded are lower than previously recorded for PVB on iron (0.3µm/min) by a third [114]

The growth rate recorded for RAPTOR-7 within this study is within the range recorded by another study evaluating the characteristics of a polyurethane coating on steel which recorded the rate as (0.16-0.5 mm/day) [105].

The variation in growth rate for RAPTOR-7 and PVB opposed to the preciously recorded values could arise from variation in the coating formulations or experimental conditions such as temperature, amount and type of initiating electrolyte, substrate and relative humidity .To conclude, whilst values for the linear growth of PVB varied from previously recorded data the results still show that RAPTOR-7 is susceptible to filiform corrosion. In addition, the filaments that form are larger in length, width and area.

Table 3.4 *Summary of average filament data for RAPTOR-7, PVB, GF, and AL P. With the highlighted rows showing data for 3 weeks and the unhighlighted for 4 weeks.*

Coating	NO. Filaments	Length (mm)	Width (mm)	filament area (mm2)	Total corroded area (mm2)	dL/dt (μm/hr)
PVB	5	2.95	0.32	0.6	2.84	5.78 ± 0.86
RAPTOR-7	5	8.78	1.37	9.55	44.49	13.36±3.52
RAPTOR-7	5	5.48	1.02	6.48	30.25	10.97 ± 2.89
AL P	2	3.08	0.69	1.85	4.33	10.43 ± 1.8
GF	3	0.91	0.60	0.31	0.47	2.72 ± 0.83

Figures 3.10 and 3.11 show the presence of filaments on both PVB and RAPTOR-7 1 week after initiation. RAPTOR-7 and PVB both show an average of 5 filaments per scribe. The final mean length of the filaments formed on RAPTOR-7 is (8.78 $\pm$ 2.75) mm based on 13 measurements whereas filaments on PVB coated iron had a mean length of (2.95 $\pm$ 0.88) mm. In the case of PVB, the average width based on 15 measurements is (0.32$\pm$ 0.09) mm. In comparison, for RAPTOR-7 the average width is (1.37$\pm$0.20) mm. The filament width for RAPTOR-7 increased over time from a mean width of 0.67 mm at week 1 to 1.37 mm at week 4. The filament widths for PVB remained constant over time within the error mentioned above. As the same volume of electrolyte that is added to each scribe is constant it can be assumed that the total amount of soluble chloride salts which constitutes the FFC filament-head electrolyte is constant between the scribes. Additionally, as the mean number of filaments that formed per scribe by week 4 for PVB and RAPTOR-7 are equal it can be assumed that the difference in the cross-sectional profiles and growth of the filaments can be attributed to the difference between the coatings.

Filament width can be related to the physical properties of the coating, following Equation 3.5, which was originally derived for a blister geometry, where G_a. is the energy required to delaminate the coating per unit of interfacial area, p is the critical pressure to grow a blister, r is the blister radius, t is the coating thickness, and E is the young's modulus of the coating [145,146].

$$G_a = \left(\frac{p^4 r^4}{17.4Et}\right)^{1/3} \quad \text{(Eqn 3.5)}$$

To apply the equation a series of assumption must be made. Firstly, the blister diameter is assumed to be larger than the coating thickness; secondly that no viscoelastic energy is dissipated in the blister growth; finally, the radius of the filaments is assumed to be half the filament width. The FFC filaments formed can be considered as a series of blisters and the use of Eqn 3.5 is therefore considered to be appropriate [20,147]. Firstly the coating thickness of RAPTOR-7 was thicker than the PVB coating. Additionally, as the apparent adhesion of PVB is lower than for RAPTOR it can be assumed that the G_a value for RAPTOR is higher than for PVB .Therefore, the equation predicts that the blister radius formed under the polyurethane coating should be wider than those observed on PVB. This finding is supported by the mean filament widths recorded in table 3.4. Similar observations were made in another study looking at the width of FFC filaments observed on epoxy coated and PVB coated steel [144].

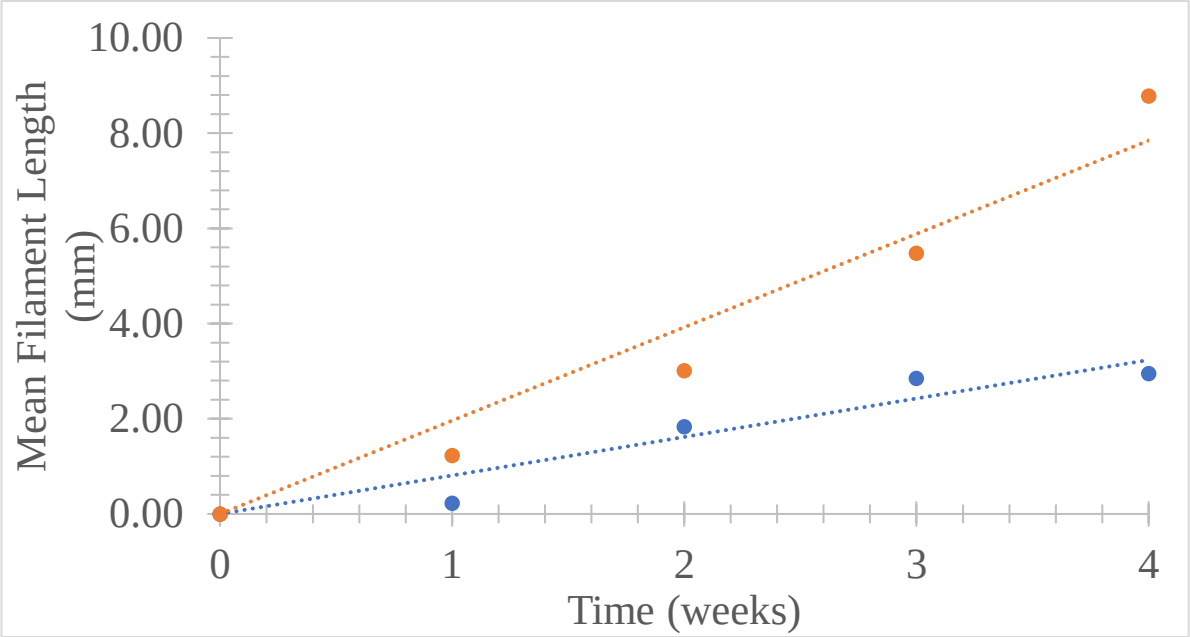

Figure 3.14 Plot of Mean filament length (mm) vs. Time (weeks) for RAPTOR-7 (orange) and PVB (blue).

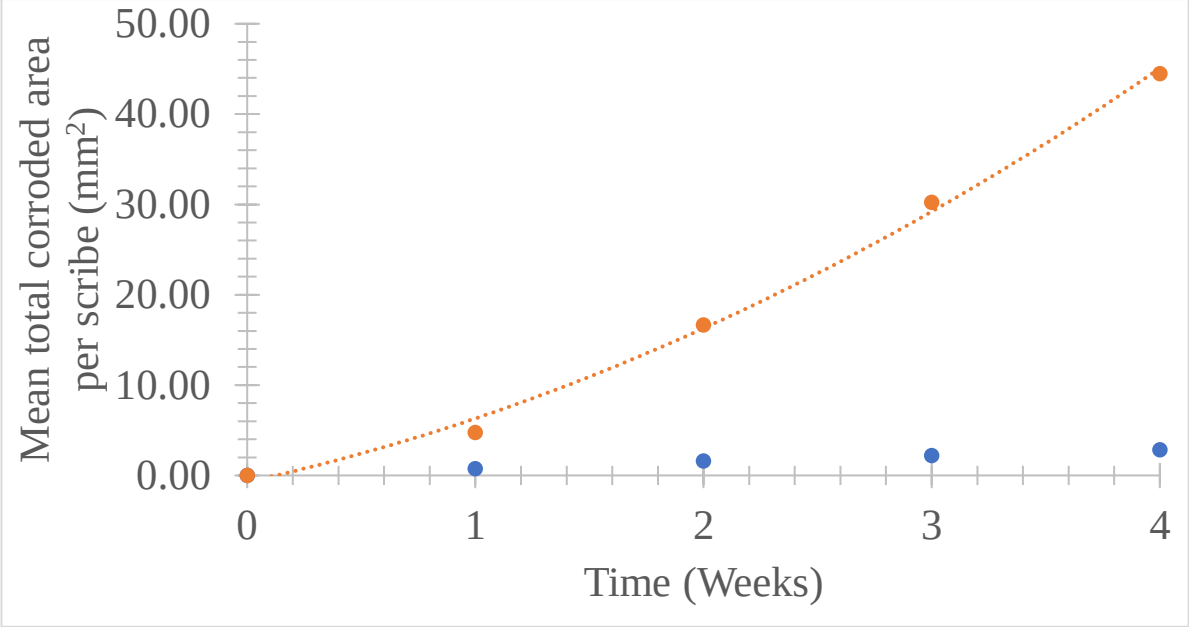

Figure 3.15 Plot of Mean total corroded area per scribe (mm^2) vs. time (weeks) for RAPTOR-7 (orange) and PVB (blue)

3.4.3 RAPTOR-7 vs Pigmented variants

Firstly, more filaments per scribe were observed on RAPTOR-7 coated iron than GF and ALP for the same experimental time as seen in table 3.4. The mean length of filaments observed on RAPTOR-7 after 3 weeks was (5.48± 1.71) mm whilst those seen on ALP had mean length of (3.08± 1.18) mm Filament on GF coated iron had a length of (0.91 ± 0.28) mm. The filaments observed for RAPTOR-7 were larger than the filaments for ALP and GF. The filaments for ALP and GF remained at a constant width within one standard deviation of the mean width .The total area per scribe is higher for RAPTOR-7 after 3 weeks than ALP and GF by 25.92 ± 2.46 mm^2 for ALP and 29.78 ± 3.17 mm^2 for GF. This is expected as more filaments that are wider and longer form on RAPTOR-7.

The FFC propagation rates were compared by plotting the mean filament length and average total corroded area per scribe against (t_f-t_i) for each of the coatings in Figures 3.16 and 3.17 respectively, where t_f is the time of the associated measurement and t_i is the time taken for the filaments to be initiated.. Filaments were observed on RAPTOR-7 one week after initiation and after the second week on the ALP and GF coated cells. Figure 3.16 shows that the linear growth rate of the filaments on ALP and RAPTOR-7 are similar,1.57± 0.18 mm/week and 1.45± 0.29 mm/week respectively.

A much lower linear growth rate of 0.51 mm/week was observed on GF iron. Figure 3.17 shows that while the linear rate is similar between RAPTOR-7 and ALP the growth rate of the total corroded area per scribe is much higher due to the increased number of filaments, and width of filaments. The rate of growth for RAPTOR-7 is taken as 7.62 mm^2/week compared to 2.09mm^2/week for ALP.

3.4.4 Inhibition mechanisms for Aluminium polyphosphate and Glass Flake on FFC

Firstly, as seen in section 3.4.3 the presence of ALP reduces the number of filaments that formed, as well as increased the initiation time . As previously stated, the volume and concentration of the initiation solution; and size of the defects for each sample were constant. Therefore, it can be assumed that any changes to the number of filaments that formed as well as the time required for the filaments to form between the different coating formulations are due to inhibition of the initiation process, whilst changes to the linear growth and area rates are due to inhibition of the propagation of the filaments. For ALP the linear growth rate in figure 3.16 was similar for both RAPTOR-7 and it can be assumed that the aluminium polyphosphate had a minimal effect on the propagation kinetics of the filaments. However, as less filaments were observed on ALP coated iron, as well as an increased initiation time.

It can therefore be assumed that aluminium polyphosphate inhibited the initiation process. When the electrolyte was added to the coating defect phosphate anions could form partially soluble or insoluble phosphates. The phosphate precipitates are deposited on the metal surface and could form cathodic blocking layers as well reduce the rate of diffusion for electroactive species [64,65,82,96]. This, will increase the time required to form the oxygen concentration cells required for the filaments to propagate [114]. GF showed the same level of inhibition to the initiation of filaments as ALP. However, it also reduced the rate at which the filaments grew. From figure 3.13 the filaments that did form on GF did not resemble the filaments seen for RAPTOR-7 or ALP. Additionally, due to the increased solid content and assumed irregularity of the surface of GF it could be assumed that the addition of glass flake increased the coatings susceptibility to rupture or break rather than providing inhibitive properties. If the coating broke the defect would increase in size. This increase in size would reduce the influence of capillary forces that are required to form the small aggregate of electrolyte that is required for the initiation of FFC [109].

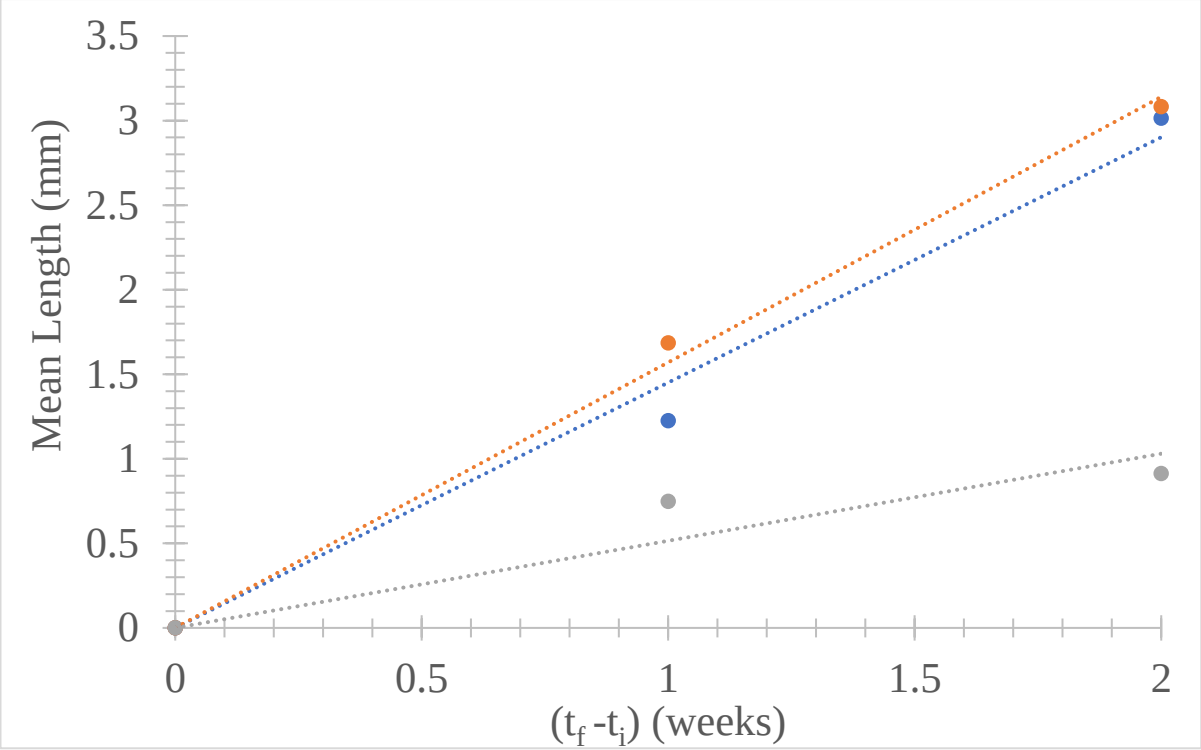

Figure 3.16 Plot of Mean filament Length (mm) vs. (t_f-t_i) (weeks) for RAPTOR-7 (Blue), AL P (Orange) and GF (Grey). Where t_i is 1week for RAPTOR-7, 2 Weeks for AL P and GF.

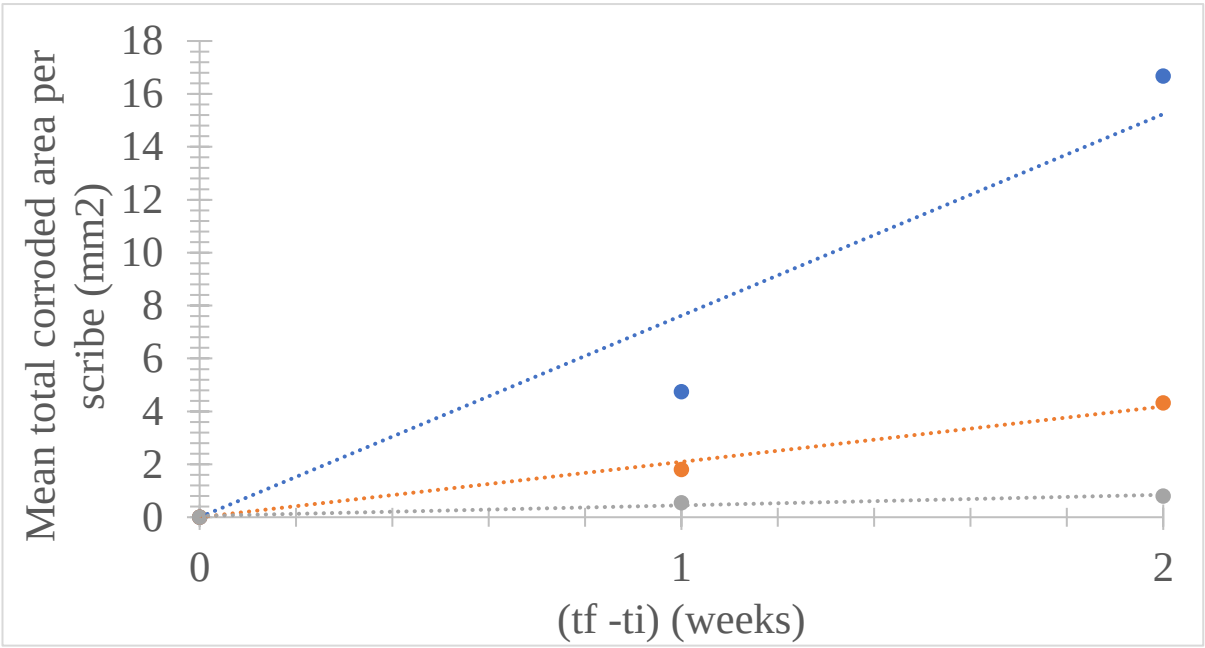

Figure 3.17 Plot of Mean total corroded area per scribe (mm^2) vs. (t_f-t_i) (weeks) for RAPTOR-7 (Blue), ALP (Orange) and GF (Grey).

Chapter 4 Conclusions and Future work

4.1 Conclusions

The main aim of the thesis was to develop an understanding of the key mechanisms responsible for corrosion driven organic failure of RAPTOR, a polyurethane coating directly applied onto iron. A combination of FTIR analysis, along with a adapted novel Stratmann cell methodology were utilised to quantify the degree of cure of RAPTOR (in terms of formation of urethane carbamate linkages) and its resistance to cathodic disbondment. The scanning Kelvin probe (SKP) was then used to obtain free corrosion potential (E_{corr}) profiles as a function of distance for the unpigmented and pigmented RAPTOR systems from the PVB/RAPTOR interface across the coating in 60 minute scan intervals. Delamination rate kinetics were obtained from the profiles revealing that RAPTOR and the 5%wt aluminium polyphosphate pigmented RAPTOR coating (ALP) exhibited parabolic rate kinetics, this being indicative of delamination being controlled by the mass migration of cations (Na^+ ions) under the coating to the delamination front. Filiform corrosion another corrosion driven organic failure mechanism was studied by introducing penetrative defects (scribes) into the coated iron coupons and adding 2µL of $FeCl_2$ per scribe. The coupons were then placed in a closed container maintained at a humidity of 94%. Time lapse photography and image analysis were then used to determine kinetics of filament initiation and propagation kinetics by measuring the filaments that formed from the scribes.

The key findings are as follows:

- An adapted novel delamination cell methodology has been successfully developed and applied to study cathodic disbondment of RAPTOR coated iron with the use of the SKP
- FTIR analysis along with delamination cells have shown that the resistance of RAPTOR to corrosion driven coating disbondment is directly related to cure time.
- The rate of cathodic delamination for unpigmented RAPTOR and ALP from iron has been shown to be controlled by mass transport of cations (Na^+)
- A 5 % wt addition of aluminium polyphosphate resulted in a 36% reduction in the rate constant of delamination k_d for RAPTOR compared to unpigmented RAPTOR
- Iron coated with unpigmented and pigmented RAPTOR has been shown to be susceptible to FFC when initiated with 2 µL of $5x10^{-3}$ $mol.dm^{-3}$ $FeCl_2$ per scribe.
- The kinetics of filiform initiation and propagation were evaluated and compared to previous studies involving PVB and Polyurethane coated iron/steel substrates [104,113]
- ALP increased the filiform initiation time by one week compared to uninhibited samples. No observed effect on the propagation rate of the filaments that formed.
- Glass flake pigmented RAPTOR (GF) did not influence the rate of coating delamination
- GF reduced the filiform propagation rate as well as increasing the initiation time of filaments during FFC.

4.2 Suggestions for future work

Further work that could be used to validate and extend the current research could include:

- Investigation into the effects of volume and concentration of initiating electrolyte on filiform initiation and propagation kinetics.
- Investigation into the mechanisms by which aluminium polyphosphate inhibits cathodic disbondment. For example, evaluating the solubility of the precipitates that form in alkaline environments
- Investigation into the affect varying the volume fraction of inhibitors within the coating have on inhibition to determine the critical loading point
- Investigate the influence of glass flake aspect ratio and volume on filament initiation and propagation rate occurring on RAPTOR coated iron.

5.0 References

[1] World steel in figures 2018, World Steel Association, last accessed November 03 2020: https://www.worldsteel.org/en/dam/jcr:f9359dff-9546-4d6b-bed0-996201185b12/World+Steel+in+Figures+2018.pdf

[2] Ahmad, Zaki. *Principles of Corrosion Engineering and Corrosion Control*, Elsevier Science & Technology, 2006.

[3] C. C. Technologies Laboratories, Inc. *Cost of corrosion and prevention strategies in the United States*, Ohio: Dublin, USA. 2001

[4] Federal Highway Administration (FHWA), Office of the Infrastructure and Development Report FHWA-RD-01-156. 2001

[5] National Association of Corrosion Engineers (NACE) Materials Performance , Special Issue, Houston, Texas, USA, July. Jointly with C. C. Technologies and FHWA. 2002

[6] Uhlig, H.H. *Corrosion and Corrosion Contro*l, 3rd ed. New York: John Wiley and Sons. 1985

[7] R.M Burns, W.W Bradley '*Protective coatings for meta*ls' second edition Reinhold publishing corporation 1955

[8] R.M.E Diamant G.R Ramage ed. *The prevention of corrosion* 1971 London, Business Books

[9] https://www.corrosionpedia.com/definition/2632/direct-to-metal-coatings, last accessed 25/10/2020

[10] https://www.paint.org/coatingstech-magazine/articles/taking-direct-to-metal-coatings-to-the-next-level,last accessed 19/12/2020

[11] Hui Chen, Jinhai Wang, Qun Huo, *Self-assembled monolayer of 3-aminopropyltrimethoxysilane for improved adhesion between aluminium alloy substrate and polyurethane coating*, Thin Solid Films, Volume 515, Issue 18, 2007

[12] Mattsson, Einar, *Basic Corrosion Technology for Scientists and Engineers*, 2nd ed. London: Institute of Materials, 1996

[13] Rosenqvist T. *Principles of extractive metallurgy*. 2nd ed. New York: McGraw-Hill Book Company; 1983

[14] J. C. Scully, *The Fundamentals of Corrosion*, 3rd edition, Oxford: Pergamon Press, 1990

[15] A. de S. Brasunas, NACE Basic Corrosion Course, Texas: National Association of Corrosion Engineers, 1970

[16] Cicek,Volkan. *Corrosion Engineering*, John Wiley & Sons, Incorporated, 2014.

[17] P.D. Donovan, *Mechanism of atmospheric corrosion, Protection of Metals from Corrosion in Storage and Transit*, Ellis Harwood Ltd, Chichester, 1986

[18] A. C. Fisher, *Electrode Dynamics*, Oxford Chemistry Primers, Oxford University Press, 2009

[19] I. Suzuki, *Corrosion Resistant Coating Technology*, New York: Marcel Dekker inc, 1989.

[20] M. Pourbaix, N. de Zoubov, in: M. Pourbaix (Ed.), *Atlas of Electrochemical Equilibria in Aqueous Solution*, Pergamon Press, 1966

[21] Gordon Ping Gu, James J. Beaudoin, Vangi S. Ramachandran,12 - *Techniques for Corrosion Investigation in Reinforced Concrete*, Handbook of Analytical Techniques in Concrete Science and Technology, William Andrew Publishing, 2001

[22] O'M Bockris, and A. K. N Reddy, *Modern Electrochemistry*, Vol. 2, Chapter 8, New York Plenum Press, 1970

[23] Tait, W. S., *An Introduction to Electrochemical Corrosion Testing for Practicing Engineers and Scientists*, PairODocs Publications 1994

[24] Wolfgang Schmickler , *Interfacial Electrochemistry* Oxford University Press, 1996

[25] Vladimir S. Bagotsky, and Klaus Mueller, *Fundamentals of Electrochemistry* John Wiley & Sons, Incorporated 2005

[26] M. Stratmann, M. Wolpers, H. Streckel, and R. Feser, Berichte Der Bunsen Gesellschaft-*Physical Chemistry Chemical Physics* 95:1365 ,1991

[27] K. Doblhofer and M. Cappadonia, Journal of Electroanalytical Chemistry 243:337(1988).

[28] Aguirre-Vargas ,11F *Thermoset coatings*. The Dow Chemical Company, Midland, MI, United States ,2018

[29] G.W. Walter, *A critical review of the protection of metals by paints,* Corrosion Science, Volume 26, Issue 1,Pages 27-38, 1986

[30] Henry Leidheiser, Jr , *De-adhesion at the Organic Coating/Metal Interface in Aqueous Media*. Center for Surface and Coatings Research, Lehigh University, USA 1979

[31] F.M. Fowkes, D.W. Dwight, J.A. Manson, T.B Lloyd, D.O. Tischler, B.A. Shah, *Enhanced mechanical properties of composites by modification of surface acidity or basicity of fillers*, in: D.M. Mattox, J.E.E. Baglin, C. Batich, R. Gottschall, (Eds.), Adhesion in Solids, vol. 119, MRS Symposium Proceedings,1988,

[32] D.M Mattox Handbook of Physical Vapor Deposition (PVD) *Processing Adhesion and Deadhesion* Cambridge University press 2014

[33] J.M. Burkstrand , *Metal-Polymer interfaces: Adhesion and X-ray photoemission studies* , J. Appl. Phys. 52 ,4795, 1981

[34] L.J. Gerenser , *Surface chemistry for treated polymers* , in D.A. Glocker , S. Ismat Shah (Eds.), Handbook of Thin Film Process Technology , Sec E.3.1, vol. 2 , Taylor & Francis , 2002

[35] Atul Tiwari, Lloyd Hihara, James Rawlins ,*Intelligent coatings for Corrosion Control* Butterworth-Heinemann 2014

[36] N. K. Akafuah, "*Automotive paint spray characterization and visualization*," in Automotive Painting Technology, K. Toda, A. Salazar, and K. Saito, Eds., Springer, Dordrecht, The Netherlands, 2013.

[37] G. Fettis, Ed., *Automotive Paints and Coatings*, Wiley-VCH, Weinheim, Germany, 1995.

[38] H. J. Streitberger and K. F. Dossel, *Automotive Paints and Coatings*, Wiley-VCH, Weinheim, Germany, 2008.

[39] J. V. Koleske, *Paint and Coating Testing Manual*: Fourteenth Edition of the Gardner-Sward Handbook, 1995.

[40] Kralj, M., Pavković, K., Stojanović, I., Anđal, J.: *Adhesion and anticorrosive properties of DTM coating as related to primer coating*, GRAĐEVINAR, 2019

[41] H. Leid heiser, Jr., G. W. Simmons, and E. Kellerman, J. Electrochem. Soc. 120 (1973)

[42] https://www.corrosionpedia.com/definition/2632/direct-to-metal-coatings,last accessed 25/10/2020

[43] Bayer, O, Siefhen, W., Rinke, H., Orther, L., & Schild, H. Germany Patent No. DRP 728981 (to I.G. Farberindustrie AG,1937

[44] Buchan, S, *Rubber to Metal Bonding*, C. Lockwood, London, 1948.

[45] Abbey K.J., Zalucha D.J. *The Chemistry of Structural Adhesives: Epoxy, Urethane, and Acrylic Adhesives*. In: Kent J., Bommaraju T., Barnicki S. (eds) Handbook of Industrial Chemistry and Biotechnology. Springer, Cham 2017

[46] Saunders, J. H., & Frisch, K. C. *Polyurethanes chemistry and technology*, High Polymers, Chemistry. Interscience Publishers, New York, Vol. XVI, Part I. 1962

[47] Rahman M.M., Rabbani M.M., Saha J.K., *Polyurethane and Its Derivatives*. In: Jafar Mazumder M., Sheardown H., Al-Ahmed A. (eds) Functional Polymers. Polymers and Polymeric Composites: A Reference Series. Springer, Cham ,2019

[48] Sabrina Tardio, Marie-Laure Abel, Robert H. Carr, John F. Watts, *The interfacial interaction between isocyanate and stainless steel*, International Journal of Adhesion and Adhesives, Volume 88, 2019,

[49] R. Giles Dillingham & Christopher Moriarty ,The Journal of Adhesion:*The adhesion of isocyanate-based polymers to steel* a Brighton Technologies Group, Inc, 2010

[50] Voyutskii, S. S., *Autohesion and Adhesion of High Polymers*, Wiley Interscience, New York, 1963

[51] Sexsmith, F. H., Adhesives Age, 3136, 1970.

[52] M. M Chehimi, and J. F Watts, J. Adhesion Sci. Technol., 6(3), 377393 ,1992

[53] H Ulrich.; *Chemistry and Technology of Isocyanates*, Wiley, 1996.

[54] D. Harrop, *Chemical Inhibitors for Corrosion Control*, Proceedings of the Industrial Division of the RSC and the Institute of Corrosion Science and Technology University of Manchester, 1990

[55] R. Naderi, M.M. Attar, *Electrochemical study of protective behavior of organic coating pigmented with zinc aluminum polyphosphate as a modified zinc phosphate at different pigment volume concentrations*, Prog. Org. Coat. 66, 2009

[56] Rabbetts A. *Replacements for hexavalent chromium in anodizing and conversion coating*. Trans Inst Metal Finish, 76(1):B4–5, 1998.

[57] W Funke, J. Oil Col. Chem. Assoc., 62,.1979

[58] Plueddemann E P. *Silane Coupling Agents*. New York: Plenum Press, 1991.

[59] W Funke; H. Leidheiser Jr, J. Oil Col. Chem. Assoc. 70 1987

[60] A. Momber, M. Irmer, N. Glück, *Performance characteristics of protective coatings under low-temperature offshore conditions*. Part 1: experimental setup and corrosion protection performance, Cold. Reg. Sci. Technol. 127, 2016

[61] H. Alhumade, R.P. Nogueira, A. Yu, A. Elkamel, L. Simon, A. Abdala, *Role of surface functionalization on corrosion resistance and thermal stability of epoxy/glass flake composite coating on cold rolled steel*, Progress in Organic Coatings, Volume 122, Pages 180-188, 2018,

[62] D. Laverde, J.C. Zubillaga, J. Gil-Sevillano, E. Villanueva, *The influence of the primer layer on mechanical damage and loss of corrosion protection of deformed painted Zn-0.16% Al and Zn-5% Al galvanized sheet steel* Corr. Sci. 37, 79, 1995

[63] J. Barraclough, J.B. Harrison, J. Oil Col. Chem. Assoc. 48 (4), 341, 1965

[64] M. Hernández, J. Genescá, J. Uruchurtu, F. Galliano, D. Landolt, *Effect of an inhibitive pigment zinc-aluminum-phosphate (ZAP) on the corrosion mechanisms of steel in waterborne coatings*, Progress in Organic Coatings, Volume 56, Issues 2–3, 2006,

[65] Yanwen Liu, Xiaorong Zhou, Stuart B. Lyon, Reza Emad, Teruo Hashimoto, Ali Gholinia, George E. Thompson, Derek Graham, Simon R. Gibbon, David Francis, *An organic coating pigmented with strontium aluminium polyphosphate for corrosion protection of zinc alloy coated steel*, Progress in Organic Coatings, Volume 102, Part A, 2017,

[66] R. Naderi, M.M. Attar, *Application of the electrochemical noise method to evaluate the effectiveness of modification of zinc phosphate anticorrosion pigment*, Corros. Sci. 51, 1671–1674, 2009

[67] A.M. Simões, J. Torres, R. Picciochi, J.C.S. Fernandes, *Corrosion inhibition at galvanized steel cut edges by phosphate pigments*, Electrochim. Acta 54, 3857–3865, 2009

[68] Y. Hao, F. Liu, E. Han, S. Anjum, G. Xu, *The mechanism of inhibition by zinc phosphate in an epoxy coating*, Corros. Sci. 69, 2013

[69] Y. Shao, C. Jia, G. Meng, T. Zhang, F. Wang, *The role of a zinc phosphate pigment in the corrosion of scratched epoxy-coated steel*, Corros. Sci. 51, 2009

[70] V.F. Vetere, M.C. Deya, R. Romagnoli, B. del Amo, *Calcium tripolyphosphate: an anticorrosive pigment for paint*, J. Coat. Technol. 73, 2001

[71] M.R. Heydarpour, A. Zarrabi, M.M. Attar, B. Ramezanzadeh, *Studying the corrosion protection properties of an epoxy coating containing different mixtures of strontium aluminum polyphosphate(SAPP) and zinc aluminum phosphate (ZPA) pigments*, Prog. Org. Coat. 77, 2014

[72] R. Naderi, M.M. Attar, *Electrochemical assessing corrosion inhibiting effects of zinc aluminum polyphosphate (ZAPP) as a modified zinc phosphate pigment*, Electrochim. Acta 53, 2008

[73] A. Kalendova, *Comparison of the anticorrosion efficiencies of pigments based on condensed phosphates and polyphosphosilicates*, Anti-Corros. Methods Mater. 50 , 2003

[74] E. Alibakhshi, E. Ghasemi, M. Mahdavian, *Corrosion inhibition by lithium zinc phosphate pigment*, Corros. Sci. 77, 2013

[75] R. Naderi, M.M. Attar, *The role of zinc aluminum phosphate anticorrosive pigment in Protective Performance and cathodic disbondment of epoxy coating*, Corros. Sci. 52, 2010

[76] Y.F. Yang, J.D. Scantlebury, E. Koroleva, O. Ogawa, H. Tanabe, *A novel anti-corrosion calcium magnesium polyphosphate pigment and its performance in aqueous solutions on mild steel*, ECS Trans. 24, 2010

[77] R. Naderi, M. Mahdavian, A. Darvish, *Electrochemical examining behavior of epoxy coating incorporating zinc-free phosphate-based anticorrosion pigment*, Prog. Org. Coat. 76 , 2013

[78] C. Deyá, G. Blustein, B. del Amo, R. Romagnoli, *Evaluation of eco-friendly anticorrosive pigments for paints in service conditions*, Prog. Org. Coat. 69 ,2010

[79] R. Naderi, M.M. Attar, *The inhibitive performance of polyphosphate-based anticorrosion pigments using electrochemical techniques*, Dyes Pigm. 80, 2009

[80] Dong dong Song, Jin Gao, Lin Shen, Hongxia Wan, and Xiaogang Li, *The Influence of Aluminum Tripolyphosphate on the Protective Behavior of an Acrylic Water-Based Paint Applied to Rusty Steels*, Corrosion and Protection Center, University of Science and Technology Beijing, 2015

[81] P. de Lima-Neto, A. P. de Araujo, W. S. Ara ´ ujo, and A. N. ´ Correia, "*Study of the anticorrosive behaviour of epoxy binders containing non-toxic inorganic corrosion inhibitor pigments*" Progress in Organic Coatings, vol. 62, no. 3, 2008.

[82] M. A. Hernandez, F. Galliano, and D. Landolt, "*Mechanism of cathodic delamination control of zinc-aluminum phosphate pigment in waterborne coatings*," Corrosion Science, vol. 46, no. 9,2004

[83] A. Guenbour, A. Benbachir, A. Kacemi, Surf. Coat. Technol. 113, 36, 1999

[84] H.S. Isaacs, A.J. Aldykiewicz Jr., D. Thierry, T.C. Simpson, Corrosion 52, 163, 1996

[85] M. Bethencourt, F. J. Botana, M. Marcos, R. M. Osuna, and J. M. Sanchez-Amaya, "*Inhibitor properties of 'green' pigments for ´ paints*," Progress in Organic Coatings, vol. 46, no. 4, 2003.

[86] M. C. Deya, G. Blustein, R. Romagnoli, and B. del Amo, "*The influence of the anion type on the anticorrosive behaviour of inorganic phosphates*," Surface and Coatings Technology, vol. 150, no. 2-3, 2002.

[87] H. Kukackova, A. Vraˇstilova, and A. Kalendova, "*Non-toxic anticorrosive pigments intended for applications in high-solids and waterborne paints*," Physics Procedia, vol. 44, 2013

[88] V. Vetere, M. Deya, R. Romagnoli, B. del Amo, JCT 73 (917) , 2001

[89] I. Zin, S. Lyon, V. Pokhmurskii, Corros. Sci. 45, 777, 2003

[90] G. Hatch, O. Rice, Ind. Eng. Chem. 37, 710, 1945

[91] O. Lahodny-Sarc, L. Kastelan, Corros. Sci. 16, 25, 1976

[92] G.B. Hatch, Mater. Protect. 8, 31, 1969

[93] A. Forsgren, *Corrosion Control Through Organic Coatings*, CRC Press, 2006.

[94] A. Kalendova, D. Vesely, J. Brodinova, *Anti-Corros. Methods Mater*. 51, 6, 2004

[95] M. Ebrahimi-Mehr, T. Shahrabi, M.G. Hosseini, *Anti-Corros. Methods Mater*. 51, 399. 2004

[96] X. Lu, Y. Zuo, X. Zhao, and Y. Tang, "*The influence of aluminum tri-polyphosphate on the protective behavior of Mg-rich epoxy coating on AZ91D magnesium alloy*," Electrochimica Acta, vol. 93, 2013.

[97] M. Deyá V.F. Vetere R. Romagnoli B. del Amo, "*Aluminium tripolyphosphate pigments for anticorrosive paints*", Pigment & Resin Technology, Vol. 30 ,2001

[98] J. Kumanotani, J. Metal Finishing Soc: 579 1981

[99] H. N. McMurray and G. Williams ,*Under Film/Coating Corrosion* ,Materials Research Centre, School of Engineering, Swansea University, Elsevier B.V. 2010

[100] H. Leidheiser, W. Wang, and L. Igetoft, *Progress in Organic Coatings* 11:19 ,1983

[101] C.F. Sharman, Nature 153, 621, 1944

[102] N. LeBozec, D. Persson, D. Thierry, S.B. Axelsen, *Effect of climatic parameters on filiform corrosion of coated aluminum alloys*, Corrosion 60, 2004

[103] W. Schmidt, M. Stratmann, *Scanning kelvin probe investigations of filiform corrosion on aluminum alloy* 2024-t3, Corros. Sci. 40, 1998

[104] W.H. Slabaugh, M. Grotheer, *Mechanism of filiform corrosion*, Ind. Eng. Chem. 46, 1954

[105] R.T. Ruggeri, T.R. Beck, *An analysis of mass transfer in filiform corrosion*, Corrosion-NACE 39, 1983

[106] N. Wint, D. Eaves, E. Michailidou, A. Bennett, J.R. Searle, G. Williams, H.N. McMurray, *The kinetics and mechanism of filiform corrosion occurring on zinc-aluminium-magnesium coated steel*, Corrosion Science, Volume 158, 2019

[107] Rudolph G. Buchheit, *Corrosion Resistant Coatings and Paints*, Handbook of Environmental Degradation of Materials Elsevier Inc CHAPTER 21 , 2018

[108] Van Loo, M., Laiderman, D. D., and Bruhn, R. R., Corrosion, Vol. 9, , 1953

[109] W. Funke, Prog. Org. Coat. 9, 29, 1981

[110] W. Funke, Ind. Eng. Chem. Prod. Res. Dev. 24, 343, 1985

[111] H.J.W. Lenderink, *Electrochemical Characterisation of Filiform Corrosion on Aluminium Rolled Products* Ph.D. thesis, Techniche University Delft, The Netherlands, 1995

[112] Popov, Branko N.. Corrosion Engineering *: Principles and Solved Problems*, Elsevier, 2015.

[113] H. Leidheiser, corrosion NACE, 38(7) pg374, 1982

[114] Geraint Williams, H.Neil McMurray, *The mechanism of group (I) chloride initiated filiform corrosion on iron,* Electrochemistry Communications, Volume 5, Issue 10, 2003,

[115] A. Bautista, Prog. Org. Coatings,28, 1996.

[116] Bennett, Andrew Richard *Novel anti-corrosion coatings on steel* ,thesis, Swansea University, 2009

[117] Koehler, E. L. Corrosion 33, 209, 1977,

[118] A. Leng, H. Streckel, K. Hofmann, and M. Stratmann, Corros. Sci., vol. 41, no. 3, 1998.

[119] W. Fürbeth and M. Stratmann, Prog. Org. Coatings, vol. 39, 2000.

[120] G. Grundmeier, W. Schmidt, and M. Stratmann, Electrochim. Acta, vol. 45, 2000.

[121] H. Leidheiser and M. Kendig, Eng. Chem. Prod. Res. Dev., vol. 17, no. 1, 1978.

[122] M. Rohwerder and A. Michalik, Electrochim. Acta, vol. 53, no. 3, 2007

[123] Castle, J. E.; Watts, J. F. *Corrosion Control by Organic Coatings*; Leidheiser, H., Ed.; NACE: Houston, 1981

[124] Hammond, J. S.; Holubka, J. W.; Dickie, R. A. J. Coat. Technol. , 51, 45, 1979

[125] Evans, U. R. *The Corrosion and Oxidation of Metals*; St Martins Press: NY, 1960

[126] Delahay, P. *Double Layer and Electrode Kinetics;* Interscience, 1966;

[127] R.F. Hamade, D.A. Dillard, Int. J. Adhes. Adhes. 25, 2005

[128] G. Williams, S. Geary, and H. N. McMurray, Corros. Sci., vol. 57 , 2012

[129] G. Williams and H. N. McMurray, J. Electrochem. Soc., vol. 148, no. 10, B377, 2001.

[130] W. Fürbeth and M. Stratmann, Corros. Sci., vol. 43, no. 2, 2001.

[131] G. Williams, H. N. McMurray, and D. A. Worsley, J. Electrochem. Soc., vol. 149, 4, B154, 2002.

[132] M. Stratmann, R. Feser, and A. Leng, Electrochimica Acta 39:1207 1994.

[133] Coates, J. *Interpretation of Infrared Spectra, A Practical Approach*. In Encyclopedia of Analytical Chemistry ,2006

[134]https://www.thermofisher.com/uk/en/home/industrial/spectroscopy-elemental-isotope-analysis/spectroscopy-elemental-isotope-analysis-learning-center/molecular-spectroscopy-information/ftir-information/ftir-basics.html, last accessed [11/12/2020]

[135] https://www.moleculardevices.com/technology/absorbance#gref, last accessed 11/12/2020

[136] A. K. Neufield, American Laboratory 35:21 2003

[137] A. Leng, H. Streckel, and M. Stratmann, Corrosion Science 41:547 (1999).

[138] Michael Steiger, Sönke Asmusse, Geochimica et Cosmochimica Acta 72 *Crystallization of sodium sulfate phases in porous materials*: The phase diagram Na2SO4–H2O and the generation of stress Department of Chemistry, University of Hamburg, 2008

[139] M. Ginic-Markovic1 , N. R. Choudhury , J. G. Matisons and D. R. G. Williams *Characterisation of polyurethane coatings using thermo analytical techniques* Journal of Thermal Analysis and Calorimetry, Vol. 59, 2000

[140] G. Klimow, N. Fink, G. Grundmeier, *Electrochemical studies of the inhibition of the cathodic delamination of organically coated galvanised steel by thin conversion films*, Electrochim. Acta. 53 ,2007

[141] C.F. Glover, C.A.J. Richards, G. Williams, H.N. McMurray, *Evaluation of multi-layered graphene nano-platelet composite coatings for corrosion control part II – Cathodic delamination kinetics*, Corros. Sci. 136 (2018)

[142]A. Leng, H. Streckel, M. Stratmann, *The delamination of polymeric coatings from steel. Part 2: First stage of delamination, effect of type and concentration of cations on delamination, chemical analysis of the interface*, Corros. Sci. 41 ,1999

[143] M. Stratmann, A. Leng, W. Fürbeth, H. Streckel, H. Gehmecker, K.H. GroßeBrinkhaus, *The scanning Kelvin probe; a new technique for the in situ analysis of the delamination of organic coatings*, Prog. Org. Coatings. 27 ,1996

[144] S.M. Cambier and G.S. Frankel ,*Filiform Corrosion of Polyvinyl Butyraland Bisphenol A-Based Epoxy-Coated Steel After Standard Laboratory Exposures* ,2014

[145] A.N. Gent, L.H. Lewandowski, J. Appl. Polym. Sci. 33 ,1987

[146] M. Kappes, G.S. Frankel, N. Sridhar, Prog. Org. Coat. 69 ,2010

[147] R.C. Rincon Troconis, G.S. Frankel, Corrosion 70 ,2014